Laser-induced nuclear dynamics in hydrocarbons

Christian Burger

München 2018

Laser-induced nuclear dynamics in hydrocarbons

Christian Burger

Dissertation
an der Fakultät für Physik
der Ludwig–Maximilians–Universität
München

vorgelegt von
Christian Burger
aus Berlin

München, den 11. April 2018

Erstgutachter: Prof. Dr. Matthias F. Kling
Zweitgutachter: Prof. Dr. Regina de Vivie-Riedle
Tag der mündlichen Prüfung: 24. Mai 2018

Zusammenfassung

In unserem täglichen Leben spielen Kohlenwasserstoffe eine wesentliche Rolle, sei es aufgrund von Zuckern, Fetten oder Proteinen in der Nahrungsaufnahme oder bei der Reinigung von Brillengläsern mit Isopropanol. Während die meisten Kohlenwasserstoffe in der Natur vorkommen, werden einige auch durch spezielle Prozesse erzeugt, welche die molekulare Bindungsstruktur ändern. Dies beeinflusst ebenfalls die chemischen, physikalischen und biologischen Eigenschaften der Moleküle. Abgesehen von standardmäßig verwendeten chemischen Verfahren können molekulare Bindungen auch mittels ultrakurzer Laserpulse mit definierten elektrischen Feldern – so genannten Träger-Einhüllende-Phasen (CEP) stabilen Laserpulsen umstrukturiert werden.

Die vorliegende Arbeit befasst sich mit den grundlegenden Prozessen, welche zur Interaktion von ultrakurzen Laserpulsen mit kleinen Kohlenwasserstoffen, wie Acetylen und Propadien, beitragen. Insbesondere die Änderung der Bindungsstruktur durch Protonenmigration, die sogenannte Isomerisierung, ist mithilfe der CEP oder der Laserintensität kontrollierbar.

Durch die gleichzeitige Untersuchung der Intensitäts- und CEP-Abhängigkeit der Isomerisierung wird deutlich, wie wichtig der Ionisationsmechanismus für alle nachfolgenden Prozesse ist. Für geringe Intensitäten (unter $1.5 \cdot 10^{14}\,\mathrm{W/cm^2}$) induziert die nichtsequentielle Doppelionisation eine starke CEP-Abhängigkeit. Für höhere Intensitäten wird die sequentielle Doppelionisation wahrscheinlicher, was in einer geringeren CEP-Kontrolle resultiert.

Um die zeitliche Entwicklung der Isomerisierung zu untersuchen, wurden Pump-Probe-Experimente an Acetylen durchgeführt. Die typische Pulsdauer ist mit weniger als 5 fs schneller als jede Kernbewegung und daher für die Messung verschiedenster molekularer Reaktionen auf ultrakurzer Zeitskala gut geeignet. Zum einen kann die Isomerisierung in “Echtzeit” dargestellt werden, wodurch die durchschnittliche Isomerisierungszeit zu 54 fs bestimmt werden konnte. Zum anderen wurde eine Vibration mit einer Periode von 26 fs detektiert, welche auf eine Bewegung der CC-Bindung im Kation zurückschließen lässt. In einer weiteren Untersuchung wurden Vibrationenperioden von 11 fs und 20 fs gemessen, die respektiv auf Vibrationen der CH- und CC-Bindungen in Dikation hinweisen.

Betrachtet man zusätzlich die dissoziierenden Moleküle, so ist der Effekt der ”Erhöhten Ionisation” (EI) von Interesse. Diese EI ist durch eine signifikante Erhöhung der Ionisationswahrscheinlichkeit gekennzeichnet, welche nur bei bestimmten internuklearen Abständen

auftritt, in der CC-Bindung bei 1.4 Å und in der CH-Bindung bei 2.0 Å. Experimentell konnte dieser Effekt der erhöhten Ionsierungsrate im Dikation zwischen 10 fs und 40 fs gemessen werden.

Im letzten Teil der Arbeit wird der Aufbau eines Mehrfarben-Experiments mit einem zusätzlichen Feld-Synthetisierer vorgestellt. Erste erfolgreiche Experimente zeigen die interessanten Anwendungsgebiete dieses komplexen Systems auf.

Die Ergebnisse der vorliegenden Arbeit zur laserinduzierten Kontrolle molekularer Bindungen ermöglichen ein besseres Verständnis der grundlegenden molekularen Reaktionen, welche essentiell für zukünftige Experimente und Anwendungen, wie zum Beispiel für die die Kontrolle der Molekularbewegung an konischen Durchschneidungen, sind.

Abstract

Hydrocarbon molecules play an important role in various situations in our daily life ranging from sugar, fat, and protein in food consumption to isopropanol for cleaning of glasses. While most of these hydrocarbons exist naturally, others have to be produced by special processes involving bond rearrangements, which result in an altered molecular structure and thus in changed chemical, physical, and biological properties. Apart from standard chemical procedures another promising possibility to control such molecular rearrangements is based on ultrashort laser pulses with defined electric fields, so called carrier-envelope phase (CEP) stable laser pulses.

In this thesis, the fundamental processes involved in the interaction of ultrashort laser pulses with small hydrocarbons, i.e. acetylene and propadiene, are investigated. Especially the bond rearrangement via proton migration, also called isomerization, is controlled via the CEP or the applied laser intensity. In the first part of this thesis, the CEP control over isomerization is explained by a superposition of vibrational wave-packets, which are triggered by the laser pulse. The initial directionality of the wave-packet predetermines the final molecular structure, which manifests long after the laser pulse has passed. Investigating both the intensity- and the CEP-dependence of the isomerization reveals the influence of the ionization onto subsequent nuclear motion. For low intensities (below $1.5 \cdot 10^{14}\,\mathrm{W/cm^2}$), the non-sequential double-ionization allows for a strong CEP-control of the isomerization. By increasing the intensity, sequential double-ionization becomes the dominating process, such that the CEP-control is suppressed.

In order to investigate the temporal evolution of the isomerization, a few-cycle pump-probe experiment is performed on acetylene. The typical pulse duration of below 5 fs is faster than any nuclear motion and hence permits the detection of different molecular reactions triggered by the ultrashort laser pulse. First, the isomerization process is visualized in "real" time, enabling us to determine the mean isomerization time to 54 fs. Secondly, a vibrational motion of 26 fs is detected, indicating CC-bond vibrations in the cation state. Thirdly, the duration of a vibrational motion is determined for CH- and CC-bond vibrations in the dication state to be 11 fs and 20 fs, respectively. Furthermore, in dissociating molecules, the effect of enhanced ionization (EI) is investigated in acetylene. EI is characterized by a significant enhancement of the ionization probability for molecules with a distinct internuclear distance, i.e. 1.4 Å for the CC-bond and 2.0 Å for the CH-bonds. Experimentally, this effect was observed as an increased ionization yield between 10-40 fs.

For the last part of this thesis, a three-color generation setup with subsequent field synthesizer is developed and first successful experiments are performed, which demonstrates its flexible applicability.

The knowledge of laser-induced nuclear dynamics and its control gained in this thesis opens the path for exciting future experiments and applications such as the control over molecular reactions at conical intersections.

Contents

Abbreviation

ADC	analog-to-digital converter
ADK	Ammosov, Delone, and Krainov
AOFS	acousto-optic frequency shifter
Ar	argon
ATI	above-threshold ionization
BBO	β-barium-borate
CE	Coulomb explosion
CEI	Coulomb explosion imaging
CEP	carrier-envelope phase
CFD	constant fraction discriminator
DLD	delay-line detector
EI	enhanced ionization
FROG	frequency-resolved optical-gating
HHG	high harmonic generation
KER	kinetic energy release
MCP	micro-channel plate
MPI	multi-photon ionization
Ne	neon
NSDI	non-sequential double ionization
PES	potential energy surface
PIPICO	photoion-photoion coincidence
REMI	reaction microscope
SDI	sequential double ionization
SFG	sum-frequency generation
SHG	second harmonic generation
SMM	Simple Man's Model
TDC	time-to-digital converter
TI	tunnel ionization
TOF	time-of-flight

UHV ultra-high vacuum
VMI velocity-map imaging

1 Introduction

A famous example of molecular dynamics is the interaction of highly energetic photons with ozone molecules in the earth's atmosphere. Ozone (O_3) absorbs a photon and thereby obtains enough energy to dissociate into dioxide (O_2) and oxygen (O). Such photo-dynamic processes occur on very short timescales, i.e. within pico- or femtoseconds (10^{-12} to 10^{-15} s). In order to investigate such processes, it is necessary to trigger and observe the reaction on the same timescale, which is so far only feasible using optical methods with ultrashort laser pulses. In this thesis, such pulses are employed to investigate molecular dynamics.

In the past decades, extensive work was performed to improve the understanding of light-matter interaction using ultrashort laser pulses [1]. One advantage of such laser pulses is the high photon density, which increases the interaction probability between the investigated molecule and the light. To describe the interactions, it is often advantageous to use the wave nature of light, i.e. to express the laser pulses by an electric field. The molecular reaction can be altered considerably by changing the parameters of these strong fields as for example pulse duration [2], wavelength [3], intensity [4], or carrier-envelope phase (CEP) [5], which is a measure of the electric field shape. Within all these interactions, the laser pulse controls the electronic and to a lesser extend the nuclear motion and thereby influences the remaining target such that the molecular arrangement evolves in a predetermined manner. This can be seen for example in hydrocarbons, like acetylene or allene, where a laser pulse of ∼5 fs initiates a nuclear wave-packet in an excited state and thereby predetermines the deprotonation or isomerization, occurring about 50 fs later [6, 7].

Such hydrocarbons are essential for our daily life as they usually build the basis of proteins, sugars, fats, and many other components. A variety of chemical processes utilize hydrogen migration to rearrange the molecular structure and thereby alter its chemical and biological properties. Upon interaction of ultrashort laser pulses with the molecule, similar hydrogen dynamics can be triggered – for example a keto-enol tautomerism, where the hydrogen migration changes an aldehyde into an alcohol [8]. Thereby, light-induced isomerization might enable reaction pathways, which are not accessible by other means.

Previous research on isomerization investigated the possibility of laser induced isomerization of large hydrocarbon molecules [8–10]. For small hydrocarbons, also the isomerization time were determined, as for example in acetylene [11] or in allene [12]. Furthermore, the position of isomerization was tracked via isotope labeling [13–15]. In this thesis, the

isomerization of small hydrocarbons is not only passively observed but also its direction is actively controlled via the CEP of an ultrashort laser pulse. Additionally, the nuclear dynamics occurring during the laser-molecule interaction are investigated, with special focus on the isomerization process of acetylene (HCCH) to vinylidene (CCHH), which is visualized in "real" time. However, it is important to mention that not only an isomerization is triggered by the laser-matter interaction but rather a variety of molecular reactions is initiated.

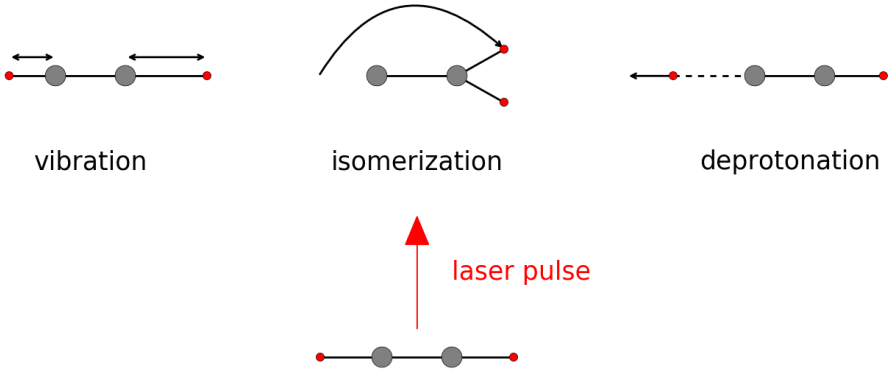

Figure 1.1: Schematic visualization of three different molecular reactions upon multi-photon-excitation by a laser pulse: vibration, isomerization, and deprotonation. The carbon atoms are depicted in grey and the hydrogen atoms in red.

In figure 1.1, three possible reactions of acetylene upon multi-photon ionization are schematically shown, i.e. vibration, isomerization, and direct dissociation of the CH-bond, called deprotonation. While vibrational motion occurs within all bonds simultaneously, their vibrational periods can differ from ∼10 fs in CH-bonds to ∼23 fs in the CC-bond. Such vibrations can also initiate the isomerization, where one proton is moving from one side of the molecule to the other side. And if the laser pulse provides enough energy, bond breaking can also occur as schematically shown in the case of deprotonation. It is important to keep in mind, that these possibilities interplay with each other, e.g. a vibration can trigger a dissociation or an isomerization. By investigating different dissociation channels, information on the various processes can be extracted. While the $HCCH^{2+} \rightarrow H^{+}+CCH^{+}$ channel is an example for deprotonation, the $HCCH^{2+} \rightarrow C^{+} + CHH^{+}$ channel indicates a preceding isomerization into the vinylidene isomer $CCHH$, where both hydrogen atoms are attached to the same carbon atom.

In order to observe such processes, an imaging system, for example a velocity-map imaging (VMI) spectrometer [16] or a reaction microscope (REMI) [17], is advantageous. While the VMI allows to measure the momenta of electron or ions with high statistics and

good resolution, it has certain limitations on the detection of coinciding fragments. The REMI, in contrast, allows the measurement of the 3D momenta of all charged fragments on a single-shot basis. Therefore, the achievable statistics is limited by the laser repetition rate. As different fragmentation channels have to be investigated to differentiate between the various molecular processes, a REMI is used throughout this thesis. To circumvent the intrinsic problem of low detection rates, the REMI is used in combination with a 10 kHz laser system.

To get further insight into the interplay between the different molecular processes, various laser fields and combinations of laser pulses were used throughout this thesis: Via single-pulse experiments, the dependence of ionization, deprotonation, and isomerization on the CEP (chapter 4) and intensity (chapter 5) were investigated. Using pump-probe experiments, the temporal evolution of the molecular structure, i.e. the bond lengths and their angles was measured via Coulomb Explosion Imaging (CEI), see chapter 6 and 7. Furthermore, a compact and flexible multi-color setup is presented in chapter 8, which allows to investigate various molecular processes by three different wavelengths. While the shown experiments are performed on small hydrocarbons (acetylene and allene), the obtained results can likely also be applied to larger hydrocarbon molecules.

List of publications with relevance to the work presented in this thesis

1. M. Kübel, R. Siemering, C. Burger, N. G. Kling, H.Li, A. Alnaser, B. Bergues, S. Zherebtsov, A. M. Azzeer, I.Ben-Itzhak, R. Moshammer, R. de Vivie-Riedle, and M. F. Kling, Steering Proton Migration in Hydrocarbons Using Intense Few-Cycle Laser Fields. *Physical Review Letters* **116**, 193001 (2016)

2. C. Burger, N. G. Kling, R. Siemering, A. Alnaser, B. Bergues, A. M. Azzeer, R. Moshammer, R. de Vivie-Riedle, M. Kübel, and M. F. Kling, Visualization of bond rearrangements in acetylene using near single-cycle laser pulses. *Faraday Discussions* **116**, 495 (2016)

3. M. Kübel, C. Burger, R. Siemering, N. G. Kling, B. Bergues, A. S. Alnaser, I. Ben-Itzhak, R. Moshammer, R. de Vivie-Riedle, and M. F. Kling, Phase- and intensity-dependence of ultrafast dynamics in hydrocarbon molecules in few-cycle laser fields. *Molecular Physics*, **115** (2017)

4. C. Burger, W. F. Frisch, T. Kardaś, M. Trubetschov, V. Pervak, R. Moshammer, B. Bergues, M. F. Kling, and P. Wnuk, Compact and flexible harmonic generator and three-color synthesizer for femtosecond coherent control and time-resolved studies. *Optics Express*, **25**, 31130 (2017)

5. C. Burger, A. Tul-noor, T. Schnappinger, H. Xu, P. Rosenberger, N. Harem, R. T. Sang, B. Bergues, R. de Vivie-Riedle, M. F. Kling, and I. Litvinyuk, Time-resolved nuclear dynamics in acetylene. **in preparation**

6. M. Kübel, C. Burger, R. Siemering, T. Naeser, R. de Vivie-Riedle, and M. F. Kling, Restructuring of Molecules with Lasers, *GIT Laboratory Journal* **7**, 37 (2017)

7. H. Li, N. G. Kling, T. Gaumnitz, C. Burger, R. Siemering, J. Schötz, Q.Liu, L. Ban, Y. Pertot, J. Wu, A. M. Azzeer, R. de Vivie-Riedle, H. J. Wörner, and M. F. Kling, Sub-cycle steering of the deprotonation of acetylene by intense few-cycle mid-infrared laser fields, *Optics Express* **13**, 14192 (2017)

Other publications

8. M. Kübel, A. Alnaser, B. Bergues, T. Pischke, J. Schmidt, Y. Deng, C. Jendrzejewski, J. Ullrich, G. G. Paulus, A. M Azzeer, U. Kleineberg, R. Moshammer, and M. F. Kling, Strong-field control of the dissociative ionization of N_2O with near-single-cycle pulses, *New Journal of Physics* **16**, 065017 (2014)

9. B. Bergues, M. Kübel-Schwarz, N. G. Kling, C. Burger, and M. F. Kling, Single-Cycle Non-Sequential Double Ionization, *IEEE Journal of Selected Topics on Quantum Electronics* **21**, 8701009 (2015)

10. F. Habel, V. Shirvanyan, M. K. Trubetskov, C. Burger, A. Sommer, M. F. Kling, M. Schultze, and V. Pervak, Octave spanning wedge dispersive mirrors with low dispersion oscillations, *Optics Express* **24**, 009218 (2016)

11. M. Kübel, C. Burger, N. G. Kling, T. Pischke, L. Beaufore, I. Ben-Itzhak, G. G. Paulus, J. Ullrich, T. Pfeifer, R. Moshammer, M. F. Kling, and B. Bergues, Complete characterization of single-cycle double ionization of argon from the nonsequential to the sequential ionization regime, *Physical Review A* **93**, 053422 (2016)

12. P. Rupp, C. Burger, N. G. Kling, M. Kübel, L. Seiffert, E. Rühl, C. G. Schäfer, M. Gallei, B. Bergues, T. Fennel, and M. F. Kling, Strong Near-Field Induced Molecular Processes on Nanoparticles. *2017 European Conference on Lasers and Electro-Optics and European Quantum Electronics Conference*, EG_4_3 (2017)

13. B. Ahn, J. Schötz, M. Kang, W. A. Okell, S. Mitra, B. Förg, S. Zherebtsov, F. Süßmann, C. Burger, M. Kübel, C. Liu, E. Di Fabrizio, H. Yanagisawa, D. Kim, B. Kim, and M. F. Kling, Attosecond-controlled photoemission from metal nanowire tips in the few-electron regime, *APL Photonics* **2**, 036104 (2017)

14. Y.F. Liu, K. Schnorr, G. Schmid, S. Augustin, S. Meister, H. Lindenblatt, A. Rudenko, M. Kübel, C. Burger, N. Stojanovic, R. Treusch, S. Düsterer, T. Jahnke, M. F. Kling, C. D. Schröter, T. Pfeifer, and R. Moshammer, THz Streaking of the Autoionization Dynamics of O_2 at the Free-Electron-Laser FLASH, *Journal of Physics: Conference Series* **875**, 032031 (2017)

15. M. Kübel, M. Arbeiter, C. Burger, Nora G. Kling, T. Pischke, T. Pfeifer, R. Moshammer, D. Bauer, T. Fennel, M. F. Kling, B. Bergues, Phase- and intensity- resolved measurements of above threshold ionization by few-cycle pulses, *submitted to J. Phys. B: At. Mol. Phys.*

16. P. Rupp, C. Burger, N. G. Kling, M. Kübel, T. Weatherby, L. Seiffert, E. Rühl, A. M. Azzeer, C. G. Schäfer, M. Gallei, T. Fennel, B. Bergues, M. F. Kling, Reaction nanoscopy: spatially resolved near-field-induced dissociative ionization of molecular adsorbates on nanoparticles, **in preparation**

2 Theory

In this chapter, the theoretical background concerning ultrashort laser pulses and their interaction with matter is given. First, the for this thesis relevant properties of ultrashort pulses are explained in section 2.1. Subsequently, the basic interactions of strong laser fields with atoms and molecules are presented in section 2.2.

2.1 Ultrashort laser pulses

The electric field of an ultrashort laser pulse is given by:

$$E(t) = E_0(t) \cdot \cos(\omega t + \phi), \tag{2.1}$$

where $E_0(t)$ is the envelope function, ω the carrier frequency, and ϕ is the carrier-envelope phase (CEP). Hereby, the envelope function can be written as:

$$E_0(t) = E_0 \cdot e^{-2ln(2)(\frac{t}{\tau})^2}, \tag{2.2}$$

with E_0 being the electric field maximum and τ the pulse duration, measured at the full-width half maximum (FWHM) of the electric field. Combining both equations, the electric field can be expressed by:

$$E(t) = E_0 \cdot e^{-2ln(2)(\frac{t}{\tau})^2} \cdot \cos(\omega t + \phi). \tag{2.3}$$

For very short laser pulses, where τ^{-1} is close to ω, the shape of the electric field is strongly influenced by the carrier-envelope phase ϕ. In figure 2.1, the electric field shape is shown for two different CEP's using typical pulse parameters, i.e. a pulse duration of 5 fs at a central wavelength of 790 nm. Clearly visible are the two components of the laser field: The envelope (depicted by the dashed line) and the carrier wave (shown as solid line). The individual velocities can be expressed by the wavenumber k and the angular frequency ω:

- group velocity: $v_g = \frac{d\omega}{dk}$
- phase velocity: $v_{ph} = \frac{\omega}{k}$

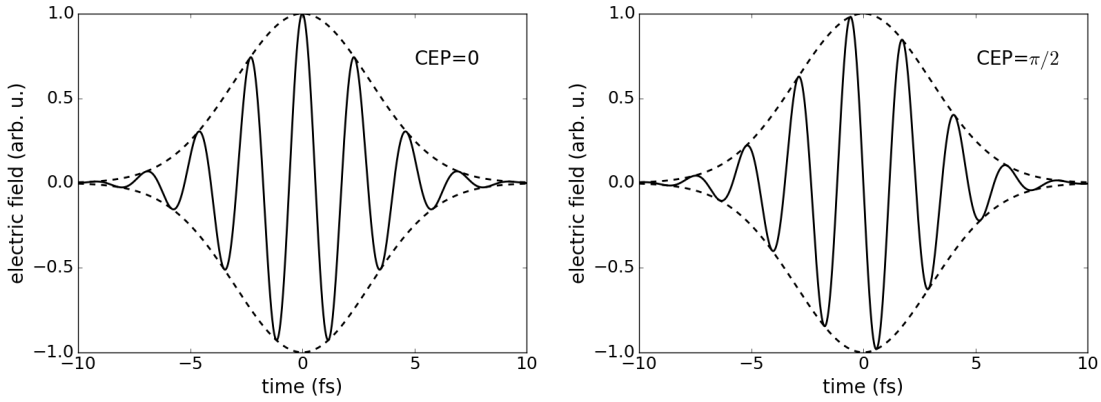

Figure 2.1: Few-cycle, 5 fs pulses, with a wavelength of 780 nm at a carrier-envelope phase of 0 and $\pi/2$.

While in vacuum both velocities are identical, in material a velocity difference occurs, which leads to a change in the CEP. Therefore, in practice, usually a thin transparent material is introduced into the beam path to vary the CEP. Such controlled CEP variations allow to shape the electric field, which thereby enables a steering of electronic motion on attosecond timescales [18]. This allows furthermore to control the generation of isolated attoseconds pulses [19] or to control molecular dissociation reactions [20].

While in this thesis mainly ultrashort laser pulses in the visible spectrum are utilized, chapter 8 utilizes second- and third-harmonic generation to efficiently create ultrashort pulses in the UV. To understand the shown experimental results, the basic principle of second- and third-harmonic generation is provided in the following.

2.1.1 Second- and third-harmonic generation

In order to reach low wavelengths (below 300 nm) with ultrashort pulse durations, usually non-linear processes such as second- and third-harmonic generation are utilized to convert a fraction of a high-power IR laser into the UV-regime. For this purpose, the laser is propagated through a non-linear medium, which provides either a $\chi^{(2)}$ or a $\chi^{(3)}$ nonlinearity. Thereby, χ corresponds to the material susceptibility. Depending on the strength of the susceptibility, the refractive index of the medium, and the required process, various materials can be used. In this thesis, β-barium-borate (BBO) crystals were used to allow for an efficient second-harmonic and sum-frequency generation from a 790 nm laser beam. The conversion efficiency of the second harmonic or third harmonic generation highly depends on multiple parameters as for example: spectral bandwidth, pulse duration, laser intensity, damage threshold of the material, and many more. Thus, a quantitative comparison of

the conversion efficiencies is complex and will not be discussed in this section. For further details on the experimentally acquired efficiencies refer to sections 3.3 and 8.2.

Second harmonic generation

Second harmonic generation can be understood as frequency doubling by absorption of two photons and emission of one photon with twice the energy within a $\chi^{(2)}$ material. To obtain an efficient conversion, a proper phase relation between the interacting waves has to be ensured within the crystal, also known as phase matching condition. In other words, one has to minimize any phase mismatch Δk, which can be expressed by $\Delta k = k_2 - 2k_1$, where k is the wavenumber of the fundamental (k_1) and second harmonic beam (k_2). This implies that the velocity of both beams should be identical, which occurs either in vacuum or in birefringent materials, where the velocity depends on the polarization. The here shown experiments are performed with birefringent crystals, where the emitted second harmonic photon has an extraordinary polarization, abbreviated by e_{out} with respect to the crystal axes. The polarization of the absorbed photons can be varied between ordinary polarized photons and extraordinary ones, abbreviated as $o_{1,2}$ and $e_{1,2}$, according to the material type:

- Type 0: $e_1 + e_2 \rightarrow e_{out}$
- Type I: $o_1 + o_2 \rightarrow e_{out}$
- Type II: $o_1 + e_2 \rightarrow e_{out}$

For all second harmonic generation processes presented in this thesis, type I BBO crystals, cut at an angle of 27.2 ° to guarantee proper phase matching, are used.
In order to increase the conversion efficiency thicker crystals can be used. This approach has the disadvantage that the phase matching condition is fulfilled for a narrower spectrum and is hence only suited for longer pulse durations. Thus, usually thin crystals (below 20 µm) or a focusing geometry are used to generate ultrashort SHG-pulses.

Furthermore, the second harmonic (395 nm) is more susceptible to chirp acquired in material due to chromatic dispersion (see 2.1.2). Therefore, all elements following the second harmonic generation (SHG) are produced as thin as possible ($\leq$ 1 mm).

Third harmonic generation

The third harmonic generation can be performed using a $\chi^{(3)}$ material, but due to its low efficiency, a cascaded process is used as follows: First, the second harmonic is created as described above within a BBO-crystal. Secondly, a sum frequency process in a $\chi^{(2)}$ crystal adds the fundamental and the second harmonic frequencies, so called sum frequency generation, into a third harmonic beam.

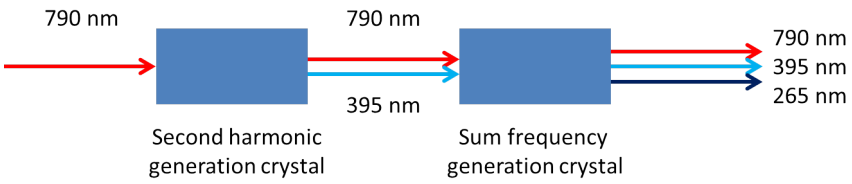

Figure 2.2: Cascaded process of third harmonic generation via frequency doubling and sum frequency mixing.

In this thesis, the sum frequency generation is performed in a BBO crystal. Compared to the second harmonic beam, the frequency tripled beam is even more sensitive to material dispersion. In the following section, an overview over the effect of chromatic dispersion is given to quantify this issue in more detail.

2.1.2 Chromatic dispersion

The optical dispersion of a material signifies the dependence of the group- and phase-velocity on the angular frequency. Such chromatic dispersion can be observed in wavelength dependent refraction as for example in rainbows or prisms.
The effect can mathematically be described by a Taylor expansion of the wavenumber k as a function of the frequency ω around the center frequency ω_0:

$$k(\omega) = k_0 + \frac{\delta k}{\delta \omega}(\omega - \omega_0) + \frac{1}{2}\frac{\delta^2 k}{\delta \omega^2}(\omega - \omega_0)^2 + ... \tag{2.4}$$

1. The zero order term corresponds to a phase shift independent of the wavelength.

2. The first order term includes the inverse of the group velocities v_g: $\frac{\delta k}{\delta \omega} = \frac{1}{v_g}$ and describes that each color travels with different speed through the material while the pulse shape is not influenced.

3. The second order term contains the so called group delay dispersion (GDD), which is a measure of the spectral phase of a laser pulse. In other words, for a GDD of 0 a laser pulse is temporally compressed, when the higher order terms are neglected, while a non-zero GDD signifies a chirped pulse.

4. Higher order terms describe how the spectral phase changes with propagation in the material.

For applications using pulses below 25 fs, it is important to consider even the higher order terms to achieve pulses close to the Fourier limit. In order to illustrate the effect of

chromatic dispersion, the resulting pulse durations of a 25 fs pulse transversing 1 mm of fused silica are shown in table 2.1 for different colors. Hereby, the pulse duration τ after the transmission through the dispersive medium can be calculated via:

$$\tau = \tau_0 \sqrt{1 + (4 \ln 2 \ \cdot \ \frac{GDD}{\tau_0^2})} \sim 4 \ln 2 \ \cdot \ \frac{GDD}{\tau_0}, \tag{2.5}$$

assuming a Gaussian pulse with a pulse duration τ_0.

Table 2.1: Effect of chromatic dispersion of 1 mm fused silica on an incoming pulse with a pulse duration of 25 fs at different central wavelengths. The group delay dispersion of a 1 mm thick crystal is calculated from the refractive index of fused silica found in [21].

wavelength (nm)	GDD (fs^2)	pulse duration (fs)
790	37	25.3
395	99	27.3
265	200	33.6

In table 2.1, the strong influence of chromatic dispersion on the pulse duration, especially for short wavelengths, becomes visible. Hence, any application of broadband laser pulses in the ultraviolet regime has to minimize the amount of glass or use special dispersive mirrors to counteract the acquired GDD.

The effects shown above are only considering the second order dispersion. To achieve pulses close to the Fourier limit, it is necessary to implement all orders of dispersion, as for example done in [22, 23] and in chapter 8, and simulate the complete beam path with the exact amount of dispersive material (glass, air, non-linear crystals, waveplates, ...).

2.2 Laser-matter interaction

In this section, the interaction of strong laser fields with atoms and molecules is explained in more detail. First, the basic ionization mechanism, above-threshold ionization is described in more detail. Secondly, the laser-atom interaction is explained by the Simple Man's Model (SMM) followed by the laser-molecule interaction.

2.2.1 Above-threshold ionization

Using strong laser fields allows to deposit large amounts of energy in atoms or molecules, leading to a single or even multiple ionization. In order to liberate an electron, the absorbed energy has to overcome the Coulomb potential of the atom or molecule. Depending on the applied intensities, the ionization process can occur in different regimes.

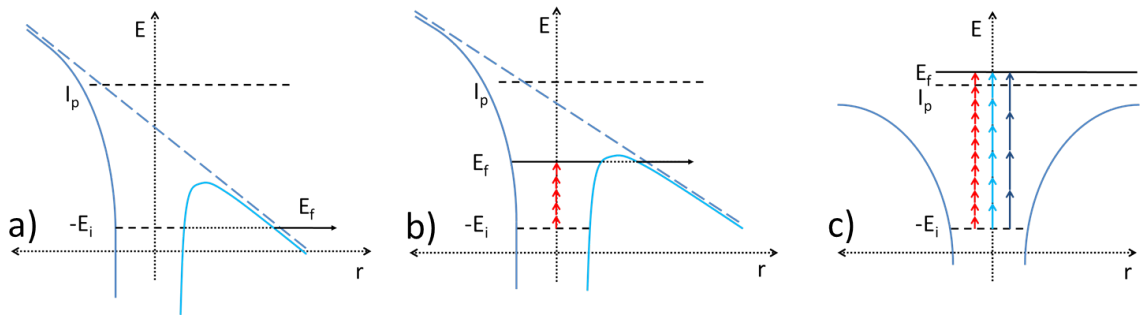

Figure 2.3: Schematic illustration of the different ionization regimes in a model atom: a) multi-photon ionization b) an intermediate regime and c) tunnel ionization. The light blue line indicates the atomic potential while the arrows represent the absorption of photons of different wavelength: red for 790 nm, light blue for 395 nm, and dark blue for 264 nm. E_i and E_f represent the initial and final energy, respectively, and I_p depicts the ionization potential of the model atom.

In figure 2.3, the relevant ionization regimes for this thesis are shown. For "low" intensities, see figure 2.3a), the ionization can be explained by the absorption of n photons exceeding the ionization potential ($n\hbar\omega > I_p$), called multi-photon ionization (MPI). The ionization rate of the MPI scales with I^n. As seen in figure 2.3a, the used wavelength plays an important role. While only four photons are required to ionize the model atom by a 265 nm laser beam, already twelve photons are necessary when a 790 nm laser is used.

Applying higher field strengths will bend the atomic/molecular potential such that a tunneling through the barrier becomes possible, called tunnel ionization (TI) – see 2.3b) and c). The ionization rate of the TI has an exponential dependence on the electric field. While the ionization time of TI is close to the field maximum of the carrier, the ionization via MPI is dominated by the envelope of the laser pulse.

The intensity at which the transition from MPI to TI occurs can be estimated by the Keldysh parameter γ [24]:

$$\gamma = \sqrt{\frac{I_p}{2U_p}}, \tag{2.6}$$

where U_p represents the ponderomotive potential – the quiver energy of a free electron in an oscillating electric field– which can be expressed by:

$$U_p = \frac{E_0^2}{4\omega^2}. \tag{2.7}$$

For $\gamma >> 1$, the processes can be explained by MPI, while for $\gamma << 1$ the tunnel ionization description is better suited. In formula 2.7, a strong wavelength dependence on the

transition regime becomes apparent. While for 790 nm light, this transition occurs around $10^{14}\,\mathrm{W/cm^2}$, it increases to $10^{15}\,\mathrm{W/cm^2}$ for 265 nm light. For the experimental conditions shown in this thesis, usually Keldysh parameters slightly above unity are used. Being in the transition region between MPI and TI makes a definite discussion within only one picture difficult. Nevertheless, a good qualitative agreement can be obtained by theoretical explanations based on tunnel ionization.

2.2.2 Simple Man's Model

The theoretical explanations are performed using the Simple Man's Model (SMM), which was first described in 1993 [25, 26] and is often used to explain the ionization process in strong laser fields. It consist of the following three steps:
1) An electron is tunneling out of the atomic potential and is subsequently accelerated away from the remaining core by the electric field.
2) In the second step, the electron is accelerated back to the remaining core when the field changes its sign within the next half period of the laser pulse.
3) As third step, the electron interacts with the ionic core in different manners:

- The electron recombines and emits a high energetic photon – called high harmonic generation (HHG) [18]. Thereby, the semiclassical picture predicts a maximal photon energy of $3.17\,U_p + I_p$ [27]. By applying spectral filtering, i.e. using the highest photon energies only, allows to create isolated attosecond pulses [28].

- The electron scatters of the core and thereby obtains up to $10\,U_p + 0.5\,I_p$, which can be calculated by quantum calculations [29, 30]. This scattering can also be used for holographic imaging of the core [31].

- It can also recollide with the ion and thereby liberate a second electron – called non-sequential double ionization (NSDI). For ionization processes in low energy regimes highly excited states can be reached by this process.

- It does not interact with the core, resulting in electron energies up to $2\,U_p$ [32], which can also be calculated by classical simulations [33]. This possibility is the most often occurring process and these released electrons are called "direct electrons".

While all processes can happen at the same time, their probabilities to occur are highly dependent on parameters as for example: target density, central wavelength, laser intensity, and many more. For the parameters used in this thesis, the process of electron recollision is especially important.

Using the SMM allows to simulate the processes in a semi-classical manner. After ionization, the electron can quiver freely in the electric field. The acquired momentum can

be calculated via the equation of motion:

$$v(t) = \frac{q}{m} \int_{t_0}^{\infty} E(t)dt + v_0, \tag{2.8}$$

where q is the charge of the electron, m is the mass, and v_0 is the starting momentum, which is zero in case of tunnel ionization such that $v_0 = 0$. Using the vector potential (A) as $A(t) = -\int_{t_0}^{\infty} E(t)dt$, equation 2.8 simplifies to:

$$p_{ele} = -qA(t_0) = +eA(t_0). \tag{2.9}$$

From this formula, one can derive that an electron born in a laser pulse will acquire an amount of momentum which is proportional to the vector potential at the birth time. Combining this information with the knowledge that the ionization probability depends on the electric field strength results in a final momentum distribution shown in figure 2.4.

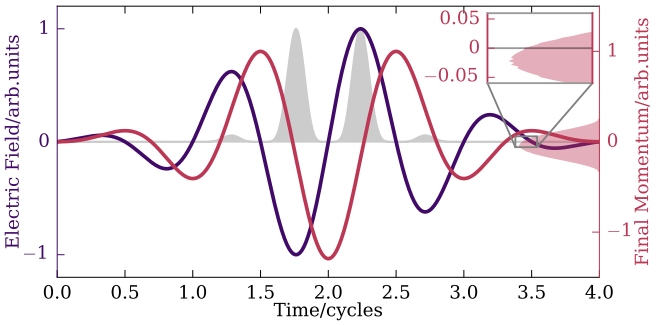

Figure 2.4: Final momentum (red) of a charge in a time dependent ultrashort electric field (purple) as a function of the release time. The probability for an electron to be released is shown in grey (in arbitrary units). The final averaged momentum distribution of electrons is shown in red on the right axis and magnified in the inset. The center is shifted to negative values as the laser pulse is a non perfect sin-pulse. Image is taken from [34].

Here, the field is shown in blue, the final electron momentum ($eA(t_0)$) in red and the ionization yield in grey. The final momentum distribution is depicted by the red filled area. It can be seen, that for highest fields the vector potential is close to zero and hence the momentum distribution is also centered around zero. As an ultrashort laser pulse is investigated, the final momentum distribution is not always centered around zero; here a laser pulse close to the perfect sin-pulse is investigated and thus the momentum distribution is only slightly negative (as highlighted by the inset). In order to simulate the ionization yield in dependence on the electric field strength, a empirical formula proposed by Tong *et al.* [35], which is based on a theory developed by Ammosov, Delone, and Krainov (ADK) [36], is used. Further information on the simulation and its implementation can be found

in [34].

While the SMM was explained for atoms it holds true as well for molecules. The subsequent molecular reaction of such laser excitations is described in the following section.

2.2.3 Laser-molecule interaction

In this section, the basic laser-molecule interactions relevant for this thesis are described. The main difference between atoms and molecules is that the binding energy of a molecule depends on the internuclear distance of its atoms, which are well visualized by the potential energy curves or surfaces. For diatomic molecules, potentials like the Morse potential can be applied. For more complex molecules, e.g. acetylene or allene, more sophisticated approaches, as described in the corresponding sections, have to be used. In the following, the Morse potential is shown to facilitate the understanding of the later on shown potential energy curves of acetylene and allene.

2.2.4 Morse potential

The Morse potential defines the potential energy of a diatomic molecule as a function of the internuclear distance. Due to its simplicity it is often used to explain fundamental processes occurring in molecules. The potential energy function $V(R)$ can be written as:

$$V(R) = D_e \cdot (e^{-2a\cdot(r-r_e)} - 2e^{-a\cdot(r-r_e)}), \tag{2.10}$$

with D_e being the well depth, a the well width, r the internuclear separation, and r_e the equilibrium distance. The first part of the formula describes the short-range repulsion, while the second term represents the long-range attraction. Using the Morse potential, the Schrödinger equation can be solved, resulting in the following eigenenergies $E(\nu)$:

$$E(\nu) = h\nu_0(v + 1/2) - \frac{[h\nu_0(v + 1/2)]^2}{4D_e}, \tag{2.11}$$

where ν is the vibrational quantum number and ν_0 is defined as:

$$\nu_0 = \frac{a}{2\pi}\sqrt{2D_e/m}, \tag{2.12}$$

with m being the mass of the particle. From equation 2.11, it becomes obvious that the energy-spacing is not equidistant as in the case of a harmonic oscillator $E(\nu) = h\nu$, but rather decreases with increasing vibrational quantum number. This difference in potential shape and energy-spacing can be seen in figure 2.5.

In this figure, the binding energy of a diatomic molecule is given as a function of the internuclear distance for both a harmonic potential (red) and a Morse potential (blue).

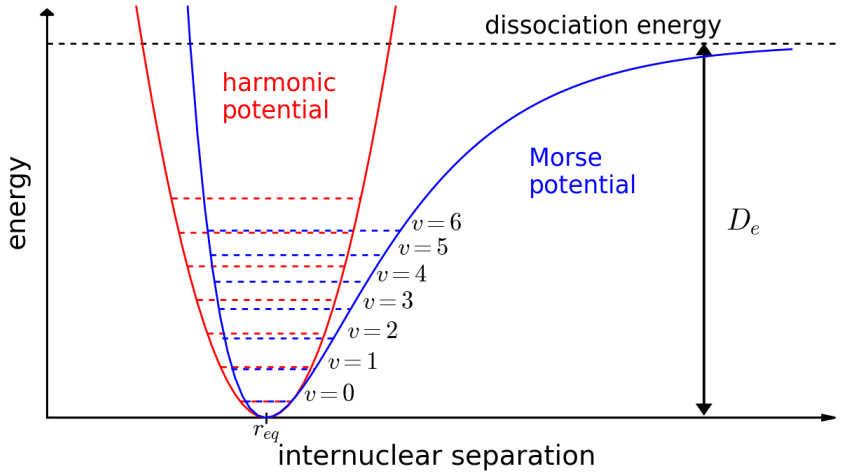

Figure 2.5: The Morse potential (blue) in comparison to the harmonic potential (red) as a function of the internuclear separation r. D_e describes the dissociation energy and v the vibrational quantum number.

While the harmonic potential is centered around the equilibrium distance r_{eq} the Morse potential has a strong repulsion for small distances and an asymptotic behavior for large distances. While in figure 2.5 only the vibrational states are shown, also various rotational states can be populated.

In the case of laser-molecule interaction, two scenarios can occur: first, for a small energy transfer, the molecule is excited into a higher vibrational state. With increasing quantum number, the internuclear distance and thereby also the period of a vibration increases. Second, for a higher energy transfer, the laser can excite the molecule into another electronic state. This transition of one electronic state to another is explained in more detail in the following by the Franck-Condon principle.

2.2.5 Franck-Condon principle

Additionally to the Morse potential, the Franck-Condon principle includes electronic and nuclear motion when describing the excitation of a molecule into a higher electronic state, e.g. $E_0 \rightarrow E_1$. It is based on the fact that electronic motion is faster than nuclear motion and hence, the probability of an electronic transition also depends on the nuclear vibrational levels.

In figure 2.6, the Franck-Condon principle is visualized for the vibrational energy states in two electronic states. It can be explained as follows: A wave-packet in the ground state of the neutral molecule ($v'' = 0$) can easily be excited to the second excited vibrational level ($v' = 2$), as exemplarily shown in figure 2.6 by the vertical arrow. A transition to other vibrational states is less likely to occur as they would include a change in the internuclear

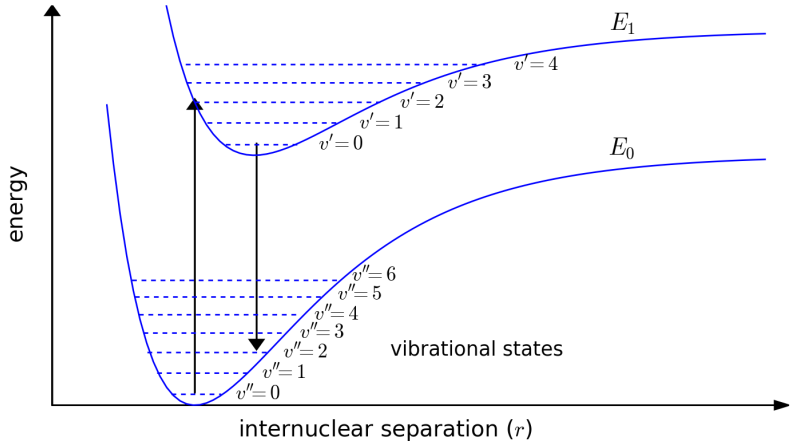

Figure 2.6: Franck-Condon principle: Electronic transitions occur exclusively vertically, as the electronic motion is faster than nuclear motion. Therefore, a wave-packet starting in the neutral (E_0) ground state ($v'' = 0$) populates preferentially the second vibrational state ($v' = 2$) of the excited electronic state (E_1).

distance, which requires a movement of the heavy atomic core. In other words, an electronic transition occurs more likely with increasing overlap of the vibrational wave functions of the corresponding energy levels.

The Franck-Condon principle holds true not only for the shown example of a diatomic molecule but as well for polyatomic molecules. In polyatomic molecules, however, the potential energy curve is replaced by a potential energy surface (PES) calculated using more complex models as explained in the corresponding chapters. Such an exemplary potential energy surface is shown in figure 2.7.

Here, the wave-packet is photo-excited from the ground state (S_0) to an excited electronic state (S_1). On the upper PES, the wave-packet evolves towards the conical intersection (CI), where it can undergo a transition back to the ground state. Such CIs of electronic states are thereby of outermost importance as they act as fast (sub-100 fs) and non-radiative pathway for most of the photo-chemical processes [37]. One CI of interest for this thesis is a transition of the $A^2\Sigma_g^+$ state to the $X^2\Pi_u$ state in the cation of acetylene. At this CI, the molecule can either isomerize to vinylidene or it remains in the acetylene configuration [38].

The above mentioned laser-excitation causes not only the population of a single excited state but usually a multitude of excited states are populated, which results in various possible molecular reactions. Therefore, a laser excitation will not always yield a vibration or a rotation of a molecule but rather a superposition of both. Hence, experimental investigations usually require high statistics to distinguish the occurring molecular reactions. The experimental techniques and setups necessary to investigate such reactions are described in the following chapter.

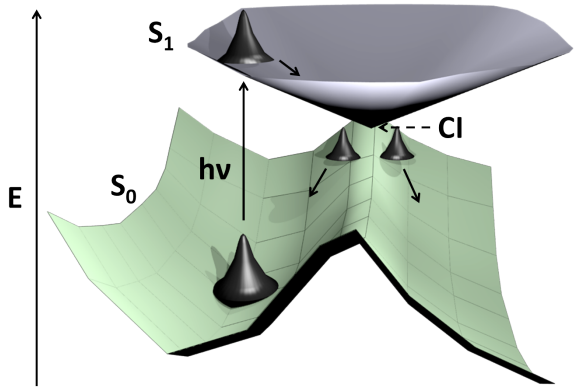

Figure 2.7: Exemplary potential energy surface including the subsequent molecular reaction: First, the wave-packet is transferred from the ground-state (S_0) to an excited electronic state (S_1) at the Franck-Condon region, depicted by the wave-packets. Secondly, the nuclear wave-packet evolves along the surface until it reaches a conical intersection (CI). Thirdly, the wave-packet can evolve in two different directions either towards the original stating point or away.

3 Experimental methods

In this chapter, the experimental methods used throughout this work are presented. In the first section, the laser setup is introduced in detail (section 3.1), i.e. the generation of ultrashort and phase-stable laser pulses and their subsequent amplification. In section 3.2, the most important optical components to modify and characterize the pulses are presented. Subsequently, several methods to conduct multi-pulse experiments are depicted in section 3.3. Lastly (section 3.4), the experimental chamber, i.e. the REMI, is introduced.

3.1 Laser setup

Since the first production of few-cycle laser pulses, the development of phase-stable laser pulses has been an active field of research, due to its applications in attosecond physics. In 2001, the first isolated attosecond pulses could be created, yet without active CEP stabilization [28]. Only two years later, in 2003, sufficient short term stability could be reached, which allowed Baltuška *et al.* "to control the attosecond temporal structure of coherent soft X-ray photons" [19]. Thanks to the invention of the feed-forward technique in 2010 (section 3.1.1), intrinsically carrier-envelope phase-stable laser pulses can currently be realized by the installation of commercially available modules into the laser system [39]. This phase-stability can be maintained throughout stretching, amplification, and temporal compression of the laser pulse [40]. In the following, the afore-mentioned module and its implementation in the laser system is discussed in more detail.

In figure 3.1, the laser setup with its major components is depicted: First, an oscillator generates ultrashort pulses with a repetition rate of 75.2 MHz, which are then phase-stabilized within the CEP4-module (Spectra Physics, former FEMTOLASERS). Subsequently, the pulses are amplified within a 9-pass amplifier. The corresponding operational details are described in the following sections.

3.1.1 Generation of ultrashort laser pulses

Within the oscillator, a Ti:sapphire crystal is pumped by a continuous-wave laser ("Verdi-V6", Coherent) at 532 nm with 2.85 W. Using the principle of Kerr-lens mode locking, it is possible to create ultrashort laser pulses of 7 fs pulse duration with a repetition rate

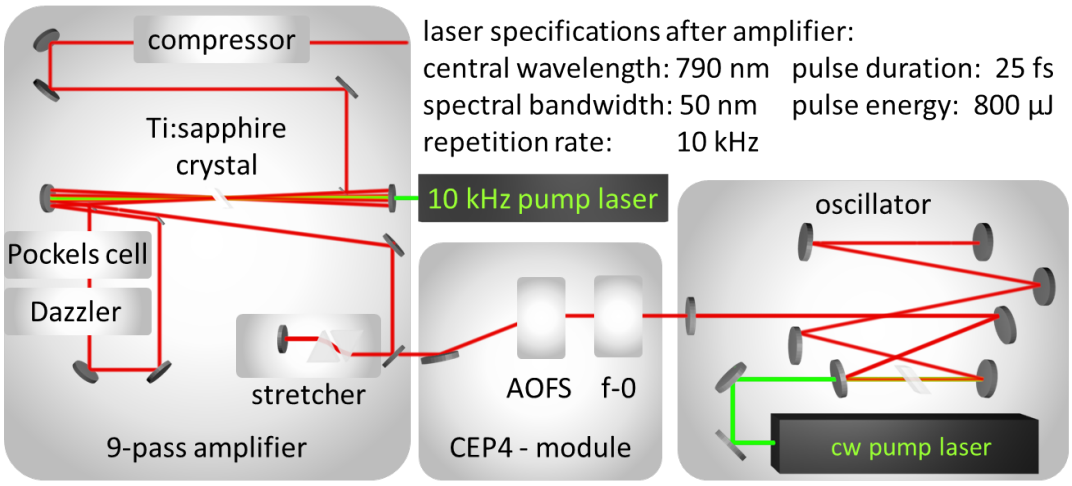

Figure 3.1: Schematic representation of the laser system. Ultrashort laser pulses are generated within the oscillator and subsequently phase-stabilized in the CEP4-module (not shown in detail). In the amplifier, the pulses are first temporally stretched, then amplified by four passes within a Ti:sapphire crystal. By the "Pockels cell" one pulse per pump laser shot is selected and spectrally shaped by the "Dazzler". Subsequently, this single laser pulse is amplified by five further passes through the crystal, and finally temporally compressed.

of 75.2 MHz at 270 mW average power, having a spectral range from 620 nm to 1000 nm (compare figure 3.3).

Feed-forward scheme

The feed-forward scheme allows to impose the same carrier-envelope phase on all laser pulses. This synchronization is based on a frequency shifting outside of the oscillator cavity.

A schematic drawing of the corresponding setup is shown in figure 3.2. First, the carrier-envelope offset frequency (f_{ceo}) is determined with an 0-to-f interferometer using the technique of self-referencing [42]. Depending on various parameters of the oscillator, e.g. temperature, humidity, and amount of dispersion within the beam path, the offset frequency f_{ceo} can vary from 0-75.2 MHz. Secondly, within an acousto-optic frequency shifter (AOFS), this offset frequency is compensated in the "-1st" order output f_{out}^{-1} of the AOFS:

$$f_{out}^{-1} = f_{in} - f_{AOFS}, \tag{3.1}$$

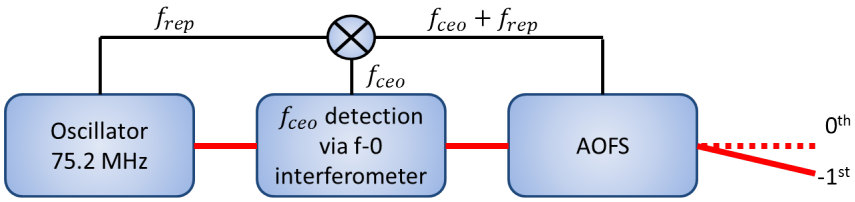

Figure 3.2: Schematic representation of the carrier-envelope phase-stabilization performed within the "CEP4"-module. The carrier-envelope offset frequency is detected within a f-0 interferometer and subsequently compensated by the "-1^{st}" order of the acousto-optical frequency shifter (AOFS). The resulting beam is intrinsically phase-stable such that excellent short- and long-term stability is achieved [41].

where f_{in} is the incoming laser frequency, and f_{AOFS} is the applied frequency of the AOFS, which can be chosen deliberately. Knowing that the input frequency can be written as $f_{in} = n \cdot f_{rep} + f_{ceo}$, equation 3.1 reformulates as follows:

$$f_{out}^{-1} = (n \cdot f_{rep} + f_{ceo}) - f_{AOFS} = (n \cdot f_{rep} + f_{ceo}) - (f_{rep} + f_{ceo}) = (n-1) \cdot f_{rep}. \quad (3.2)$$

Consequently, the output of the AOFS is independent of f_{ceo}, and hence all pulses have the same CEP. As an AOFS is most efficient in the range between 40 and 100 MHz, typically $f_{rep} + f_{ceo}$ is applied instead of only the offset frequency.

This feed-forward scheme is implemented in the attached "CEP4" module with an average output power of 150 mW. It was shown that this module can improve the short- and long-term stability of an oscillator such that a short term stability of 30 mrad during 20 s can be achieved and locked for over 24 hours [41].

3.1.2 Amplification and temporal compression

The phase-stable pulses after the CEP4-module are subsequently sent into a multi-pass amplifier ("FEMTOPOWER^{TM} HR 10 kHz CEP4", Spectra-Physics), where they are temporally stretched to avoid damaging the crystal from too high intensities. Subsequently, all pulses are amplified within a cryo-cooled Ti:sapphire crystal, which is pumped by a 10 kHz "DM50-527" laser (Photonics Industries) providing pulse energies of 5 mJ at 527 nm. After four passes of amplification, a single pulse is selected by a Pockels cell and spectrally shaped by an Acousto-Optic Programmable Dispersive Filter ("Dazzler", Fastlite). After five further passes, the laser pulses are temporally compressed by a grating compressor. Finally, the amplifier output provides the following parameters: a repetition rate of 10 kHz, a pulse duration of 25 fs, which is close to the Fourier limit of 24 fs, pulse energies of up to 800 µJ, and a central wavelength of 790 nm with 50 nm bandwidth (compare figure 3.3).

At this position, we can chose whether to use these pulses directly or to further compress the pulses temporally. In order to decrease the pulse duration to the few-cycle regime, the spectrum of the laser has to be broadened in a hollow-core fiber. Depending on the input pulse energy, the fiber is filled with ∼0.7 bar of argon (Ar) for pulse energies below 0.5 mJ, or ∼3 bar of neon (Ne) for energies above. In either case, a broadband supercontinuum supporting 4-fs pulses at 750 nm central wavelength is obtained. The pulses are temporally compressed using chirped multilayer mirrors [43] and fused silica wedges. The pulse duration is verified using a home-built transient-grating frequency-resolved optical gating (FROG) setup [44, 45]. After the temporal compression, the pulse energies are decreased to 250 µJ while the pulse duration can reach 4 fs.

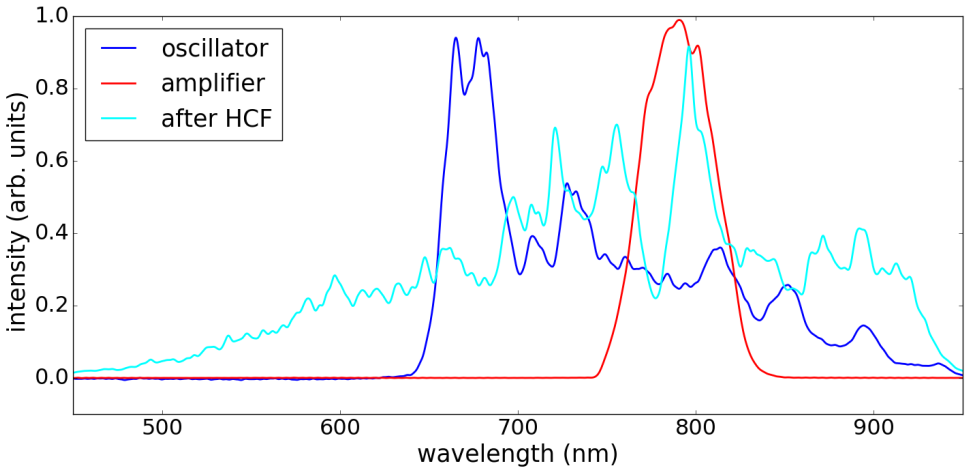

Figure 3.3: Spectra behind different positions of the laser setup: the oscillator (blue), the amplification by the 9-pass amplifier (red), and subsequent to the spectral broadening in the hollow core fibre (HCF) filled with argon and temporal compression by the chirped mirrors (cyan).

3.2 Laser pulse characterization

In order to characterize the laser pulses, the following techniques are applied: a spectrometer ("CCS200/M", Thorlabs) to measure the spectrum, a frequency-resolved optical-gating (FROG) to determine the pulse duration, and either an f-2f interferometer or a stereo-ATI phasemeter to extract the carrier-envelope phase. The determination of the CEP is explained in more detail in the subsequent section.

CEP detection

Ultrashort laser pulses can steer the motion of electrons and thereby trigger even nuclear motion. To allow for such a CEP-control, the waveform of the laser pulse has to be well defined. Within the last decade, two methods have been established: single shot phase-tagging by a stereo-ATI phasemeter and CEP measurement of phase-stable lasers by an f-2f interferometer [40, 45–47]. In the following, these two detection methods are presented in more detail.

CEP tagging using the Stereo-ATI phasemeter

In 2001, Paulus *et al.* [48] demonstrated the dependence of noble gas photo-ionization on the carrier-envelope phase of ultrashort laser pulses. Within the next two years, it was found that low- and high-energy spectra show different CEP-dependence [49]. Investigating these dependencies allows to determine the relative CEP for a given ratio of asymmetries between low- and high-energetic electrons [49]. After several years of development, the single pulse CEP-detection became feasible – even for kHz repetition rates [46, 47]. The experimental realization of this single shot CEP detection, the stereo-ATI phasemeter and its major components, is depicted in figure 3.4. A laser pulse ionizes atoms within a gas

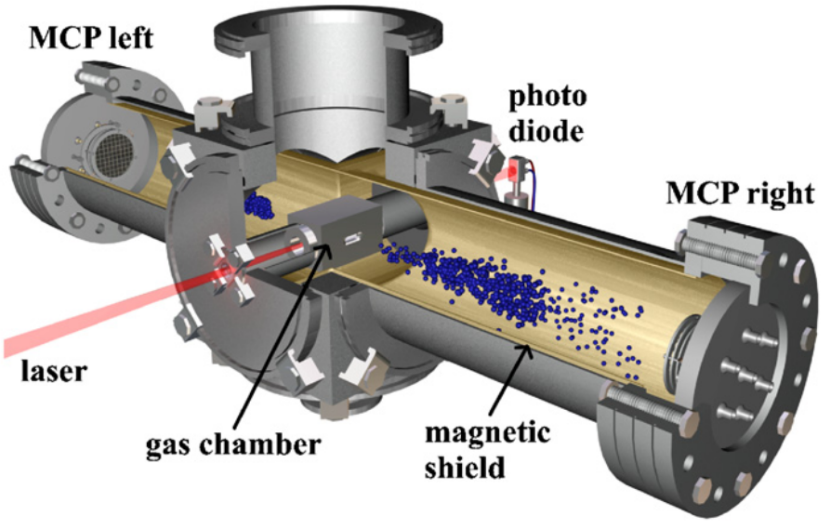

Figure 3.4: Schematic drawing of the stereo-ATI phasemeter. A strong laser pulse ionizes gas molecules, typically xenon atoms. The thereby released electrons are detected by two pairs of MCPs, which record the timing and the yield of electrons along the laser polarization direction. The figure was taken from [50].

chamber and thereby releases electrons to the right and the left detector. Depending on

the CEP, an asymmetry in the electrons emission direction and their corresponding energy is recorded. The energy of the electrons can be deduced from their time-of-flight – low energetic electrons will arrive later on the detector than highly energetic ones. The photodiode behind the chamber is used to provide a precise timing for the electron detection. The magnetic shield protects the electrons from external magnetic influences which would bend their trajectories and thereby might modify the detection efficiency. To quantitatively

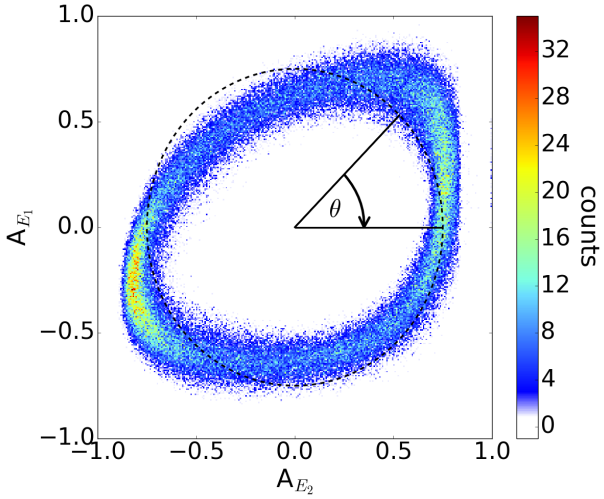

Figure 3.5: Parametric asymmetry plot of 180000 laser pulses. A_{E_1} and A_{E_2} represent the asymmetry parameters in the low and high energy region, respectively.

measure the phase Φ, the asymmetry parameter A is calculated for two distinct energy regions (E_1, E_2):

$$A_{E_1} = \frac{N_{left,1} - N_{right,1}}{N_{left,1} + N_{right,1}} \sin(\Phi + \Phi_0) \qquad A_{E_2} = \frac{N_{left,2} - N_{right,2}}{N_{left,2} + N_{right,2}} \cos(Phi + \Phi_0),$$

where N is the number of detected electrons on the left and right detector, respectively. From these two asymmetry parameters the polar angle θ is calculated by:
$\theta = \arctan(A_{E_1}/A_{E_2})$. In figure 3.5, a graphical representation of the asymmetry parameters and the angle θ depict the above mentioned interplay. From θ the CEP can be recalculated via $\Phi = \theta - \Phi_0$ for measurements with sufficient statistics, i.e. more than 10^4 shots, which corresponds to a measuring time of 1 s. For further information on the retrieval of $\Phi(\theta)$ and the technical details of the phasemeter please refer to [50, 51]. It is furthermore important to notice that this technique requires around 30 µJ pulse energy [50], which might be disadvantageous for high-repetition laser systems or experiments, which require high pulse energies.

Phase measurement via the f-2f interferometer

Another technique to measure the CEP is based on a purely optical setup using interferometry. A broadband pulse is hereby spectrally overlapped with a second harmonic beam created by the longer wavelengths of the fundamental beam. In the overlapping spectral range, which is usually around 470 nm for a Ti:sapphire laser, the observed interference fringes allows retrieving the CEP by Fourier filtering [52], which is described in [45] by the analysis of: $\Phi = 2\Phi_{940nm} - \Phi_{470nm}$.

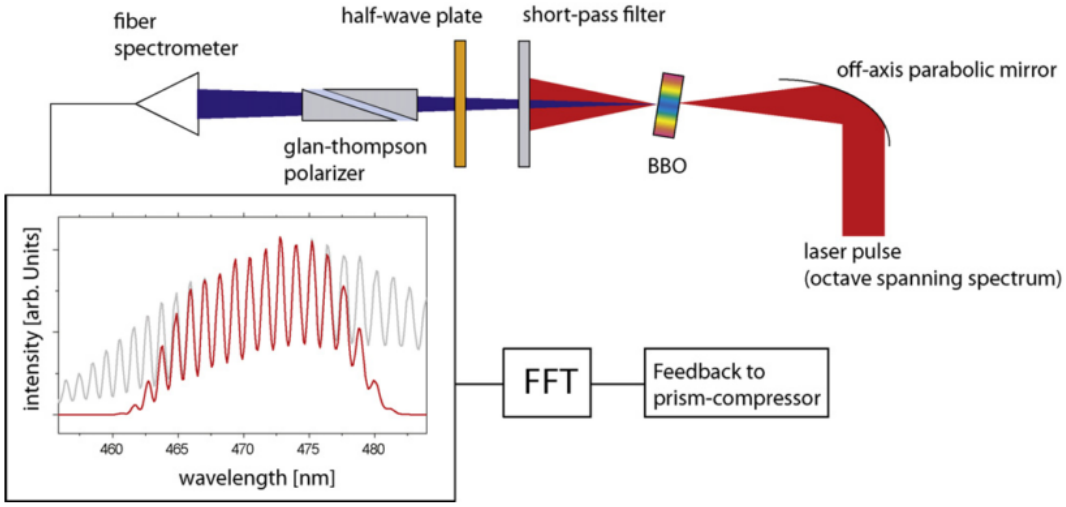

Figure 3.6: Schematic drawing of the f-2f interferometer. The octave spanning beam is sent onto a BBO crystal, which produces a second harmonic beam of the higher wavelengths. Subsequently, the lower wavelengths are spectrally filtered and analyzed on their corresponding polarizations. The spectrum is recorded by a fibre spectrometer ("USB2000+",Ocean Optics). The figure was taken from [45].

The experimental realization is depicted in figure 3.6. A laser pulse with an octave spanning spectrum, i.e. a fraction of the hollow-core fiber output, is used to create the second harmonic of the higher wavelengths in a BBO crystal, which is directly overlapped with the spectrally broad fundamental beam. The fringe pattern is then detected by a spectrometer and analyzed using a Labview program [45]. One of the major drawbacks of the f-2f analysis is the low acquisition rate due to the slow data transfer from the spectrometer to the computer. Recently, first measurements showed the feasibility of a single-shot detection at an acquisition rate of 10 kHz [40]. Using such a single-shot f-2f device in the future would be advantageous compared to the Stereo-ATI phasemeter as the required pulse energies are with 16 µJ considerably lower.

3.3 Multi-pulse experiments

Within this thesis, two types of multiple pulse experiments were performed. Firstly, pump-probe experiments using few-cycle pulses were conducted to reveal the temporal evolution of molecular processes. The high temporal resolution of few-cycle pulses allowed to track the nuclear motion in acetylene. Secondly, a multiple-color pulse synthesis scheme was used, which enabled the control of electronic motion on sub-cycle time scales.

3.3.1 Near single-cycle pump-probe scheme

To investigate the temporal evolution of atomic or molecular processes, a pump-probe scheme with ultrashort laser pulses is most commonly applied. Such a few-cycle pump-probe experiment is a challenging task as the ultrashort pulse duration of both pulses has to be maintained while achieving high spatial and temporal precision of both arms with good reproducibility. In order to fulfill these requirements, a Mach-Zehnder interferometer is used within this thesis, shown in figure 3.7.

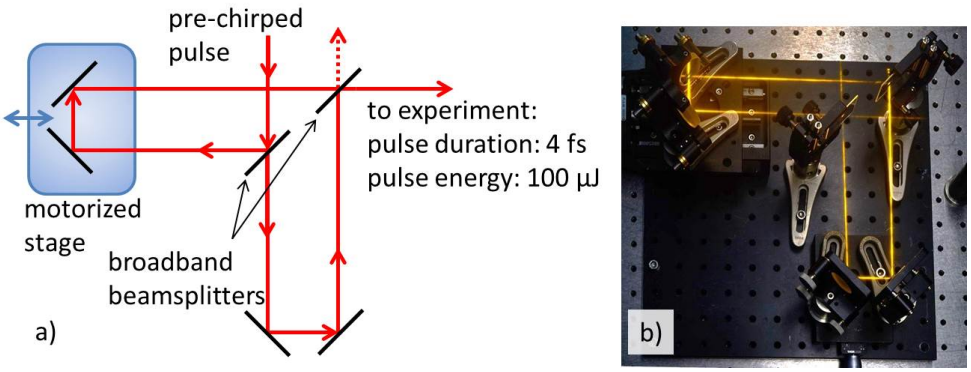

Figure 3.7: Schematic setup (a) and photograph (b) of the Mach-Zehnder interferometer used for pump-probe experiments with ultrashort laser pulses. The motorized stage allows sweeping the pump-probe delay in an automatized manner. To record this photograph, a long exposure time was used during which fog was introduced to enhance the scattering of the laser light and hence visualize the laser beam. Its yellow color is due to the broad spectrum extending from 500-900 nm.

Thereby, the laser is split into two identical parts by a 50:50 beamsplitter. Subsequently, each arm is redirected onto a second beamsplitter, where both arms are recombined. The beamsplitters are only 1 mm thick, which guarantees their mechanical stability while minimizing the dispersion. To ensure that the output of each arm is identical, the pulse characterization is performed for each arm separately. Within one arm, an automatized linear translation stage with nanometer accuracy is introduced, which allows to precisely

adjust the pump-probe delays. The position information of the stage is continuously monitored and combined with other experimental data (see section 3.4.1). To compensate for the dispersion acquired within the interferometer, the pulses are pre-compressed by the chirped mirrors such that a pulse duration of 4 fs in the experimental chamber is achieved.

3.3.2 Multi-color experiments

For multiple-color coherent-control experiments, different approaches were reported to produce ultrashort pulses in the UV range [53–55]. As many molecules have strong absorption bands below 300 nm, in particular the creation of ultrashort laser pulses in this spectral range, which would enable resonant electronic excitations, was investigated. As the here used laser-system has only moderate pulse energies (due to the high repetition rate) a frequency tripling system in bulk media was employed to efficiently generate the third harmonic around 264 nm. The principle is based on the subsequent generation of second and third harmonic (see section 2.1.1): First, the amplifier output is frequency doubled within a BBO crystal. Subsequently, the fundamental and the second harmonic are overlapped within a second BBO crystal, where via sum-frequency generation the third harmonic is created. The resulting spectra are shown in figure 3.8. Even though the individual compo-

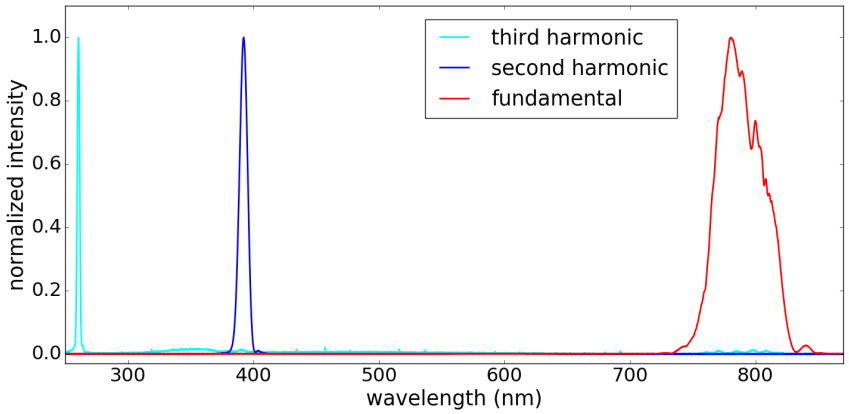

Figure 3.8: Spectra of the fundamental, second and third harmonic. Clearly visible is the limited spectral bandwidth, which results in longer pulse durations of 35-61 fs.

nents provide a rather small bandwidth, each component is sufficiently broad to support pulse durations of 35-61 fs. For more details on the creation of the individual harmonics, the subsequent pulse shaping, and the pulse characterization – including the calculations – see chapter 8. Using this approach, a high conversion efficiency to the third harmonic of ∼11 % was achieved.

3.4 Reaction microscope

In order to investigate the laser-matter interaction in the gas phase, various experimental setups are used. While an electron time-of-flight (TOF)-spectrometer provides only the information on the electrons and their energy, the more complex velocity-map-imaging setup measures the 3D momenta of electrons or ions. In this thesis, however, a reaction microscope (REMI) was employed, which enables to retrieve the 3D momentum of electrons and ions simultaneously. Furthermore, coincidences between all charged fragments of one laser shot are detected. Only by applying this coincidence technique it is possible to investigate the molecular processes, which are studied in this thesis. In this section, the main working principle and all relevant details for the presented experiments are described. For a more detailed overview on reaction microscopes and their application, refer to the review article by Ullrich *et al.* [17].

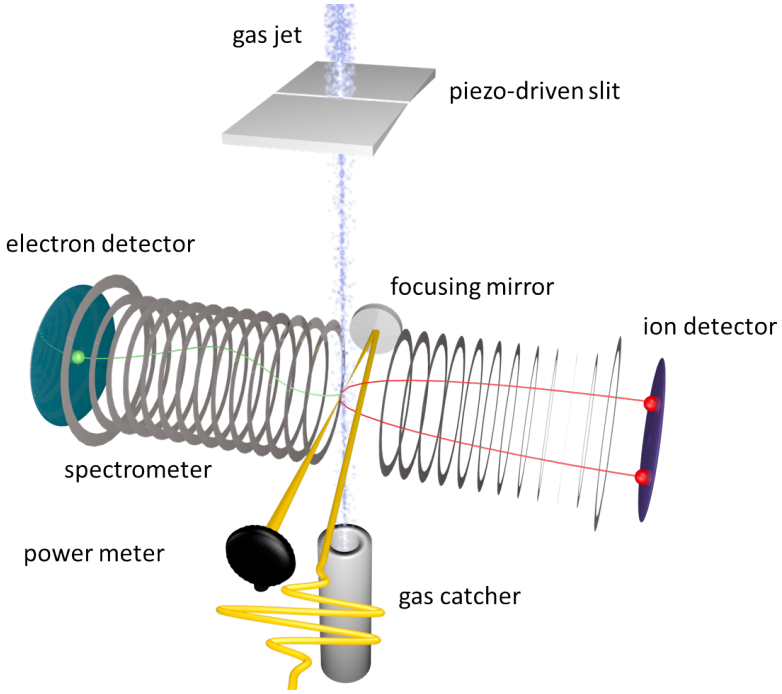

Figure 3.9: Experimental setup of a reaction microscope. The gas jet consisting of the target gas is introduced from the top and intersected in the center of the chamber with the laser pulse. Any charged particle, which is created by the laser-matter interaction, is extracted by a static electric field (spectrometer) onto position- and time-sensitive detectors. Laser parameters, e.g. power and carrier-envelope phase, are recorded simultaneously.

In figure 3.9, the main components of a reaction microscope are shown. A strong laser pulse is intersected with a gas jet, which can consist of any gaseous compound. The charged

particles arising from this interaction are extracted by a homogeneous static electric field, which is created by a spectrometer, onto time- and position-sensitive detectors. To account for the higher velocity of the electrons, an additional magnetic field is applied by Helmholtz coils, which bends the electrons on circular trajectories. Applying the magnetic field increased thereby the detection efficiency of electrons with an initial velocity perpendicular to the spectrometer axis.

Furthermore, the coincidences between all detected particles from one shot can be recorded, enabling us to reconstruct the molecular structure at the time of Coulomb explosion. In order to have a low amount of "false" coincidences, i.e. ionization of multiple atoms and molecules, the target density and the backing pressure have to be sufficiently low, which is one of the main challenges in REMI measurements.

To achieve such good background pressures, all elements within the vacuum chamber are built to be ultra-high vacuum (UHV) compatible. To improve the pressure below 10^{-9} mbar, the complete chamber is "baked" at $\sim$100 °C for more than 24 hours to desorb the water from the chamber walls. After the heating, a final pressure below 10^{-10} mbar is reached. While this pressure can be maintained throughout all experiments, the heating process has to be repeated after venting.To maintain the low background pressure, the gas jet is differentially pumped and the target gas in the main chamber is directly extracted by the "gas catcher".

It is worth mentioning, that reaction microscopes are not only used to investigate laser-matter interactions but also to study electron impact ionization [56] or ion collisions [17, 57]. In this thesis, however, only the relevant aspects of the REMI setup for the presented experiments are explained in more detail – with particular focus on the coincident ion detection.

Gas source

The preferred target in reaction microscopy is a supersonic gas jet with very low target density of around 10^9 particles per cm^3 [58]. The setup of the gas jet consists of a supersonic nozzle with a diameter of 5-50 µm, a skimmer pair (200 µm diameter), and a piezo-driven slit, which varies the final width of the gas jet. Particularly in intensity-dependent measurements, the automation of the slit width becomes important, as it permits to control the amount of particles in the interaction region and hence the number of created ions and electrons. For more information on the automation of the slit depending on the applied laser intensity, see chapter 5. By minimizing the diameter of the supersonic nozzle, a uniform velocity distribution of the target gas is achieved. To fabricate such nozzles, laser pulses are focused onto a 200 µm thick metal plate, where a small hole is "drilled" by laser ablation. Usually a nozzle diameter of 30-50 µm is used ensuring enough particle density at the interaction region. Only for experiments with very light gases, e.g. helium, a nozzle

of 6 µm diameter is used to minimize the throughput of the nozzle.

Recoil ion detection

Once the atom or molecule from the gas target is ionized by the laser pulse, the resulting ions are accelerated by the static electric field onto the ion detector. The spectrometer field is created by a stack of 32 equidistant ring electrodes with 100 Ω resistors in between, resulting in a homogeneous field distribution. At the end of the spectrometer, a first mesh maintains the homogeneity of the electric field. To achieve a high detection efficiency independent of the initial momentum, a second mesh accelerates the ions onto the detector. The detector consists of two parts: a stack of chevron micro-channel plates (MCPs), providing the TOF (t_z) information, and a two-dimensional delay-line detector (DLD) (RoentDek) with a line-spacing of 1 mm, yielding the perpendicular position information (x, y). A particle impact on the MCP creates an electron avalanche, which is further accelerated onto several lines of the delay-line detector. Detecting the electrons on multiple lines allows for a sub line-width resolution of the DLD, around 50 m [59]. A full 3D momentum (p_x, p_y, p_z) reconstruction becomes possible by combining the detected position from the DLD and the timing information at the MCP. For a more technical description of the detector stack and possible improvements, refer to Jagutzki *et al.* [59, 60]

Another important aspect is the single particle detection efficiency η_{MCP}. For this, the MCP geometry is crucial as the particle has to impact within a channel to create an electron avalanche, which limits the efficiency depending on the MCP geometry to around 50-60 %. For multiple particle detection, the total efficiency is calculated by $\eta_{tot} = (\eta_{MCP})^N$, where N is the number of detected particles. Hence, for a four-fold coincidence, the efficiency is reduced to 6 %. Additional complications arise from the "dead" time of 10 ns of the delay-line detectors. This "dead" time occurs after a particle was detected, leaving the detector insensitive to further particle impacts for ∼10 ns and thereby decreases the total efficiency further. As usual time-of-flights are within the microsecond regime, this "dead" time becomes only important for coincident detections with two particles of similar mass, e.g. C^+ and CH_2^+, see figure 4.3. Thus, it is very challenging to measure processes which include multiple particle coincidences with good statistics.

3.4.1 Data acquisition

Once a particle hits the detector, the MCP and the DLD will yield a signal, which is amplified by a fast-amplifier ("FTA820", ORTEC) and rectified by a constant fraction discriminator (CFD) ("QUAD CFD 935", ORTEC). The timing of the signal is extracted by a time-to-digital converter (TDC) ("V1290N", CAEN). Further external parameters, e.g. the CEP, the power, or the stage positions are recorded as voltages in the analog-to-

digital converter (ADC) ("V785N", CAEN). By using analog window filters ("4-8 logic", CAEN; "GG8000", GSI), the TDC and ADC are only read out if a particle is detected within the applied time window. In this thesis, that time window was often chosen such that the signal of the single ionization was not recorded, reducing the overall count rate significantly. Once this condition is fulfilled, all timing information of this laser shot TDC and all external parameters from the ADC are read out and the data are transferred to the computer, where they are monitored and eventually saved [61]. To monitor and analyze the data, the open source program Go4 is used [62]. Using the length of the spectrometer, the voltage gradient and the time and position information, the 3D momenta of each particle are calculated. Furthermore, Go4 allows to set coincidence filters to distinguish between different coincidence channels through, for example, using the photoion-photoion coincidence (PIPICO) plots (see figure 3.10). For these channels, the 3D momenta of all detected particles are saved together with the external information, acquired in the ADC, on a single shot basis. Each coincidence channel is then evaluated individually on the delay-, intensity-, or CEP-dependencies by self-written computer programs in Python to obtain the final plots shown in this thesis.

3.4.2 Coulomb explosion analysis

Coincidence filtering

Within this thesis mainly ion-ion coincidences recorded with the REMI are shown. In order to filter these coincidences from all other signals the following procedure is applied. First, the time-of-flight information is used to identify the fragments – a time window is applied, which includes all possible TOFs of the fragment. Subsequently, only events having two or more counts within one laser shot are investigated, which is depicted via the PIPICO representation. Lastly, only coincident events fulfilling the law of momentum conservation are selected for further analysis.

Figure 3.10a) presents a PIPICO plot of acetylene, where the TOF of the first ion is shown together with the TOF of the second arriving ion. In figure 3.10b), the TOF's are converted to the mass over charge ratio (m/q) to facilitate the identification of the fragments. Two major features can clearly be distinguished: First, the straight lines (horizontal and vertical) at mass over charge ratios of: 1 (H^+), 2 (H_2^+), 13 (CH^+ or $C_2H_2^{2+}$), 18 (H_2O^+), and 26 ($C_2H_2^+$), which correspond to coincidences between fragments of often created ions, e.g. hydrogen or acetylene. These lines are also called "false" coincidences, as they result from two independently ionized particles within one laser shot. Secondly, diagonal lines are observed, which originate from Coulomb explosions of the parent molecule. Depicted in the graph are the three major coincidence lines, which will be discussed throughout this thesis:

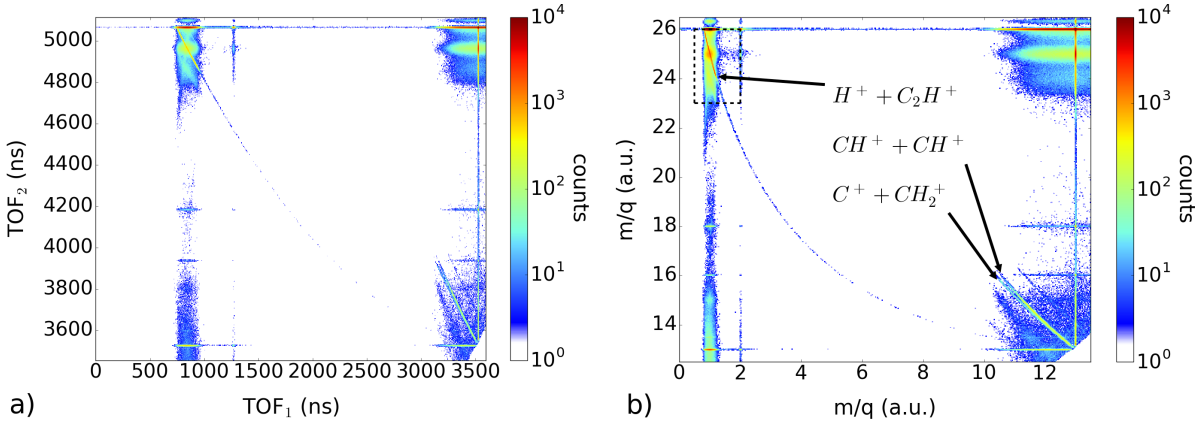

Figure 3.10: Photoion-photoion coincidence spectrum of acetylene measurement. a) Depicted is the time-of-flight (TOF) of the first ion against the TOF of the second ion. b) Same as a) but the TOF's are converted into the mass over charge (m/q) ratio to facilitate the identification of the fragments. The discussed coincidence channels are highlighted by arrows. The black dashed box represents the area of interest of the deprotonation channel, which is shown in figure 3.11. The lower right area, where the symmetric break-up channel and the isomerization channel are observed, is investigated in more detail in figure 4.3.

- Deprotonation: $C_2H_2^{2+} \rightarrow H^+ + CCH^+$. The deprotonation channel is clearly visible in the top left area. The long tail results from a meta-stable state of acetylene, which dissociates only after several microseconds.
- Symmetric break-up: $C_2H_2^{2+} \rightarrow CH^+ + CH^+$.
- Isomerization: $C_2H_2^{2+} \rightarrow C^+ + CH_2^+$. The isomerization channel is very close to the symmetric break-up channel due to their similar mass and hence both channels are difficult to distinguish. For further details see chapter 4.

Using the example of the deprotonation, the coincidence filtering technique is explained in more detail.

In figure 3.11a), the PIPICO spectrum of the deprotonation is magnified to visualize the most important features. While the coincidence line is clearly visible, a second blurred diagonal line below indicates the fragmentation channel $C_2H_2^{2+} \rightarrow H^+ + C_2^+ + H$. As the neutral hydrogen is not detected, the momentum sum of the coincidence is not equal to zero and hence the line is blurred. Furthermore, many "false" coincidences can be seen between the fragments $C_2H_2^+$ (m/q=26), C_2H^+ (m/q=25), and H^+ (m/q=1). In order to select exclusively the events resulting from the same parent molecule, the momentum of

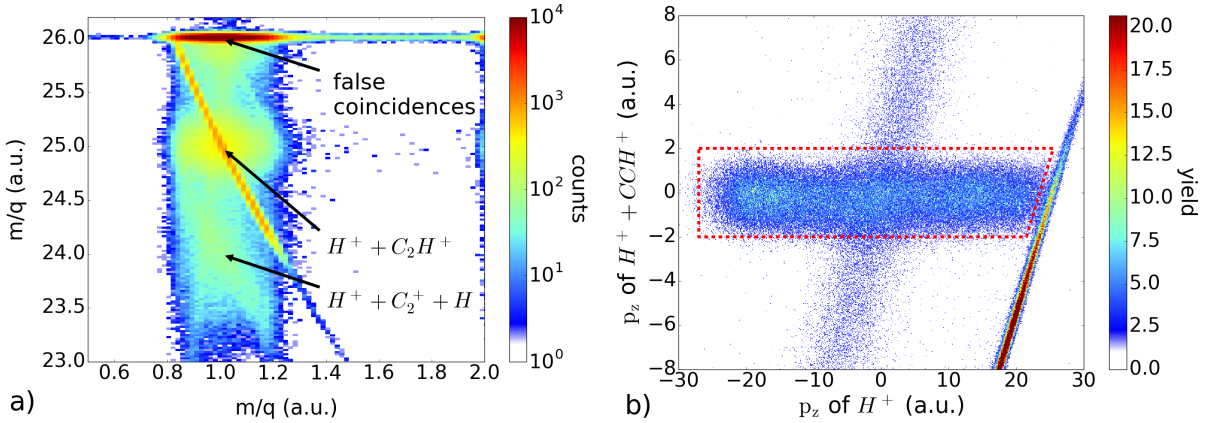

Figure 3.11: a) Photoion-photoion coincidence spectrum of the deprotonation in acetylene. The TOF's are already converted to m/q ratio. b) Graphical representation of the coincidence filtering. Only events within the red dashed box are considered for further analysis of the deprotonation channel. More details are found in the text.

one fragment is depicted versus the momentum sum of all fragments, see figure 3.11b). If the momentum is conserved, the momentum sum p_z of $H^+ + CCH^+$ should be close to zero – independent on the momentum of the hydrogen momentum. These events are then filtered, as depicted by the red dashed box, and used for further analysis. The diagonal lines in figure 3.11b) result from the "false" coincidences $C_2H_2^+$ with H^+ (right diagonal line) and C_2H^+ with H^+ (central diagonal line). For convenience only one momentum direction (p_z) is shown here, while the filtering is applied in all three dimensions.

Despite this filtering, some "false" coincidences cannot be distinguished from the correct signal. In order to keep a reasonable ratio between the real and the "false" coincidences, the count rate should not exceed one laser-molecule interaction per laser shot. Usually a count rate below 5 kHz was used, such that "false" coincidences occur only with very low probability.

Kinetic energy release

Once the coincidences are filtered and the 3D momenta are retrieved, the kinetic energy release (KER) of the coincidence can be calculated. Hereby, the KER is given by:

$$\mathrm{KER} = \sum_{n=1}^{N} \frac{p_n^2}{2 \cdot m_n}, \tag{3.3}$$

where N is the number of fragments per coincidences channel, m_n the mass of the coincidence fragment, and p the momentum, which is given by $p = \sqrt{p_x^2 + p_y^2 + p_z^2}$. Considering

the Go4 momentum output in atomic units ($p = p[a.u.]$), an example KER calculation of the symmetric breakup channel of acetylene ($C_2H_2^{2+} \rightarrow CH^+ + CH^+$) is shown in equation 3.4:

$$\mathrm{KER}_{\mathrm{CH-CH}}[\mathrm{eV}] = \left(\frac{p_{1,x}^2 + p_{1,y}^2 + p_{1,z}^2}{2 \cdot 13} + \frac{p_{2,x}^2 + p_{2,y}^2 + p_{2,z}^2}{2 \cdot 13} \right) \cdot \frac{27.2}{1822.9}. \tag{3.4}$$

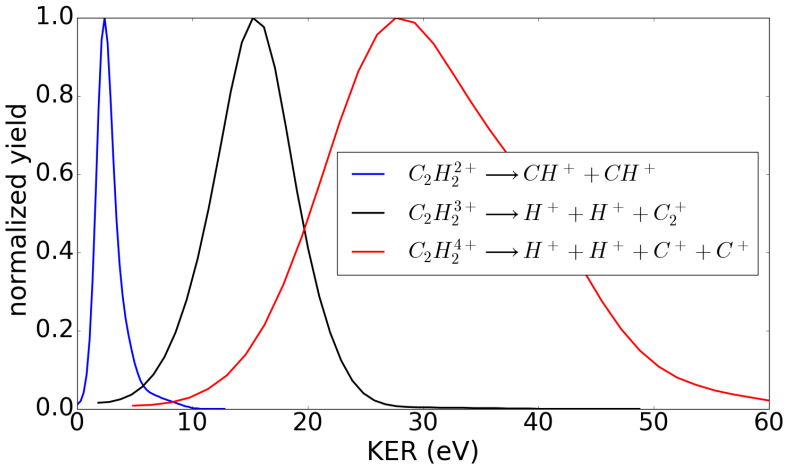

Figure 3.12: Kinetic energy release (KER) for different coincidence channels. The two-fold coincidence channel is depicted in blue, the three-fold coincidences in black, and the four-fold coincidence channel in red. By increasing the amount of fragments, the average KER is enhanced while simultaneously the distribution becomes broader.

Using this formula, example KER distributions for different coincidence channels are shown in figure 3.12. The symmetric breakup (depicted in blue) results a KER distribution centered around 4 eV. A quadrupole coincidence (shown in red) in contrast results in higher KERs as not only one bond is broken but three bonds break in the Coulomb explosion. Additionally to the total KER, also the distribution provide valuable information. If molecules dissociates from a single electronic state, the resulting KER distribution will be narrow. When various electronic states are involved, the molecules have different excess energies and hence the distribution is broader. This fact becomes clearly visible in figure 7.2. Further details concerning the KER of the individual channels will be discussed later.

4 Steering the proton migration in hydrocarbons

In this chapter, the proton migration process is investigated in small hydrocarbons, namely the isomerization from acetylene (HCCH) to vinylidene (CCH_2) and from allene (H_2CCCH_2) to propyne ($HCCCH_3$). The separation between the fragments from the acetylene and vinylidene breakups, which have similar mass and momenta, is challenging and feasible so far only by coincidence detection methods [17, 63]. Certain dissociation channels, as for example $C_2H_2^{2+} \rightarrow C^+ + CH_2^+$ or $C_3H_4^{2+} \rightarrow C_3H^+ + H_3^+$ can only originate from the isomer and hence these channels are used to investigate the isomerization.

To control the molecular structure of hydrocarbons and thus the chemical and biological properties of the molecules is one of the major driving mechanisms in the research field of light-induced molecular dynamics. And despite many possible applications in chemistry, the control over hydrogen migration has been limited to theoretical studies for a long time [64–66]. Recently, experimental methods have been developed to investigate the hydrogen migration using ultrafast laser pulses. By changing fundamental parameters, e.g. the pulse duration or the intensity, Xie *et al.* explored the isomerization of ethylene [67] and controlled the fragmentation yield of various other hydrocarbons [68]. Other research groups used two-color fields with pulse durations of tens of femtoseconds to control the isomerization in toluene [69] or methanol [70].

Here, the carrier-envelope phase (CEP) is exploited to control the isomerization in acetylene and allene. First, a detailed theoretical explanation provides more insights into the physical fundamentals of the isomerization process (section 4.1). Subsequently, the experimental evidences of the control over deprotonation (section 4.2.2) and isomerization (section 4.2.3) in acetylene and allene (section 4.3) are presented. This chapter is mainly based on [5].

4.1 Theoretical description

The here presented theoretical calculations are based on the work of Robert Siemering [5, 71] and are shown to explain the theoretical background for the isomerization process in acetylene and allene. For a more detailed explanation about the theoretical description,

refer to [71].

In order to describe the CEP-dependence of the hydrogen migration, the two following processes have to be considered. First, the laser-molecule interaction, which occurs within the laser pulse duration of around 5 fs, is described. This process is expressed by normal modes – which can be IR-active or IR-inactive (compare figure 4.1a). An IR-active mode represents hereby the vibrations, at which the dipole moment changes. Secondly, the isomerization process, which happens at much longer time scales of tens of femtoseconds, is simulated. Using symmetry arguments, less degrees of freedom have to be considered when reactive coordinates are used to describe the isomerization. Instead of the normal modes where all atoms are considered, the reactive coordinates investigate the CCH-angles on both sides of the molecule (see figure 4.1a)), which allows to represent the problem in two dimensions even though the simulations are still performed in full dimensions. Hence, for the following representation of the isomerization process only reactive coordinates are used.

In figure 4.1a) and b), the relevant normal modes and the reactive coordinates for acetylene and allene are depicted. In figure 4.1(c) and (d), the potential energy surfaces of the $A^3\Pi$ state (acetylene) and the $B^3\Pi$ state (allene) are depicted. The molecular structure of the acetylene and allene molecule is indicated together with the corresponding isomer configurations, which are found in the global minima (bottom right and top left).

Laser-molecule interaction

Figure 4.1a) depicts the IR-active cis-bending mode $|n0\rangle$ and the IR-inactive trans-bending mode $|0m\rangle$ of acetylene, which form a 2D basis $|nm\rangle$, where m, n are the number of vibrational quanta. In figure 4.1b), the more complex allene molecule and its three normal modes (IR-active rocking and antisymmetric bending and IR-inactive symmetric bending) are shown.

In the following, the laser-molecule interaction is explained exemplarily for acetylene. The excitation and ionization can only occur in the IR-active modes $|n0\rangle$, in which a wave-packet $e^{-i\phi}|n0\rangle$ is created. The phase ϕ of this vibrational wave-packet is thereby given by the CEP of the laser, even if the laser pulse is non-resonant to the vibration. In order to define the ionization time, it is assumed that the molecule is ionized at the intensity maximum, leading to a slight overestimation of the calculated asymmetries, compare figures 4.6b) and 4.8b). Due to the difference of eigenfunctions of the neutral molecule and the cation, the ionization results as well in a population of IR-inactive modes $|0m\rangle$ – being a CEP independent population process. The wave-packet is given by the basic superposition of the fundamental IR-active and the IR-inactive modes:

$$\Psi_{basic} = |01\rangle + e^{-i\phi}|10\rangle\,. \tag{4.1}$$

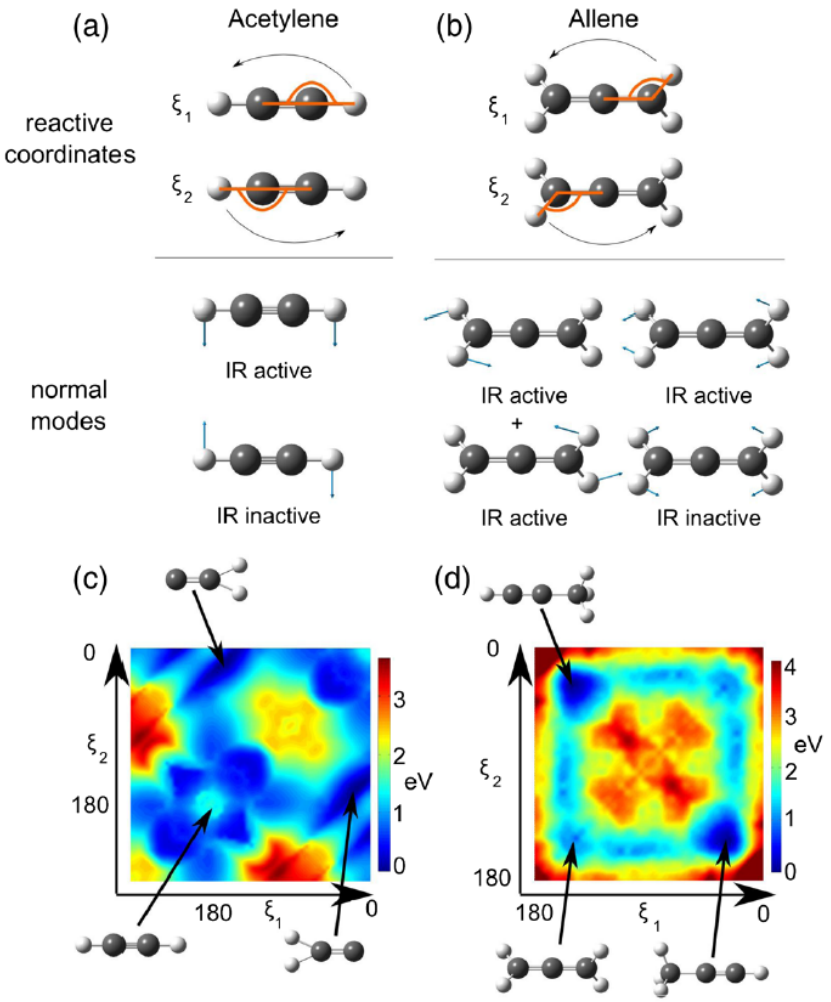

Figure 4.1: Reactive coordinates and normal modes used in the theoretical description of the hydrogen migration in acetylene (a) and allene (b). While the normal modes are used to describe the laser molecule interaction, the reactive coordinates (ξ_1, ξ_2) represent the CCH bond angles (shown in orange) indicating the isomerization process. The reactive coordinate ξ_1 describes the hydrogen migration from the right to the left and ξ_2 from the left to the right. (c) The potential energy surface of the acetylene dication ($A^3\Pi$ state) presents the binding energy as a function of the two reactive coordinates. The two isomerized configurations (top left and bottom right) in the global minima are indicated together with the initial form of the molecule (bottem left). (d) The potential energy surface of the $B^3\Pi$ state of the allene dication. This image was taken from [5].

To interpret the CEP control mechanism, Ψ_{basic} is used as it explains the asymmetric isomerization occurring in the dication. The wave-packet is projected onto the $A^3\Pi$ state, being the lowest dication state supporting isomerization.

Isomerization process

To simulate the isomerization step, the wave-packet Ψ_{basic} is propagated along the two dimensional PES along the two reactive coordinates (see figure 4.1). For this purpose, the wave-packet Ψ_{modes}, expressed in normal modes, is projected onto the wave-packet ψ_{reac}, expressed in reactive coordinates. The respective eigenfunctions of the dication ground state are used to perform this projection:

$$\psi_{reac} = \sum_{i,j} \langle \Psi_{modes} | \Phi_i \rangle \langle \Phi_i | \phi_j \rangle | \phi_j \rangle , \tag{4.2}$$

where Φ_i are the normal mode eigenfunctions, and ϕ_j are the reactive coordinate eigenfunctions. The evolution of the wave-packet is calculated for 480 fs in steps of 0.24 fs along the PES of the $A^3\Pi$ state (acetylene, figure 4.1(c)) and the $B_3\Pi$ state (allene, figure 4.1(d)). It is visible that for both molecules the Franck-Condon region – the region of the PES where the wave-packet is projected onto from the ground state – is not the global minimum. A wave-packet starting from the Franck-Condon region experiences first local minima where-after the molecule can undergo isomerization to reach the global minimum. The corresponding molecular configurations are indicated in each plot (compare 4.1(c) and (d)).

The propagation of the wave-packet for two different CEP is illustrated in figure 4.2 for the isomerization of acetylene to vinylidene. The basic wave-packet Ψ_{basic} for a CEP of π and zero are visualized within the first two subplots. It can be seen that both wave-packets evolve differently along the PES resulting in a population of either potential minima, which correspond to left or right configuration of vinylidene. In other words, the initial wave-packet triggers a preferential isomerization direction. This difference in the final distribution is experimentally observable as an asymmetry in the C^+ emission direction, which is tunable by the CEP.

The left (right) isomerization is quantified from the dissociation yield $L(R)$ within both global minima, which correspond to the left and right configuration of vinylidene, integrated over the complete propagation time. The resulting asymmetry parameter A is calculated from L and R according to equation 4.3 and is shown in figure 4.6b). Even though the asymmetry is slightly overestimated, a good agreement between theory and experiment can be achieved.

The isomerization of allene can be calculated in a similar manner to acetylene being

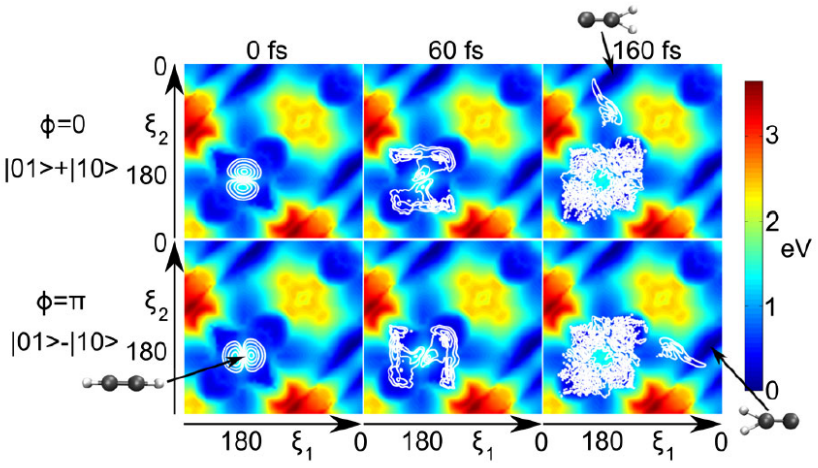

Figure 4.2: Wavepacket evolution on the $A^3\Pi$ state of acetylene for two different initial wave-packets schematically depicted along the reactive coordinates ξ_1 and ξ_2. The two wave-packets correspond to a CEP of 0 (top row) and π (bottom row). The white contour lines depict the nuclear wave-packet at different times after ionization and thereby visualize the amount of isomerized molecules in the final state. While a CEP of 0 results in a isomerization from left to right (top row), a CEP of π leads to a hydrogen migration from right to left (bottom row). This image was taken from [5].

however more complex. For example, the reactive coordinates to describe the isomerization are a linear combination of eight normal modes. Within the preparation step, three of these modes (one IR-inactive, two IR-active ones; see figure 4.1b)) are used to prepare the initial CEP-dependent wave-packet: $\Psi = |00m\rangle + e^{-i\phi}(|n_1 00\rangle + |0n_2 0\rangle)$.

As seen in figure 4.8, the left-right asymmetry of the allene isomerization to propyne can not only qualitatively be reproduced but as well also quantitatively. The successful extension of the theoretical model from acetylene to allene indicates that also the nuclear dynamic in even larger molecules can be simulated as long as the proper reaction coordinates can be identified.

4.2 Acetylene

Using the coincidence technique allows us to separate different break up channels, see figure 4.3. While in section 3.4, the filtering of the deprotonation channel was shown, here the more challenging isomerization channel is investigated.

In figure 4.3a), the PIPICO spectrum of acetylene is depicted in the region of interest for the isomerization channel. Clearly observable are the two coincidence channels, which are in close proximity to each other due to their similar masses. The horizontal and ver-

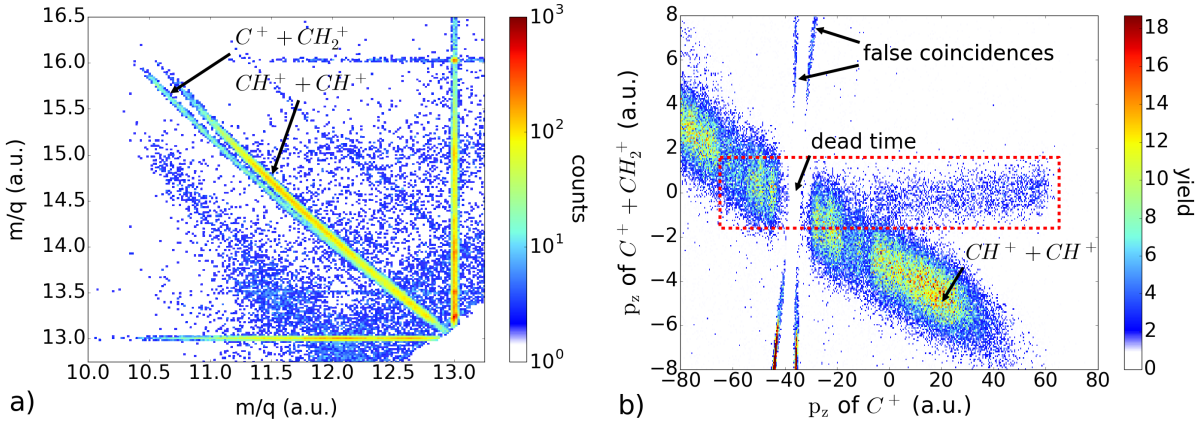

Figure 4.3: a) Photoion-photoion coincidence spectrum of acetylene measurement: graphical representation of the time of flight (TOF) of the first ion against the TOF of the second ion. The TOF's are already converted into the m/q ratio to facilitate the identification. b) Graphical representation of the coincidence filtering. Only events within the red dashed box are considered for further analysis of the isomerization channel. More details can be found in the text.

tical lines correspond to "false" coincidences. In figure 4.3b), a graphical representation of the coincidence filtering is shown. When the momentum conservation is fulfilled, the momentum sum of the coincidence channel $C_2H_2^{2+} \rightarrow C^+ + CH_2^+$ should be independent on the momentum of the C^+ ion (compare to figure 3.11b). All counts within the red dashed box fulfill this condition and thus they are used for further analysis. The other events correspond to the symmetric breakup channel ($C_2H_2^{2+} \rightarrow CH^+ + CH^+$, diagonal contributions) or "false" coincidences ($C_2H_2^{2+}$ with C^+ or CH^+, almost vertical contributions). Furthermore, around -40 a.u. the "dead" time of the detector – the time after a first particle detection, when the detector is insensitive to a second ion impact – is clearly visible (see section 3.4). Utilizing this technique, not only in the shown p_z direction but in all three dimensions, improves the separation between the isomerization channel and all other contributions even further.

After applying the coincidence filtering to all coincidences channels, we now investigate the experimental result concerning the CEP-dependence of the various processes. The shown data for acetylene were recorded at a laser intensity of $1.3 \cdot 10^{14}$ W cm^{-2}.

4.2.1 Double ionization of acetylene

In order to have a benchmark of the CEP-control in polyatomic molecules, first the CEP-control over the electron emission direction in acetylene is investigated by analyzing the

double ionization of acetylene. Usually, the electron motion can be easily controlled by the carrier-envelope phase, which is reflected by high asymmetry parameters [72]. In figure 4.4,

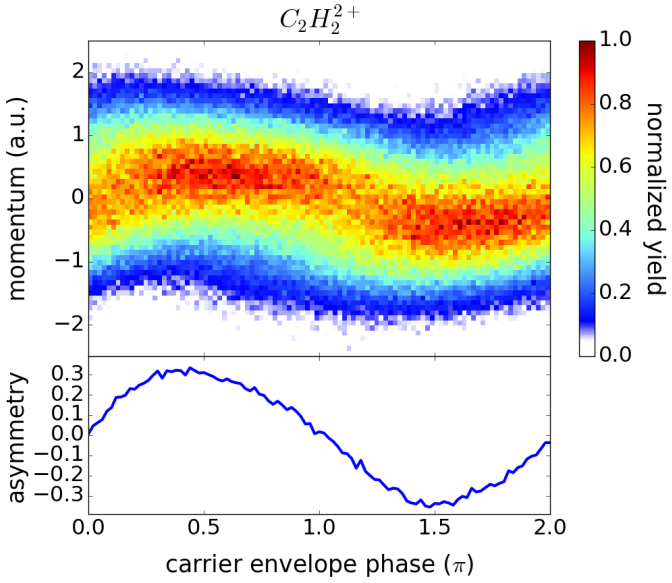

Figure 4.4: Momentum resolved ionization yield as a function of the carrier-envelope phase in the double ionization of acetylene. Here, only the momentum along the laser polarization is considered.

the double ionization yield is depicted as a function of the momentum and carrier-envelope phase. Here, and throughout this thesis, the term "momentum" represents the momentum along the laser polarization, neglecting the transverse momenta. It can be observed, that the CEP induces a clear shift of the momentum distribution. The yields of $C_2H_2^{2+}$ ions emitted to the right R(ϕ) or left L(ϕ) as a function of the CEP can serve as a measure of the influence of the CEP. To quantify the CEP dependence, the asymmetry parameter $A(\phi)$ is introduced with:

$$A(\phi) = [L(\phi) - R(\phi)]/[L(\phi) + R(\phi)]. \tag{4.3}$$

In this measurement, an asymmetry of 34 % was reached, which is visible in the lower part of figure 4.4. Thus, we can conclude that this measurement provided an excellent CEP-control over the electronic motion in acetylene. In the following, the CEP-control of the same measurement over the deprotonation and isomerization channel will be shown.

4.2.2 Deprotonation of acetylene

The deprotonation of acetylene is a well-studied process [6, 73] and is shortly explained here for the sake of completeness. It is particularly interesting that a CEP-control was observed at all [6], as acetylene is a linear and symmetric molecule without a dipole moment. Usually, molecules without a dipole moment cannot be controlled by the CEP and hence a new explanation had to be found. The possibility of a CEP control was explained by a superposition of vibrational modes within the dication state where the CEP acts as a trigger controlling the vibrational excitation. For further information on the theoretical model and interpretation refer to [6]. In figure 4.5, the CEP-control over deprotonation is visualized in two different manners. First, figure 4.5 a) depicts the momentum sum of both fragments as a function of the CEP. Note that the momentum sum p_i usually differs slightly from zero as it equals the negative momentum sum of all emitted electrons. Hence, by investigating p_i, similar information on the ionization process compared to the double ionization signal should be extractable. And indeed, the retrieved asymmetry of 32 % was observed here as well (compare figure 4.4). Secondly, in figure 4.5b) and c), the individual momenta of the coincident fragments are shown in dependence of the CEP. In comparison to the momentum sum, several observation can be made:

- The observed momenta are increased to more than 20 atomic units, which is a direct result of the Coulomb explosion (CE).
- The momentum distribution does not reveal a clear CEP-dependence due to its large spread. Hence, only the one-dimensional representation clearly indicates the control over deprotonation direction.
- Even though the asymmetry parameter reaches only 3 % a clear CEP- dependence can be observed. Comparing the asymmetry amplitude of the electrons, which are 1800 times lighter, it is surprising that an asymmetry can be detected at all. This control over the deprotonation was explained by a superposition of vibrational motion triggered by the electronic excitation, compare section 4.1 and reference [6].

As the shown two dimensional representation of coincident fragments, see figure 4.5b) and c), only provide limited additional information, following CEP-control measurements will exclusively be shown in the one dimensional representation.

4.2.3 Isomerization of acetylene

After the observation of the CEP-control over deprotonation, a more complex molecular reaction, the isomerization, is discussed in the following. During the isomerization, the molecular structure of acetylene changes from its linear configuration to the vinylidene

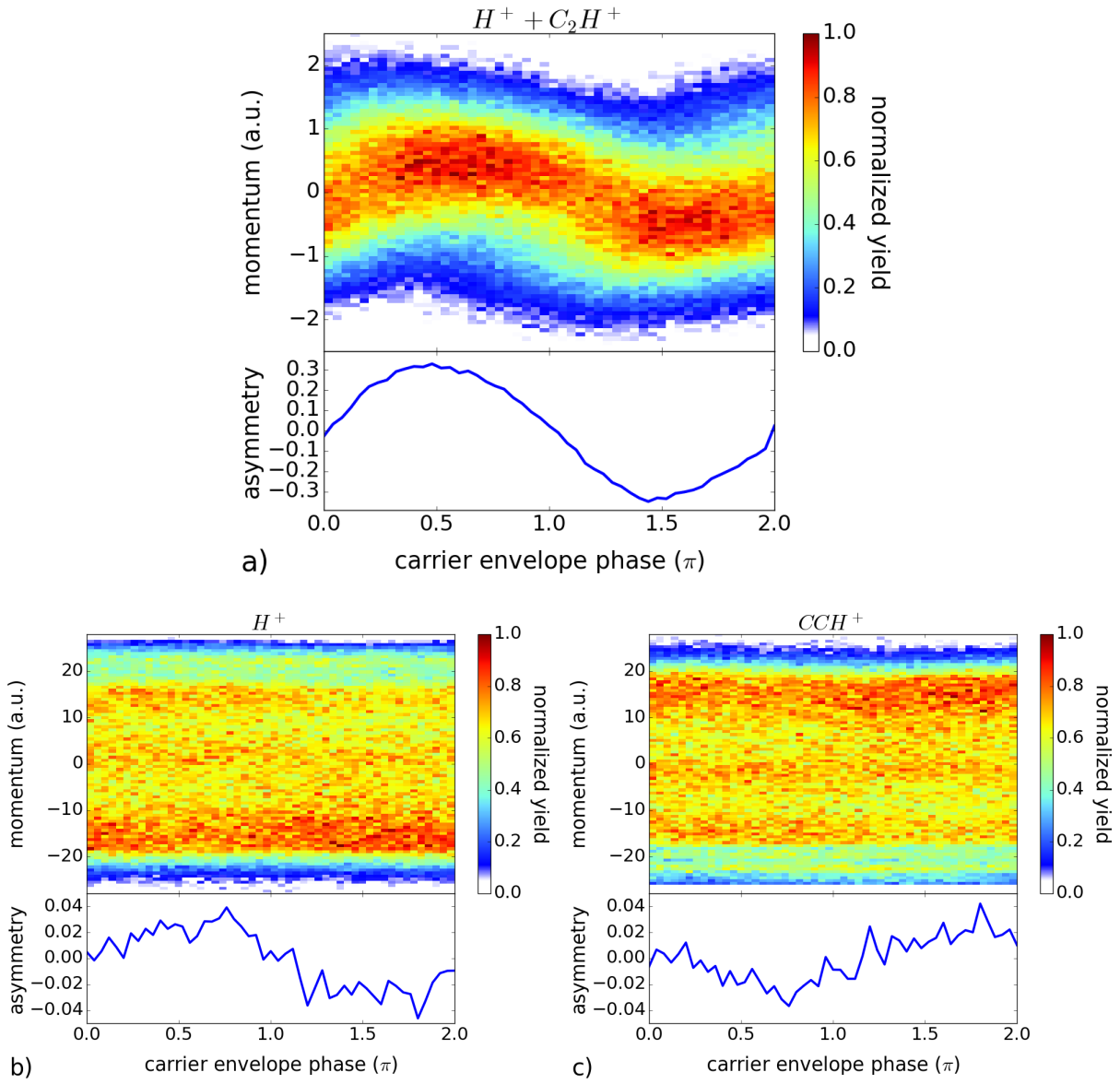

Figure 4.5: Momentum maps for the coincidences of the deprotonation channel of acetylene in dependence of the carrier-envelope phase. The momentum sum of both particles is shown in a) while in b) the hydrogen momentum and in c) the CCH^+ momentum of those coincidences is presented.

isomer by hydrogen migration. If the molecule is Coulomb exploding from the vinylidene configuration, the resulting fragments (C^+ and CH_2^+) can be distinguished from the symmetric breakup of acetylene by the coincidence techniques as discussed above. The momentum of carbon ions from these coincidences is depicted in figure 4.6a). The momentum along the laser polarization (p_z) is shown versus the momentum along the laser propagation direction (p_x). The mostly isotropic distribution of the carbon ion is a consequence of the hydrogen migration which triggers a rotation of the molecule and hence the carbon is emitted in all directions. In the momentum range 42 a.u.$< p_z <$ 28 a.u. the above mentioned overlap in TOFs of both coincidence channels impedes a definite coincidence detection. Thus, only events outside of this range were evaluated to investigate the CEP dependence of the carbon emission direction. In figure 4.6b), the asymmetry

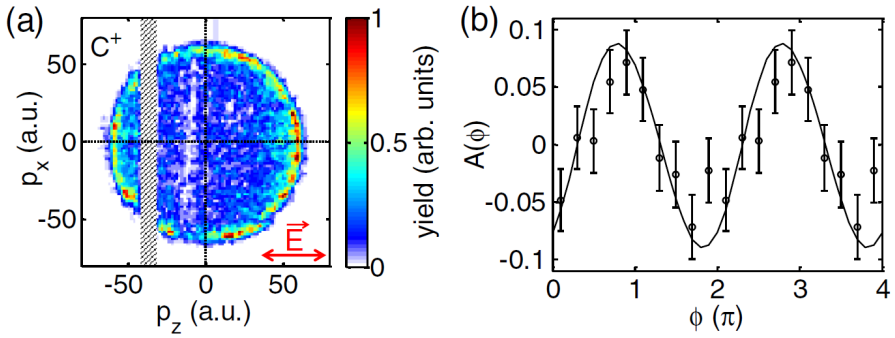

Figure 4.6: a) CEP-averaged momentum distribution of C^+ ions resulting from the dissociation of vinylidene. b) Asymmetry parameter of C^+ ion emission direction in dependence of the carrier-envelope phase. The solid line depicts the calculated asymmetry for an intensity of $1.5 \cdot 10^{14}$ W cm^{-2} which is shifted along the CEP axis for best agreement. This image was taken from [5].

of carbon ion emission in dependence of the carrier-envelope phase is depicted. A clear CEP-dependence is observed revealing a surprisingly large amplitude of 8 %. The solid line depicts th simulated asymmetry in dependence of the CEP. As in the experiment the absolute CEP cannot be determined, the predicted asymmetry curve of the C^+ ion was shifted for best agreement. The CEP axes in figure 4.6b) is given relative to the phase offset of the asymmetry parameter of the single ionization.

By comparing experimental data and theoretical predictions, it becomes obvious that the isomerization process of a linear molecule can be explained by a superposition of vibrational modes, which trigger a subsequent hydrogen migration. The asymmetry amplitude is even larger for the isomerization than compared to the deprotonation. One possible explanation is that for an isomerization only very distinct states can contribute to the process, while for the deprotonation a multitude of states will dissociate into the detected $H^+ + CCH^+$

channel and thereby wash out the signal.

4.3 Isomerization of allene

In order to investigate if the isomerization process can be controlled also in larger hydrocarbon molecules, in the following allene ($H_2C_3H_2$) is studied onto its possible CEP-control over hydrogen migration. In comparison to acetylene, allene has not four but seven atoms and hence the doubly charged molecule can Coulomb explode in many different dissociation channels. In figure 4.7, this variety of dissociation channels can be seen within the

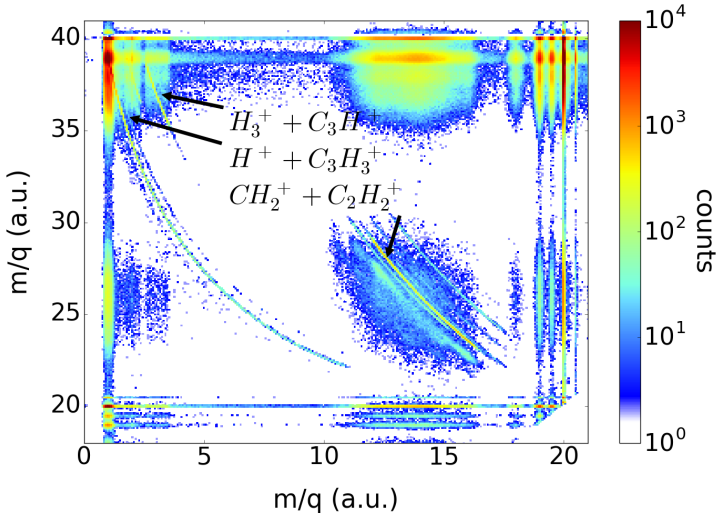

Figure 4.7: Photoion-photoion coincidence spectrum of acetylene measurement: graphical representation of the time of flight of the first ion against the TOF of the second ion. The TOFs are already converted to mass over charge (m/q) ratio. While a variety of dissociation channels are observable, only the major coincidence channels are highlighted by arrows.

PIPICO representation of allene. While the major coincidence lines are highlighted, also additional channels are observed. These can be used to extract supplementary information about the processes occurring in an ionized allene molecule. The horizontal and vertical lines occur due to "false" coincidences between various charged fragments, e. g. $C_3H_4^+$ (m/q=40), $C_3H_4^{2+}$ (m/q=20), and $C_2H_2^+$ (m/q=26). All subsequent data were recorded at an laser intensity of $3 \cdot 10^{14}\,\mathrm{W\ cm^{-2}}$.

The hydrogen migration in allene is discussed in the following within the dissociation channel $C_3H_4^{2+} \rightarrow H_3^+ + C_3H^+$. Thereby, isomerization is monitored through the formation of trihydrogen ions (H_3^+). Even though allene's isomer propyne (HC_3H_3) is stable in the

neutral state and contained in low concentrations in commercially available allene gas bottles, H_3^+ formation has been found to result predominantly from the isomerization of allene [13].

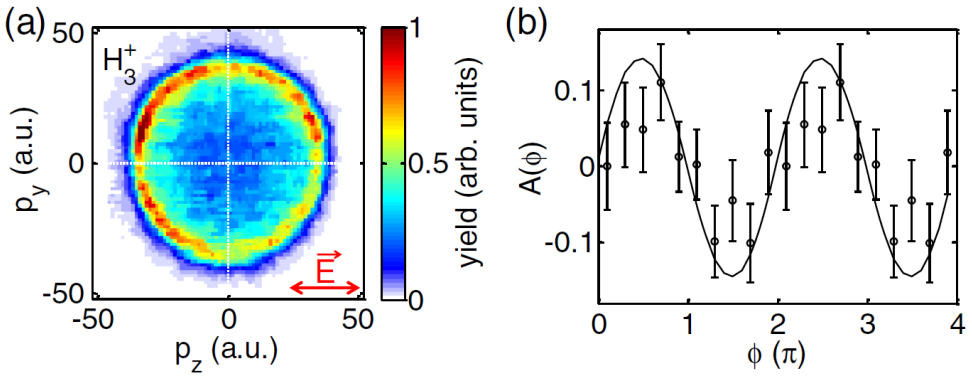

Figure 4.8: a) CEP-averaged momentum distribution of H_3^+ ions resulting from the dissociation of propyne. The red arrow indicates the laser polarization direction. b) Asymmetry parameter of H_3^+ ion emission direction in dependence of the carrier-envelope phase. The solid line depicts the calculated asymmetry for an intensity of $3.0 \cdot 10^{14}\,\mathrm{W\,cm^{-2}}$, which is shifted along the CEP axis similar by the same amount as for the isomerization in acetylene. This image was taken from [5].

Figure 4.8a) displays the CEP averaged H_3^+ momentum distribution, which was found to be isotropic. Similar to the isomerization in acetylene, this uniform distribution results from the molecular rotation and is consistent with the previous studies on the isomerization of allene [12, 13]. In figure 4.8b), the asymmetry parameter $A_{H_3^+}(\phi)$ is shown in dependence of the carrier-envelop phase. Clearly observable is the CEP-dependence of the asymmetry parameter revealing the control over the directionality of proton migration in allene (above 5 %). Thus, it can be concluded that similar to the acetylene measurement, in allene the hydrogen migration can be controlled by the carrier-envelop phase. In order to compare the experimental CEP information and the theoretical simulations, the following procedure was applied. Similar to figure 4.6b) the asymmetry parameter of the experiment in figure 4.8b) is given relative to the phase offset measured for the single ionization. For the predicted H_3^+ ion asymmetry curve the CEP was shifted by the same amount as the predicted C^+ curve. It can clearly be seen, that the experimental data and the theoretical predictions overlap well. This indicates that the simulation was successfully applied also for slightly larger molecules. Again, a strong CEP-control over the isomerization direction was observed, indicating the strong influence of the electronic wave-packet motion onto vibrational nuclear motion and its subsequent isomerization.
Having established the experimental and theoretical evidence of a CEP-control over hy-

drogen migration in small hydrocarbons allows now to extend the studies to even larger molecules.

4.4 Conclusion

In this chapter, the CEP-control over molecular reactions in hydrocarbons is discussed in detail. Experimental measurements were performed in acetylene and allene, where a CEP-control over the deprotonation and isomerization could be shown. The achievable control over the isomerization of 8-10 % was two times higher than the control over the deprotonation. One possible explanation is a higher sensitivity of the isomerization process, compared to the deprotonation, on the electronic wave-packet, which is created by the laser-molecule interaction. The experimental findings are supported by the theoretical model, which simulates the creation and propagation of a nuclear wave-packet. Within the simulations, the CEP-controlled isomerization process is described by two subsequent steps. First, a field-sensitive nuclear wave-packet is created during the laser-molecule interaction. In the second step, this CEP-dependent wave-packet is freely propagated along the potential energy surface. Thereby, the CEP-dependence of the starting wave-packet are sufficient to predetermine the final wave-packet position. In other words, the CEP predefines the trend of the isomerization, which occurs on much longer timescales and hence allows to steer the directionality of isomerization.

Having established this control mechanism for isomerization, it is now possible to also investigate more complex photochemical reactions, e.g. a keto-enol tautomerization or changing the chirality of molecules. Furthermore, to increase the control over isomerization, one could resonantly excite vibrational modes, which directly couple to the nuclear motion and thus provide higher control. Such experiments, however, can only be performed using excitation wavelengths in the mid-IR region.

However, before studying more complex systems, it is important to investigate the intensity dependence of the control mechanisms to understand if the mechanism is generally applicable or only for specific intensities. Thus, in the following chapter, the CEP-control in acetylene and allene is investigated for a broad intensity range.

5 Intensity-dependent control over isomerization

An ultrashort laser pulse can excite and double ionize an atom or a molecule via various processes, e.g. NSDI or sequential double ionization (SDI), depending on the applied intensity [74–76]. As seen in the last chapter, the ionization step can predetermine the subsequent processes, e.g. hydrogen migration in hydrocarbons. Thus, a change in applied intensity might not only alter the ionization process but can alter the subsequent isomerization step as well. In this chapter, the CEP-dependence of the dissociative ionization in acetylene and allene are investigated for a broad intensity range regarding the deprotonation:

$$C_2H_2^{2+} \rightarrow H^+ + C_2H^+,$$
$$C_3H_4^{2+} \rightarrow H^+ + C_3H_3^+,$$

and the isomerization

$$C_2H_2^{2+} \rightarrow C^+ + CH_2^+,$$
$$C_3H_4^{2+} \rightarrow H_3^+ + C_3H^+.$$

First, the experimental and theoretical methods are explained (section 5.1). Subsequently, the results on acetylene (section 5.2) and allene (section 5.3) are discussed. This chapter is mainly based on: M. Kübel, C. Burger, *et al.* [4]

5.1 Methods

To directly compare the experimental results shown here to the previous chapter, the laser setup and its operation parameters were kept identical. To measure the CEP of the ultrashort pulses, a stereo-ATI phasemeter [50] was used for the acetylene experiments, whereas an f-2f interferometer [45] was utilized for the allene experiments. The change of the CEP was performed as before by varying the dispersion within the stretcher unit of the amplifier. Before entering the reaction microscope, the laser pulses are attenuated by a motorized neutral density filter wheel. With this, the intensity within the interaction

region can be varied by four orders of magnitude, here, however, only a factor of three is used, without changing the beam focus size, as done by using an iris. In order to allow for optimized coincidence detection, the average count rate was kept below 8 kHz (see section 3.4.1). Furthermore, to acquire reasonable statistics, the count rate should neither be too low. Due to the highly non-linear intensity dependence of strong-field ionization, it is difficult to fulfill both criteria while changing the laser intensity.

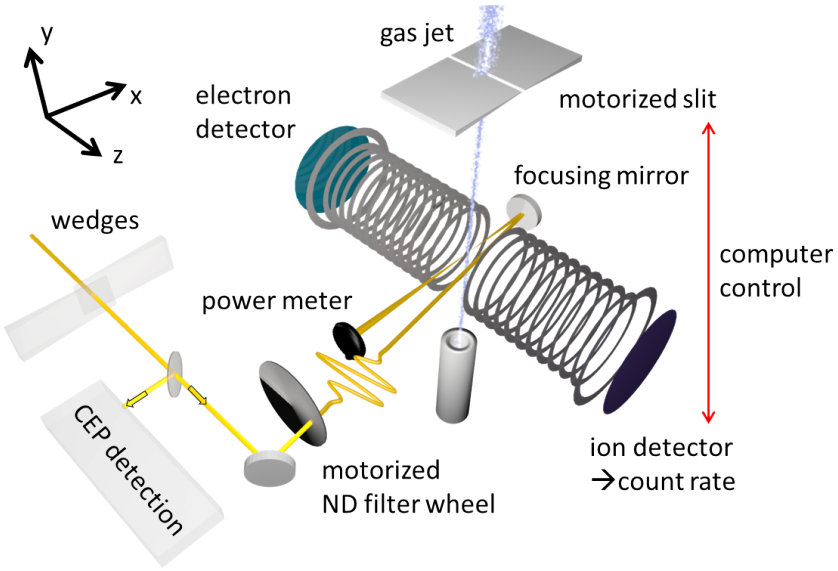

Figure 5.1: Experimental setup for the simultaneous intensity and carrier-envelope phase measurement of hydrocarbons. The CEP for each of the laser pulses is continuously swept, measured, and recorded. Additionally, the pulse energy is modified by a motorized neutral density (ND) filter wheel and recorded by a power meter. To account for changes in the count rate due to the intensity scan, a motorized slit allows to adjust the density of the gas jet.

Figure 5.1 depicts the experimental setup for the simultaneous intensity- and CEP-scan. First, the CEP was measured, actively controlled, and analyzed as mentioned in chapter 4. Secondly, the intensity scan was performed as follows:

- The neutral density filter wheel is continuously changing the pulse energies, leading to an intensity variation between $\sim 1 \cdot 10^{14}\,\mathrm{W/cm^2}$ and $\sim 3 \cdot 10^{14}\,\mathrm{W/cm^2}$. The pulse energies are recorded by a fast electronic power meter behind the exit window of the REMI. As the focal spot and the pulse duration remain unaffected by the filter settings, the laser intensity is directly proportional to the pulse energy. To determine the proportionality factor between the pulse energy and laser intensity, separate measurements on Ar and Ne targets were performed [75].

- The count rate of the ion detector is monitored on the data acquisition computer, which generates a feedback signal for the motorized slit within the gas jet.
- The width of the slit was changed to modify the total amount of gas molecules in the focal area, and hence the count rate.

All in all, this setup allows to tune a variety of parameters, i.e. dispersion settings, filter wheel position, count rate, and slit width and analysing the corresponding CEP values as well as the power/intensity information.

In order to compare the experimental results to the theoretical predictions, it is important to consider the constant but unknown CEP offset of the CEP detection in the f-2f interferometer and the phasemeter. Thus, the experimental CEP offset is fixed by the following procedure:
Using acetylene, the experimental CEP values are shifted to obtain best agreement with the theoretical predictions in the deprotonation channel at an intensity of $1.5 \cdot 10^{14}\,\mathrm{W/cm^2}$ (see figure 5.3).
Using allene, the CEP axis is shifted such that the single ionization of allene has a similar CEP-dependence as the one of acetylene at an applied intensity of $1.0 \cdot 10^{14}\,\mathrm{W/cm^2}$.

The principles of the theoretical calculations are identical to chapter 4. First, IR-active vibrational modes are CEP-dependently excited and populated by the laser field, and thus the resulting wave-packet depends on the CEP of the laser field. Secondly, the wave-packet is freely propagated on the potential energy surface with a preferential direction predetermined by the CEP. This preferred directionality translates into a CEP-dependent deprotonation or isomerization of the molecule.

5.2 Acetylene

5.2.1 Double-ionization of acetylene

In the previous chapter, it was shown that the ionization process predetermines subsequent molecular reactions such as deprotonation and isomerization. Therefore, in this first section, the double-ionization of acetylene is investigated as a function of carrier-envelope phase and laser intensity.

Figure 5.2 depicts the asymmetry of the double-ionization of acetylene as a function of intensity and CEP in two different ways: a) pure double-ionization and b) center-of-mass of the deprotonation channel. In both channels, the usual 2π CEP-dependence is observed [77]. With increased intensity, the asymmetry amplitude decreases from 35 % to below 20 %. The offset of the CEP dependent asymmetry, also known as “phase of the phase” [78], reveals only a small intensity dependence – the maxima and minima are aligned almost vertically.

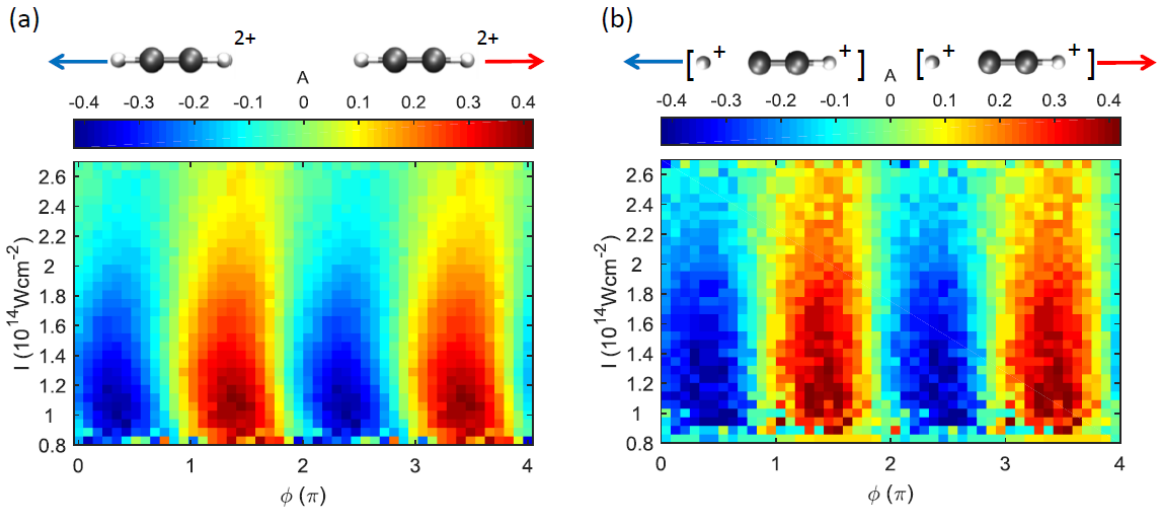

Figure 5.2: Asymmetry of a) the double-ionization in acetylene ($C_2H_2^{2+}$) and b) the center-of-mass of the deprotonation channel ($H^+ + C_2H^+$) as a function of the intensity and the carrier-envelope phase ϕ. The ionization channels are depicted by the molecular sketches above the plots. This image was taken from [75].

In figure 5.2a), the shape of the intensity- and CEP-dependence of the double-ionization of acetylene corresponds well to previously reported results on the double-ionization of argon [75]. For both gases, the asymmetry parameter is strongest for small intensities. To explain this phenomenon, it is important to recall that two different ionization processes can occur. The first is the so-called sequential double-ionization (SDI), which is based on tunnel ionization. This process requires high electric fields and leads to the ejection of two subsequent electrons. As both electrons are independently ionized and their ionization probabilities are only sensitive to the field strength, this process can only slightly be controlled by the CEP. The second double-ionization process is the non-sequential double-ionization (NSDI) induced by electron recollision. Thereby, the first electron is ionized by tunnel ionization through the potential barrier but subsequently it recollides with the remaining ionic core and releases the second electron. As the recollision requires specific electron trajectories, the NSDI process is highly dependent on the CEP. Thus, the strong CEP-dependence for small intensities can be seen as a direct result of NSDI induced by electron recollision. By increasing intensity, SDI becomes more probable and hence the CEP-dependence is reduced. In conclusion, within the here-shown intensity range, NSDI represents the dominant double-ionization mechanism.

In figure 5.2b), the center-of-mass motion of the deprotonation channel is depicted. In analogy to the pure double-ionization, compare figure 5.2a), it can be concluded that also the deprotonation is induced by electron recollision. This implies that both final states,

i.e. $C_2H_2^{2+}$ and $H^+ + C_2H^+$, are triggered by the same process and that the populated dication states can either stay bound or dissociate. Slightly smaller asymmetry values were observed within the non-dissociative channel in comparison to the deprotonation channel. To explain these reduced asymmetry values, the electronic states involved in the dissociation process have to be analyzed. While the molecule is still bound in the dication ground state, the deprotonation occurs only in excited dication states, and hence needs more excitation energy [79]. Thus, the transition from NSDI to SDI takes place at higher intensities, which translates for the investigated intensity range into higher asymmetry parameters.

5.2.2 Deprotonation of acetylene

In contrast to the figures shown above, only the momentum of a single fragment is depicted in the following, i.e. the proton momentum for the deprotonation channel and the carbon momentum for the isomerization channel.

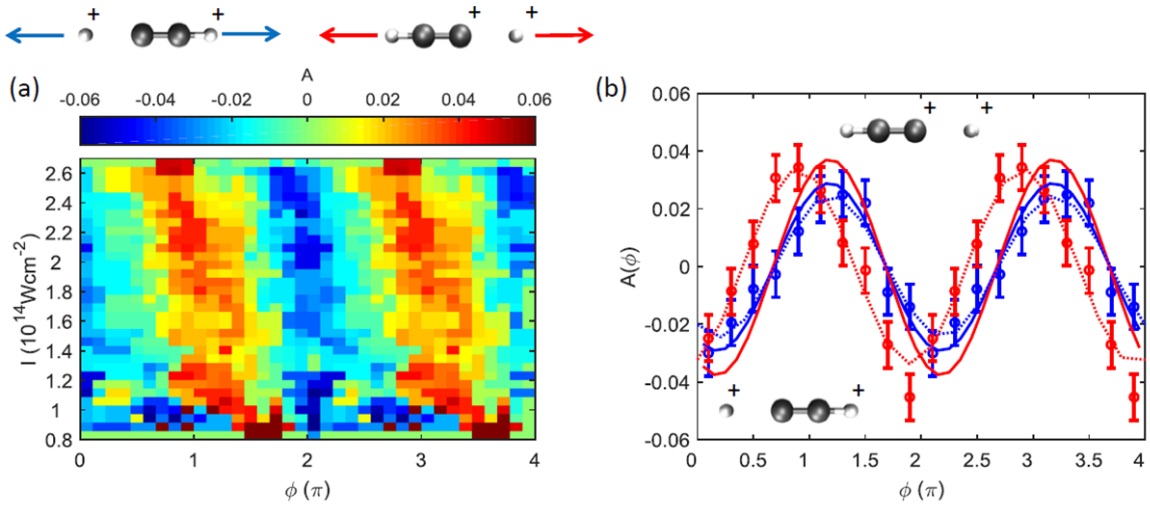

Figure 5.3: a) Asymmetry of the proton momentum as a function of CEP and laser intensity in the deprotonation channel. b) Comparison of the experimental data (symbols) and the theoretical prediction (solid lines) for two different intensities ($1.5 \cdot 10^{14}\,\mathrm{W/cm^2}$ (blue) and $2.5 \cdot 10^{14}\,\mathrm{W/cm^2}$ (red). The experimental data are averaged over the range of $\pm 0.2 \cdot 10^{14}\,\mathrm{W/cm^2}$ and fitted by a sinusoidal fit (dotted lines). Due to the unknown experimental CEP offset, the experimental data were shifted for best agreement with the theory at an intensity of $1.5 \cdot 10^{14}\,\mathrm{W/cm^2}$. This image was taken from [75].

In figure 5.3a), the asymmetry of the proton momentum resulting from the deprotonation process is depicted as a function of the laser-intensity and the CEP. In figure 5.3b),

two line profiles for the intensities $1.5 \cdot 10^{14}\,\mathrm{W/cm^2}$ (blue) and $2.5 \cdot 10^{14}\,\mathrm{W/cm^2}$ (red) and their sinusoidal fits (dotted lines in the corresponding color) are directly compared to the theoretical predictions (solid lines). Several observations can be made: First, the asymmetry remains below 5 % throughout the investigated intensity range. A slight increase of the asymmetry amplitude with intensity can be identified but, as visible in figure 5.3b), this increase is not significant with respect to the error bars. Secondly, the asymmetry phase offset changes to smaller values for higher intensities, which can be seen in the line profiles in figure 5.3b). Thirdly, the experimental data and their theoretical predictions agree well regarding the retrieved amplitudes. The measured phase shift of $50 \pm 13°$, however, cannot be reproduced by the theoretical model. Likely, the changing ionization process for higher intensities results in an altered CEP-dependence, which influences the phase offset. This change within the ionization process is not considered in the simulation. In the latter, the ionization is assumed to be constant at the maximum of the electric field, which usually results in an overestimation of the asymmetry values (compare chapter 4). Here, however, the asymmetry amplitudes agree well, representing a surprisingly strong asymmetry in the experiment, which might originate from contributions of higher excited states as described in the following.

Contributions from different electronic states

The investigation of kinetic energy release (KER) of the Coulomb explosion will allow gaining more insight into the involved electronic states. In figure 5.4a), the KER distribution of the deprotonation channel is depicted for three different intensities. For all intensities, "false" coincidences were observed in the region of low KERs (below 1 eV). For the three laser intensities chosen, a broad energy distribution from 2.5-8 eV was measured. This indicates that the molecules have different amount of excess energy, and thus originate from different excitation states. Furthermore, a shoulder at around 5 eV becomes apparent, which allows us to separate the energy distribution into a low (blue shaded) and a high (red shaded) KER region. This enhanced contribution at higher KERs indicates that the corresponding parent molecules were excited into energetically higher lying states. Thus, it is possible to separate the dication states by the final KER. In figure 5.4b), the asymmetry parameter for the low and high KER counts is depicted together with the theoretical prediction. It becomes obvious, that the separation of the KER influences the amplitude of the asymmetry. The low energetic coincidences (blue) reveal a rather small asymmetry amplitude compared to the theoretical prediction. This is in agreement with the aforementioned theoretical overestimation of the asymmetry due to the assumption that the molecule is always ionized at the maximum of the laser field. The high energetic coincidences (red) reveal an increase in amplitude, which indicates that the higher excited states are likely populated by electron recollision and hence are more sensitive on the electric

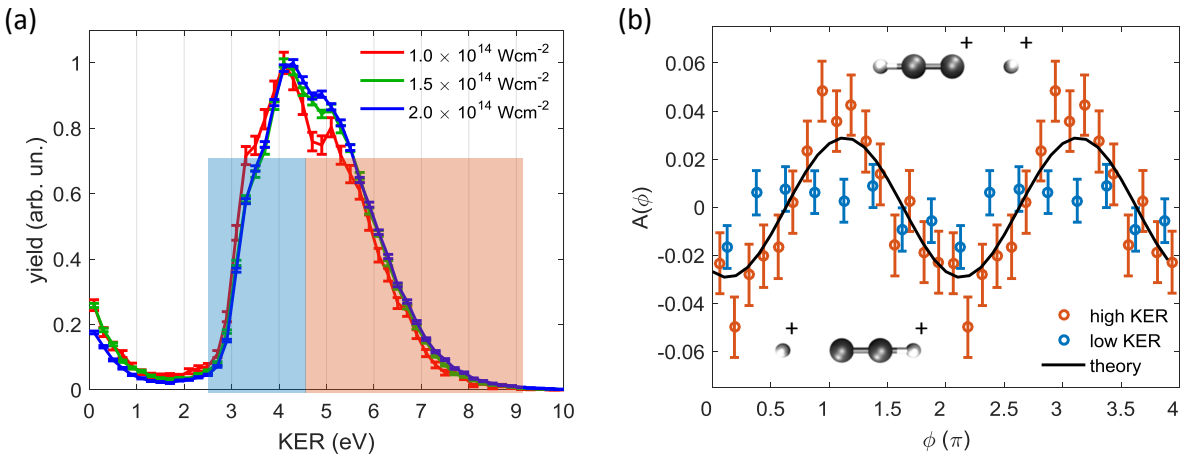

Figure 5.4: a) Kinetic energy release (KER) distribution of the deprotonation channel, for three different intensities, each integrated over $\pm 0.2 \cdot 10^{14}\,\mathrm{W/cm^2}$. The separation into blue and red shaded areas depicts the low- and high-KER regions, respectively. b) Asymmetries of the proton momenta at an intensity $I = 1.5 \cdot 10^{14}\,\mathrm{W/cm^2}$ for the low (blue) and high KER (red) region. The theoretically predicted asymmetry assuming the deprotonation reaction occurs within the $A^3\Pi$ state. This image was taken from [75].

field shape.

5.2.3 Isomerization of acetylene

In the following, the isomerization and its subsequent dissociation via the $C_2H_2^{2+} \rightarrow C^+ + CH_2^+$ channel is investigated in detail. As seen in the previous section, the KER distribution provides valuable information on higher lying excited states. For the isomerization of acetylene, the KER distribution is relatively narrow compared to the deprotonation channel, see figure 5.5. This narrow contribution around 4.4 eV is in good agreement with previous measurements using strong IR laser pulses [11, 63]. It indicates that only few different states are involved in the isomerization reaction. Here, the $A^3\Pi$ state is the only relevant state in the dication, which allows for isomerization. Thus, the resulting energies of a Coulomb explosion are well defined, leading to a narrow KER distribution shown in figure 5.5 for three different intensity values.

In figure 5.6a), the CEP-dependent asymmetry of the carbon momenta is displayed for two intensity values. As in the deprotonation, the asymmetry amplitude is less than $\pm 10\,\%$, which is in agreement with the CEP-control over the isomerization presented in figure 5.6. For higher intensities, i.e. above $1.4 \cdot 10^{14}\,\mathrm{W/cm^2}$ the asymmetry amplitude decreases significantly while changing the offset phase by $70 \pm 20°$ with respect to lower intensities.

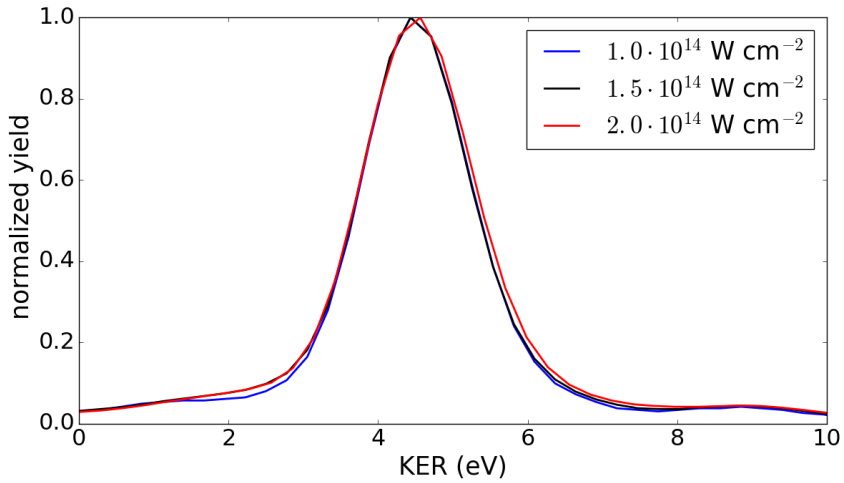

Figure 5.5: Kinetic energy release (KER) distribution of the deprotonation channel, for three different intensities, each integrated over $\pm 0.2 \cdot 10^{14}\,\mathrm{W/cm^2}$.

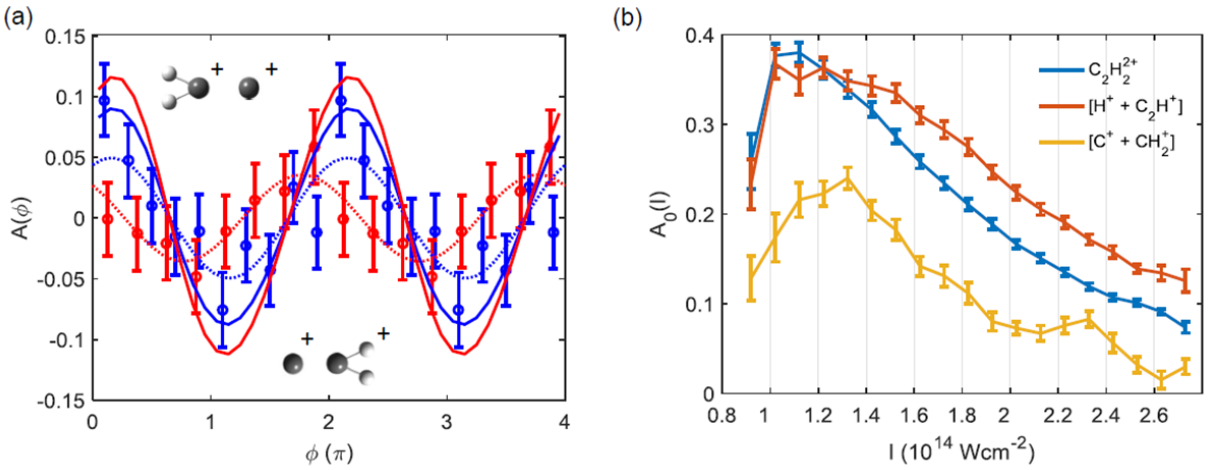

Figure 5.6: a) Asymmetry of the CEP-dependent emission direction of the carbon momenta resulting from isomerization channel $C_2H_2^{2+} \rightarrow C^+ + CH_2^+$. Depicted are two different intensities, $1.5 \cdot 10^{14}\,\mathrm{W/cm^2}$ (blue) and $2.5 \cdot 10^{14}\,\mathrm{W/cm^2}$ (red), which are averaged over a range of $\pm 0.3 \cdot 10^{14}\,\mathrm{W/cm^2}$. While the solid lines represent the theoretical calculations the dotted lines are sinusoidal fits to the experimental data (symbols). The hydrogen migration direction is depicted by the schematic drawings above and below the asymmetry curves. b) Intensity-dependent asymmetry amplitudes ($A_0(I)$) of the non-dissociative (blue), deprotonation (red) and isomerization (yellow) channel. Here, the center-of-mass momenta were used to retrieve the asymmetry amplitudes of the different channels. This figure was taken from [75].

A similar change of the phase offset with respect to the direction and magnitude was observed in the deprotonation channel, indicating similar underlying ionization dynamics in both cases. The lower asymmetry amplitude in isomerization, however, contradicts the theoretical predictions. This discrepancy might be caused by simplified assumptions in the simulations, which are not capturing the following scenario: the hydrogen migration intrinsically stores energy in a rotational motion, resulting also in a rotation of the entire molecule. By such a rotation, the resulting assignment of fragmentation changes its directionality. In other words, a proton moving from left to the right will usually be detected by a carbon emission to the left, but after half a rotation it results in a carbon emission to the right. Thus, the molecular rotation washes out the original CEP-directionality, and hence the asymmetry becomes smaller. Experimental evidence of such a rotation is given in [11] and is furthermore shown in figure 4.6a), where a uniform momentum distribution indicates a Coulomb explosion in all directions, as can be expected from a rotating molecule. With increasing intensity, the energy stored in the rotation is higher, and hence the rotation occurs faster, resulting in a smaller asymmetry. In the simulation, however, no rotation of the molecule is included, resulting in an overestimation of the asymmetry.

As a final comparison of the ionization process for all above shown channels, figure 5.6b) depicts the asymmetry of the center-of-mass motion for the investigated intensity range. The above-mentioned higher asymmetries in the deprotonation channel are clearly visible for intensities from 1.4 - 2.7 $\cdot 10^{14}\,\mathrm{W/cm^2}$. This increased asymmetry amplitude is due to the energetically higher states required to trigger a deprotonation. While the overall shape of the isomerization asymmetry is similar to the other two channels, a considerably lower amplitude was measured. Here, it is important to remind ourselves that the center-of-mass is solely determined by the electronic response to the laser field and hence the ionization process. Thus, all subsequent processes, as for example isomerization, molecular rotation or deprotonation, will not affect the center-of-mass motion. Therefore, a lower asymmetry indicates a less pronounced electron recollision ionization and rather a sequential double-ionization. This observation is in agreement with a measurement performed at slightly higher intensities of $4 \cdot 10^{14}\,\mathrm{W/cm^2}$, where it was shown that electron recollision strongly affects the deprotonation but only slightly influences the isomerization [79].

5.3 Allene

5.3.1 Double ionization of allene

As in the previous section for acetylene, the ionization mechanisms of allene is shown for the center-of-mass motion for the deprotonation channel.

In figure 5.7a), the asymmetry parameter is depicted as a function of intensity and CEP. In figure 5.7b), the asymmetry amplitudes, determined by sinusoidal fits to the ex-

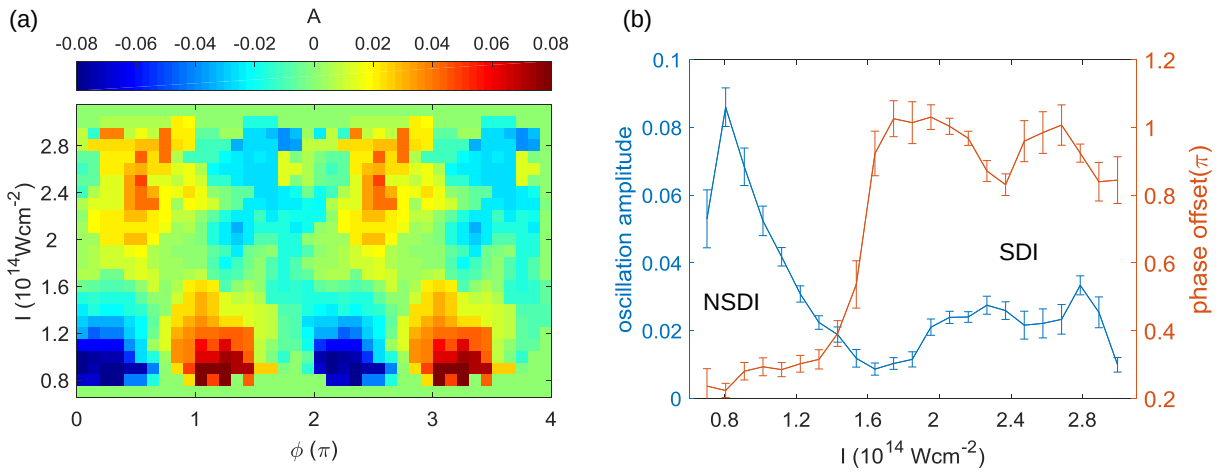

Figure 5.7: a) Asymmetry of the center-of-mass motion in the deprotonation channel of allene ($C_3H_4^{2+} \rightarrow H^+ + C_3H_3^+$) as a function of intensity and CEP. b) Resulting asymmetry amplitude and phase offset obtained from a sinusoidal fit to a). The regimes of non-sequential and sequential double-ionization are denoted additionally for visualization purposes. This image was taken from [75].

perimental data, are presented as a function of intensity. In contrast to the acetylene measurement, a strong change is observed within the scanned intensity range. For low intensities, an asymmetry amplitude of 8 % was observed with an offset of $0.2\,\pi$, see figure 5.7b). At $1.4 \cdot 10^{14}\,\mathrm{W/cm^2}$, a change of the asymmetry amplitude and phase can be observed, which can be attributed to a transition from the non-sequential double-ionization regime to the sequential double-ionization regime. In the low intensity regime, the NSDI mechanism is the driving ionization process. At an intensity of $1.6 \cdot 10^{14}\,\mathrm{W/cm^2}$, the NSDI and SDI mechanisms have similar probabilities and hence the signal vanishes. For even higher intensities, SDI becomes the dominant process. As SDI is almost CEP-insensitive, the asymmetry drops to 2 % and also has a different phase offset. In contrast to the acetylene experiments, in allene the transition from NSDI to SDI was already observed within the investigated intensity range, which is attributed to a lower ionization energy. This observation agrees well with the lower ionization energy of 10.1 eV of allene [80] compared to 11.4 eV of acetylene [81].

5.3.2 Isomerization of allene

In order to investigate the hydrogen migration process in allene, three different two-fold coincidence channels can be used:

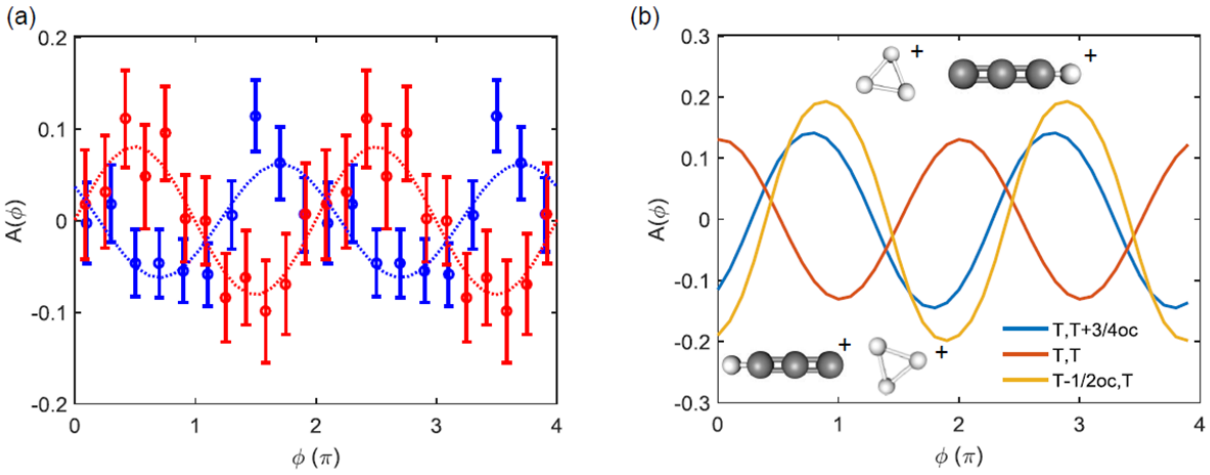

Figure 5.8: a) CEP-dependent asymmetries of H_3^+ emission direction, for the intensities $2.5 \cdot 10^{14}\,\mathrm{W/cm^2}$ (blue) and $2.9 \cdot 10^{14}\,\mathrm{W/cm^2}$ (red), each averaged over a range of $\pm 0.15 \cdot 10^{14}\,\mathrm{W/cm^2}$. b) Theoretical calculations of the asymmetry predicted for an intensity of $3 \cdot 10^{14}\,\mathrm{W/cm^2}$ at different double-ionization times. In the legend, the two times denote the time of the first and second ionization, respectively. The time T represents the time of highest laser fields, and oc stands for "optical cycle". The hydrogen migration direction is depicted by the schematic drawings above and below the asymmetry curves. This image was taken from [75].

$$
\begin{aligned}
(I) \quad & C_3H_4^{2+} \rightarrow CH^+ + C_2H_3^+, \\
(II) \quad & C_3H_4^{2+} \rightarrow C_2H^+ + CH_3^+, \\
(III) \quad & C_3H_4^{2+} \rightarrow C_3H^+ + H_3^+.
\end{aligned}
$$

While all channels can be identified in the PIPICO representation, compare figure 4.7, only the last coincidence channel provides good statistics without any background signal and it is therefore used for further analysis of the hydrogen migration in allene. Thereby, the direction of the H_3^+ emission indicates that the proton has migrated from the opposite side of the molecule. Similar to the carbon emission in acetylene, a CEP-dependent asymmetry of the H_3^+ emission direction shows a control over the hydrogen migration process in allene. Such a CEP-dependent asymmetry in H_3^+ momentum distribution is depicted in figure 5.8a) for two different intensities. While the asymmetry amplitudes are almost equal for both intensities, a considerable shift of the phase offset of almost π was observed. This sudden change in the phase offset is surprising regarding the small intensity difference of $\sim 15\,\%$. It is particularly interesting as, in general, focal averaging cannot be avoided, which largely blurs such defined intensity effects.

One possible explanation for this sudden phase offset shift is a change of ionization process. Similar to the phase shift observed in the center-of-mass of the deprotonation channel, a change from NSDI to SDI might explain such behavior. In order to verify this hypothesis, theoretical calculations of the isomerization process in allene were performed. Thereby, the ionization process was investigated varying the ionization times corresponding to either electron-recollision-based NSDI or to SDI.

In figure 5.8b), the CEP-dependent isomerization asymmetry is depicted for different ionization times of the first (t_1) and second (t_2) ionization step. For the typical electron recollision, the first ionization occurs at the field maximum $t_1 = T$, while the second ionization happens at $t_2 = T + 3/4$ oc, which corresponds to the time between emission and recollision of the electron and parent molecule (see blue curve).
In SDI, the first ionization occurs either at the field maximum $t_1 = T$ (red) or at a half cycle before $t_1 = T - 1/2$ oc (orange). The second ionization is assumed to happen at the time of highest fields $t_2 = T$, as then the ionization probability is highest.

In all cases it is apparent that the theory overestimates the measured asymmetries. This can result from the fact that the ionization is restricted to a single point in time and that molecular rotation is not included in the theoretical model. Furthermore, the phase shifts between the three assumed ionization times are very pronounced. While the electron recollision scenario (blue) and the SDI at different half cycles (yellow) reveal only small phase shifts, the SDI occurring exclusively at the field maximum is shifted by almost π as observed experimentally. For low intensities, an electron recollision is the most probable driving mechanism. While a sequential ionization at different half cycles cannot be excluded, it is less likely than the NSDI mechanism. For higher intensities, the phase shift can be explained by sequential double-ionization occurring exclusively during the crest of the laser field.
By comparison between simulation and experimental data, it becomes apparent that the ionization process in allene changes from NSDI at an intensity of $2.5 \cdot 10^{14}\,\mathrm{W/cm^2}$ to SDI at intensities of $2.9 \cdot 10^{14}\,\mathrm{W/cm^2}$.

5.4 Conclusion

In this chapter, the intensity and CEP dependence of the ionization, deprotonation and isomerization process in acetylene and allene were studied. In acetylene, it became visible that the sequential ionization dominates over the non-sequential double-ionization for increasing intensity. Furthermore, highly excited states were found to play an important role in the deprotonation process as they have a strong CEP dependence. In the isomerization process, however, no such contributions from higher excited states could be observed, which is in agreement with the assumption that only one state that allows for isomerization is

populated in the dication. These observations are furthermore in agreement with theoretical predictions based on vibrational wave-packets evolving on the potential energy surface of the $A^3\Pi$ state of the dication. The phase dependence of these wave-packets is initiated by the CEP of the laser field within the ionization process. However, the simulation does not explain the intensity dependence of the isomerization process – likely, due to the lack of molecular rotation within the model.
In allene, a small intensity change resulted in an asymmetry phase shift of almost π, which can be explained by a transition of the ionization dynamics. This phase offset shift was observed for the center-of-mass motion in the deprotonation channel as well as in the isomerization channel. Using the theoretical model it was shown that a transition from non-sequential to sequential double-ionization is consistent with a phase offset shift of almost π.
In conclusion, it was found that using low intensities results in higher CEP-control over molecular processes such as deprotonation and isomerization. By increasing the laser intensity, the control is not only reduced, but also its directionality can change, as seen in the isomerization of allene. All in all, a control over the isomerization process in acetylene and allene is very dependent on the applied laser intensity as the ionization process predetermines the molecular reaction.

6 Temporal evolution of acetylene upon strong-field ionization

In this chapter, the temporal evolution of processes triggered by a strong-field excitation are investigated using a pump-probe scheme. In order to extract precise timing information as well as to reveal fast occurring processes it is advantageous to use ultrashort laser pulses. In recent years, a special technique based on the extraction of the 3D momenta of three or more molecular fragments in coincidence was applied to reconstruct the molecular structure via Coulomb explosion imaging (CEI) [82, 83]. Having this tool to reconstruct the molecular structure in combination with its timing information allows to visualize the hydrogen migration in "real time" [84]. Especially, the isomerization from acetylene to vinylidene in the coincidence channel $C_2H_2^{3+} \rightarrow H^+ + C^+ + CH^+$ was extensively studied [38, 84–86]. Independent of the chosen excitation wavelength, intensity, or the populated intermediate state the isomerization time was consistently found to be around 50 fs.

In the following chapter, the additional coincidence channel $C_2H_2^{3+} \rightarrow H^+ + H^+ + CC^+$ is exploited to gain a much deeper understanding of the isomerization processes. First, the changes to the experimental setup and the theoretical methods are briefly explained in section 6.1. Afterwards, the observed wave-packet motion is interpreted in section 6.2, whereas the visualization of the bond rearrangement by both three-fold coincidence channels is discussed in section 6.3. This chapter is mainly based on: C. Burger *et al.* [87]

6.1 Experimental and theoretical methods

Experimental setup

To experimentally enable the pump-probe studies, a Mach-Zehnder interferometer is introduced into the beam path (see figure 6.1). In the interferometer, the pulse is split into two identical parts by a 50:50 beamsplitter, delayed in one arm by a nm- resolution delay stage, and recombined at a second 50:50 beamsplitter. A good spatial overlap and temporal profile was checked by an autocorrelation measurement in the experimental chamber. The delay stage was continuously swept between -267 fs and 267 fs ensuring similar conditions throughout the complete measuring time. To furthermore guarantee the reproducibility of

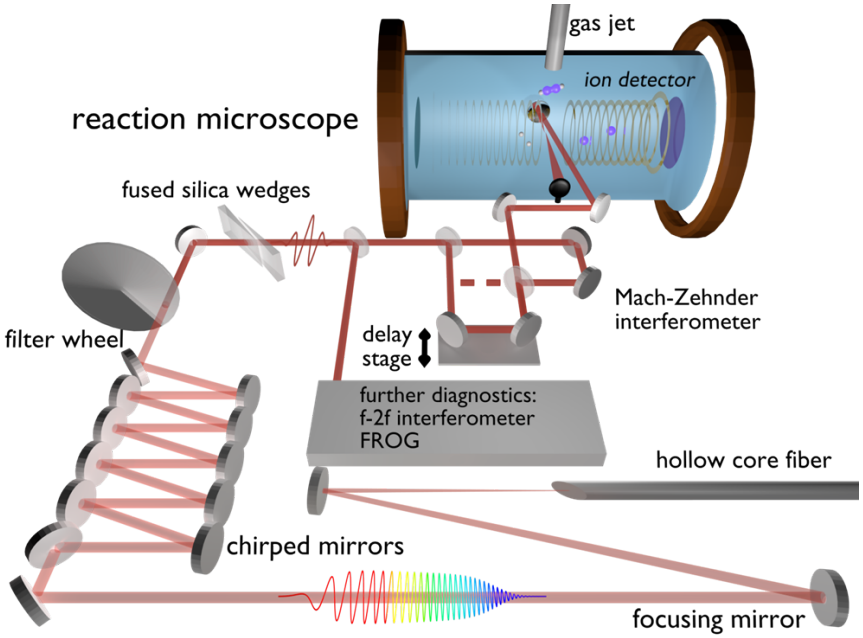

Figure 6.1: Experimental setup of the pump-probe measurements with ultrashort pulses.

the experiment, four individual long term measurements were performed, over 72 hourss in total, which were checked against each other and later combined for the final analysis.

Table 6.1: Presented data are combined from the following measurements

measurement run	1	2	3	4
	coincidences per channel			
$H^+ + C^+ + CH^+$	245552	89274	32796	146586
$H^+ + H^+ + CC^+$	129131	55396	18770	80105
$H^+ + H^+ + C^+ + C^+$	53695	8156	5944	44955

In table 6.1, the amount of coincidences per channel is displayed for the individual measurements. Here, it becomes visible that the $H^+ + C^+ + CH^+$ channel has the highest yield being 80 % higher than that of the $H^+ + H^+ + CC^+$ channel. Owing to the high repetition rate and the long term stability of the laser system, the total amount of data is 5 times larger than the previously reported data [38]. Combining this high statistics with the temporal resolution of the few-cycle pulses facilitates not only the visualization of the isomerization process with unprecedented resolution but also the investigation of the vibrational wave-packet motion in the intermediate state.

Theoretical method

The theoretical simulations, based on the Complete Active Space Self-Consistent Field model (CASSCF), were performed by Robert Siemering from the group of Regina de Vivie-Riedle (LMU Munich) using the program package MOLPRO with the 6-311++G** basis set [88]. For the electron correlation calculation the active space was accommodated to the number of valence electrons and contains the 10 molecular orbitals and all electrons but the 1s-core electrons of the carbon atoms. Hence, the molecular configurations in the dication are calculated using a precise description of excited states. The result of these calculations are shown in figures 6.3 and 6.6.

6.2 Wave packet motion in the intermediate state

The wave-packet motion in the intermediate state is one of the most difficult processes to observe as one needs very high temporal resolution, i.e. for acetylene better than 10 fs, as well as good statistics to reveal the underlying processes. The KER as a function of the time delay between both pulses enabled us to reveal some of the underlying dynamics.

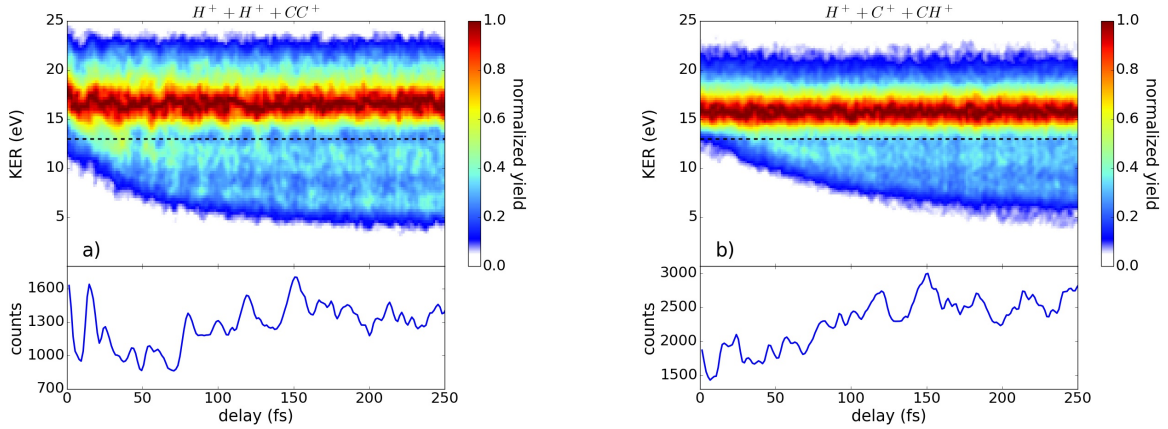

Figure 6.2: The yield of a) $H^+ + H^+ + CC^+$ and b) $H^+ + C^+ + CH^+$ as a function of the pulse delay and the kinetic energy release. The yield is normalized for each time bin, revealing a small oscillation of the peak in yield with delay. The black dashed line indicates the separation of the regions investigated in figure 6.4. In the lower panels the integrated total yield is plotted as a function of delay.

In figure 6.2, the yield of the three-fold coincidence is plotted as a function of the KER and the time delay between both pulses. Several different features become observable:

1. A time dependent contribution becomes visible for low KER (below 13 eV) regions. These coincidences result from molecules that are dissociated by the probe pulse at

larger internuclear distances, which leads to a lower kinetic energy from the Coulomb explosion.

2. Comparing this temporal evolution (KER below 13 eV) in both channels, a slower temporal evolution in the $H^+ + C^+ + CH^+$ channel is detected. Hereby, it is important to remind ourselves that in the $H^+ + C^+ + CH^+$ channel the CC-bond and the CH-bond are probed, while in the $H^+ + H^+ + CC^+$ channel exclusively the CH-bond is investigated. Hence, a slower temporal evolution of the $H^+ + C^+ + CH^+$ channel can be interpreted as a slower elongation of the CC-bond compared to the CH-bond probed in the $H^+ + H^+ + CC^+$ channel.

3. The maximum yield is achieved for coincidences with a KER around 16 eV. While on average, the maximum remains at the initial KER value, close inspection reveals small oscillations around this value. These changes result likely from different bond length at the time of Coulomb explosion, i.e. the probe time. Hence, the vibration frequencies can be inferred from a Fourier analysis of these oscillations.

4. The total yield of the channels also shows an oscillatory behavior indicating a delay dependence of the ionization probabilities. As the ionization probability depends on the bond length these oscillations are likely due to vibrations in the excited molecule.

With observations, 3) and 4), two independent indications for a wave-packet motion in the intermediate state are observed. Inspecting these oscillations by Fourier analysis reveals three major contributions: 11.5 fs ± 1.7 fs, 20.4 fs ± 1.5 fs, and 33.4 fs ± 1.2 fs. To interpret this result calculations of the periods of various stretching and bending modes in the neutral, cation, and dication state were performed.

Table 6.2: Calculated oscillations periods of different modes in the neutral, cation, and dication.

mode	period of oscillation (fs)		
	neutral	cation	dication
trans-bending (x-z and y-z)	59.2 ± 0.6	40.4 ± 0.5 and 70.1 ± 0.7	52.2 ± 0.6
cis-bending (x-z and y-z)	48.1 ± 0.5	40.5 ± 0.5 and 45.4 ± 0.5	47.0 ± 0.5
CC-stretching	16.3 ± 0.5	23.0 ± 0.5	**21.6 ± 0.5**
antisymmetric CH-stretching	10.0 ± 0.4	11.2 ± 0.4	**11.4 ± 0.4**
symmetric CH-stretching	9.7 ± 0.4	10.9 ± 0.4	11.0 ± 0.4

In table 6.2, the different time scales for bending- and stretching motions become obvious. Comparing the experimental results wo these calculated timings the CH-bond stretching mode can be identified with the 11.5 fs ± 1.7 fs oscillation and a CC-bond stretching of the dication with the 20.4 fs ± 1.5 fs oscillation. The slower oscillation period cannot

be identified by the calculations as it is too slow for stretching modes but too fast for bending modes. However, as a stretching of a CC-bond usually results in a shrinking of the CH-bond it is likely that this oscillation of 33.4 fs ± 1.2 fs results from a combination of different stretching modes of the CH- and CC-bonds.

To summarize the observation of figure 6.2, a clear the temporal evolution of the dissociation (see point 1) is observable. Hereby, the slower CC-bond elongation manifests itself by a slower temporal evolution of the dissociation (see point 2). By analyzing the oscillation periods (points 3 and 4), the CH- and CC-bond vibrations in the dication state are identified using our strong-field pump probe scheme.

6.3 Visualization of the hydrogen migration

In our pump-probe experiments a variety of different coincidence channels can be identified. Here, only those channels including the isomerization process are shown:

i) $C_2H_2^{2+} \rightarrow C^+ + CH_2^+$

ii) $C_2H_2^{2+} \rightarrow C_2^+ + H_2^+$

iii) $C_2H_2^{3+} \rightarrow H_2^+ + C^+ + C^+$

iv) $C_2H_2^{3+} \rightarrow H^+ + C^+ + CH^+$

v) $C_2H_2^{3+} \rightarrow H^+ + H^+ + CC^+$

vi) $C_2H_2^{4+} \rightarrow H^+ + H^+ + C^+ + C^+$

In channel i), the fragmentation yield of vinylidene as a function of the time delay can be measured allowing to determine the isomerization time to 52 ± 15 fs as reported by Jiang *et al.* [89] Channels ii) and iii) require a hydrogen migration followed by a stable bond formation of both hydrogen atoms, which is very unlikely to happen and hence the statistics is too low to extract relevant information from those channels. Channels iv) and v), however, provide excellent statistics. Channel iv) was extensively studied (see references [38, 84–86]) to visualize the isomerization process. Channel v) has been proposed by Alnaser *et al.* [63] but has not been investigated so far. Reports of channel vi) have been scarce and are mainly found in combination with three-body coincidences analysis [86] or with deuteriated acetylene [90].

In the following, the focus will be on the three-fold coincidence channels iv) and v). One big difference between these channels concerns the TOFs of their fragments. In channel $H^+ + H^+ + CC^+$, where two hydrogen ions have to be detected, the detection efficiency is lowered due to the "dead time" of the detector. It, however, provides a big difference

in mass of the fragments C_2^+ and H^+. Thus, while the detection is not very efficient the assignment of fragments is unambiguous. Channel $H^+ + C^+ + CH^+$, in contrast, has higher detection efficiency but an overlap in TOF of the C^+ and CH^+ fragments cannot be avoided, leading to false coincidences, which results in a more difficult molecular reconstruction.

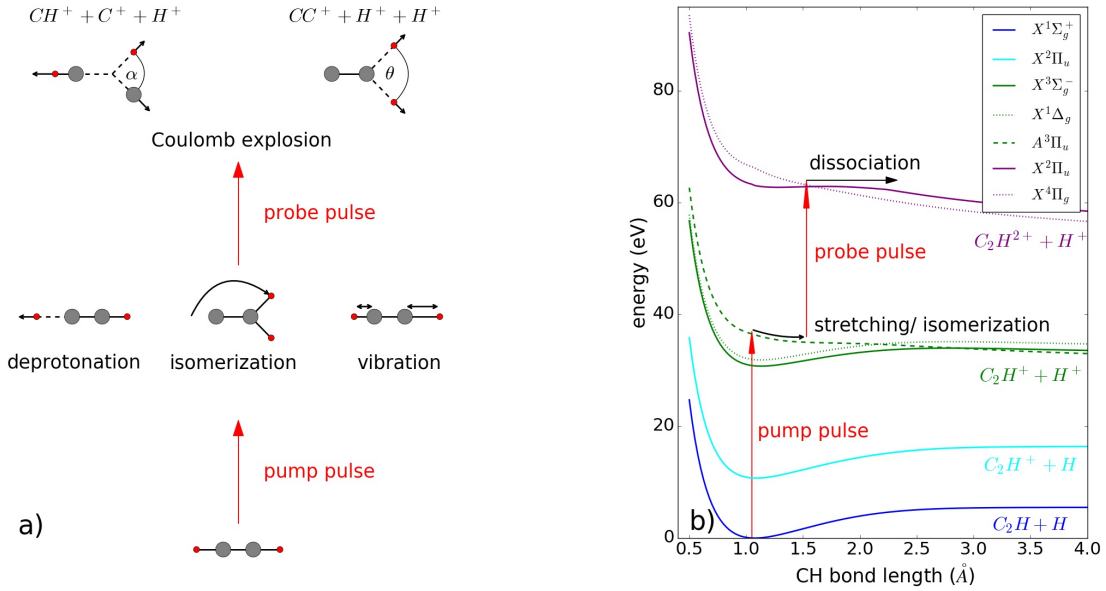

Figure 6.3: a) Illustration of the molecular configurations for different time of the pump-probe experiment. The angles α and θ will be used to discriminate between the vinylidene and acetylene configuration. b) Calculated potential energy curves for the neutral (blue), cation (cyan), dication (green), and trication (purple) ground states and select excited states as a function of the internuclear distance of one CH-bond.

In figure 6.3, an illustration of the different molecular configurations and processes in the intermediate state is depicted along with the calculated potential energy curves for the CH-bond. The pump pulse is ionizing the molecule into either the cation or dication state where various processes can occur, e.g. deprotonation or isomerization. The probe pulse ionizes the molecule into triple or even quadruply charged states from where it dissociates via Coulomb explosion.

This dissociation with three or four fragments allows for Coulomb explosion imaging where the detected 3D momenta are used to calculate the molecular configuration. By defining the angles α and θ to describe the migration of hydrogen (see figure 6.3 a)) the migration process for different time delays can be tracked. To allow for comparison of our results with previous measurements, α is defined as in references [84, 85] and represents the angle between the center-of-mass of the molecule, the carbon ion, and the hydrogen ion (see figure 6.3 a)). The angle θ is spanned between both protons and the C_2^+ ion.

By using the C_2^+ ion as a center, a direct comparison of the experimental results to the calculations shown in figure 6.6 becomes possible.

The identification of the intermediate state in such pump probe experiments is always difficult as the pump pulse usually populates a variety of states. So far, population of the cation states has been reported for XUV and UV pump pulses [38, 86, 91]. In contrast, IR and VIS strong-field excitation populate the dication state [84, 85]. This discrepancy is not completely understood yet but likely it results from different used intensities rather than a wavelength dependency. Using identical pump and probe pulse intensities, as in our experiment, it is energetically favorable to populate the excited dication state (see figure 6.3). By pumping the molecule into an excited state several motions can be triggered, e.g. vibration, dissociation, rotation and isomerization, which are schematically depicted in figure 6.3 a). The gain further insight into the isomerization process the molecular structure is investigated.

Figure 6.4 presents the fragmentation yield as a function of the angles α and θ and the time delay for both coincidence channels. The applied energy filter separates the dissociating contributions at lower KER values (below 13 eV) from the time independent KER region (above 13 eV). In the $H^+ + C^+ + CH^+$ channel, a considerable amount of molecules in the vinylidene configuration at small time delays are observed. This artifact is due to the overlap in the TOF for fast CH^+ fragments and the slow C^+ fragments (compare chapter 4). Hence, in the data analysis the identification of both fragments is can be false, leading to a wrong assessment of the molecular configuration. For the $H^+ + H^+ + CC^+$ channel, the reconstruction of the molecular configuration is thus much more reliable as the TOFs of each fragment are clearly separated. Investigating the angular distribution of the coincidences with high KER reveals that the molecules tend to stay in a bent acetylene configuration, which is seen by the broad and constant distribution around $\alpha \sim 20°$ and $\theta \sim 140°$, respectively. This observation fits to the calculated bent configuration for the excited acetylene molecule (see figure 6.6). Hereby, the excitation energy is transfered into bending motion of the hydrogen atoms. This results in the observed widespread angular distribution around the equilibrium. In contrast to the constant distribution for high KER coincidences, the dissociating molecules, seen in figure 6.4 c) and d), show rich dynamics. In the $H^+ + H^+ + CC^+$ channel most of the molecules undergo isomerization such that more than 60 % of all molecules end up in the vinylidene configuration. In the $H^+ + C^+ + CH^+$ channel, the majority of molecules stay in the acetylene configuration while a slowly increasing contribution of vinylidene molecules can be identified. Interestingly, the migration back to acetylene, as reported previously [84], cannot be observed. This discrepancy could, however, result from the additional background subtraction, applied by Hishikawa *et al.* [84], which accounts for three fold coincidences by single pulse excitation.

By applying a filter based on the angular information the molecules in the vinylidene

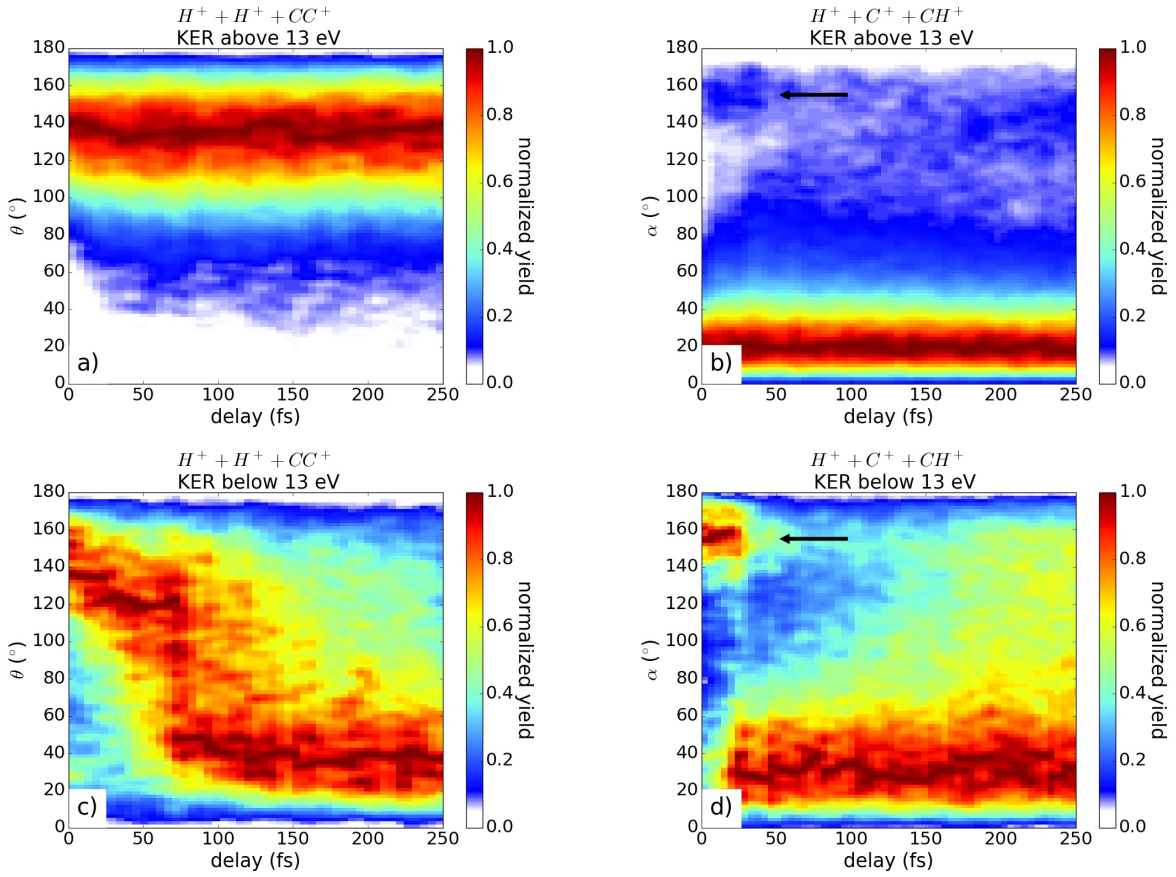

Figure 6.4: Shown is the yield as a function of time delay and angle θ for channel $H^+ + H^+ + CC^+$ in a) and c), and α for channel $H^+ + C^+ + CH^+$ in b) and d). Using the KER filters (indicated above each plot) the bound (13 eV - 30 eV, a) and b)) the dissociating contribution (0 eV - 13 eV, c) and d)) are separated. In b) and d) artifacts, indicated by the arrow, at small delays and large angles are observed due to overlapping time-of-flights of the fragments (see text).

configuration and those coming from acetylene can be separated. Therefore, the following filter are applied: the acetylene configuration is given for all angles α above 90° and all angles θ below 90°, while the vinylidene arrangement is observed for α below 90° and θ above 90° (see figure 6.3 a)).

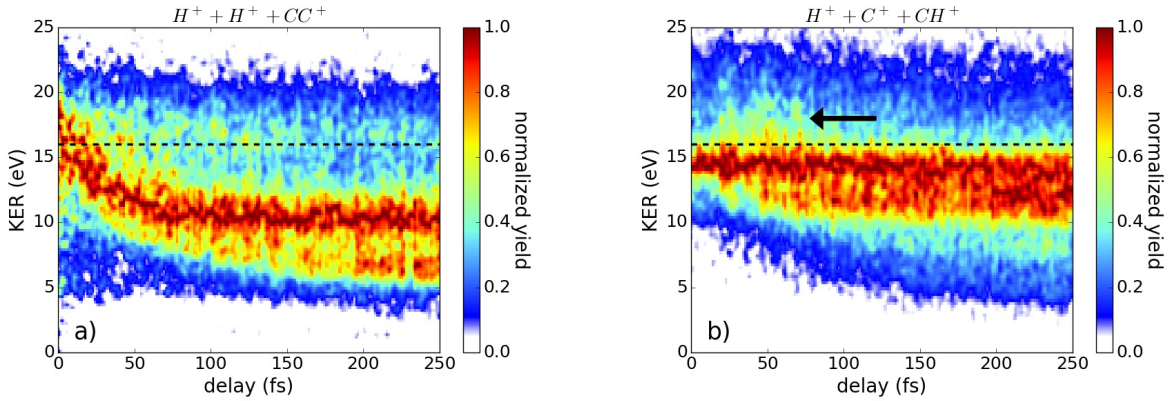

Figure 6.5: Fragmentation yield as a function of the kinetic energy release and the pulse delay for the $H^+ + H^+ + CC^+$ and $H^+ + C^+ + CH^+$ channel, a) and b), respectively. By fulfilling the condition: $\alpha < 90°$ and $\theta > 90°$, all shown coincidences dissociated from the vinylidene configuration. The arrow indicates an area of interest to identify the intermediate state (see text), while the dashed black lines are used in figure 6.7 as a new energy filter.

In figure 6.5, this filter is applied to isolate the isomerized molecules and plot the fragmentation yield as a function of KER and pulse delay. As compared to figure 6.2, the time independent contribution at 16-17 eV is considerably weaker, while the dissociating contribution becomes clearly visible. This result leads to two major insights: First, the majority of isomerizing molecules are dissociating, meaning that the intermediate state is an unbound state. Secondly, the dissociation is too fast to allow the proton to migrate back to the acetylene configuration. Highlighted by the arrow in figure 6.5 b), an increased fragmentation yield with higher KER at delays between 0 fs and 100 fs can be seen. This increased yield in channel $H^+ + C^+ + CH^+$ for high KER values and the delay dependence in both KER plots in figure 6.5, can be explained by an isomerization via the $A^3\Pi_u$ excited dication state as shown by theoretical calculations, see figure 6.6 [92].

According to the calculations molecules which were ionized into the $A^3\Pi_u$ state by the pump pulse will relax into one of the two local minima t1' and t1". Here, the molecule has a bent configuration with 140° between the CC- and CH-bond, which is in agreement with the data of figure 6.4 a). From these local minima the molecule can overcome the energetically higher lying transition states t-TS1' and t-TS1" by changing its configuration. This change results in larger angles, longer CH-bond lengths and shorter CC-bonds. If a

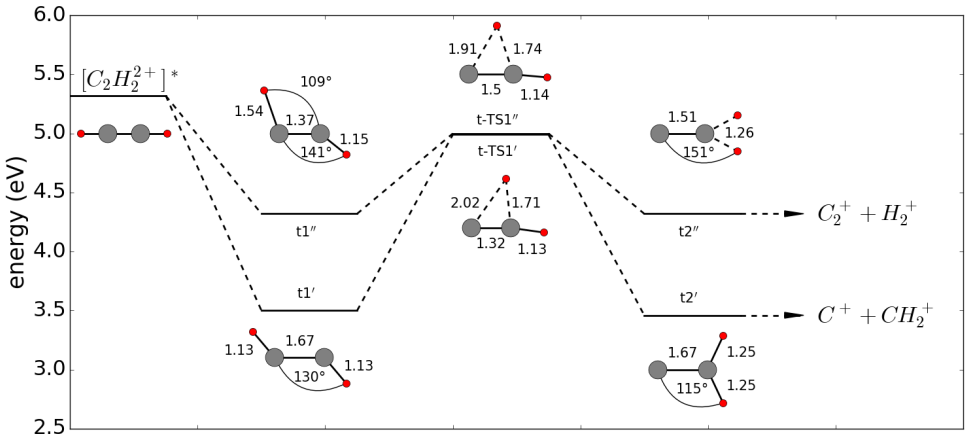

Figure 6.6: Energy-diagram for different configurations of an acetylene molecule in the excited dication state. The states t1' and t1" represent bound molecules in local minima in a bent configuration. Molecules passing the t-TS1' and t-TS1" state will isomerize and dissociate once they reach the t2' and t2" state. The bond lengths are given in units of 10^{-10} m. The idea for this figure was taken from reference [92].

molecule is probed in this intermediate state a high KERs will be detected if the CC-bond is broken and smaller KER if the CH-bonds are broken. In the $H^+ + H^+ + CC^+$ channel, where only CH-bonds are broken, a rapid decrease in KER will be observable, which is clearly visible in figure 6.5 a) within the first 100 fs. In the $H^+ + C^+ + CH^+$ channel, this effect is more difficult to observe as both, the increase in KER owing to shorter CC-bonds and decreased KER by longer CH-bonds, occur simultaneously washing out the signal. However, as the CC-bond stores more energy an overall increase in KER is expected, which is in agreement with the observation of figure 6.5 b) at delay times around 50 fs, indicated by the arrow. Once the molecule overcomes the energy barrier it finishes the isomerization into the t2' and t2" state from where it dissociates. This dissociation is again visible by the decreasing KER contributions for longer time delays in figure 6.5.

Using the angular information, the isomerization time of the acetylene dication. The isomer yield, i.e. the ratio of vinylidene molecules ($\alpha > 90°$, $\theta < 90°$) to all triple coincidences of the corresponding channel, is introduced in the following to also quantitatively investigate the isomerization.

In figure 6.7, the isomer yield is plotted as function of the pulse delay for both investigated channels. We analyzed two different cases: First, all isomerization counts appearing in figure 6.5 are considered to calculate the total isomer yield (red data points). Secondly, only events with KER above 16 eV are investigated, indicated by the dashed lines in figure 6.5.

For the first scenario, the isomer yield is increasing with pulse delay for both channels. In channel $H^+ + H^+ + CC^+$, an asymptotic behavior for long delays is seen implying a

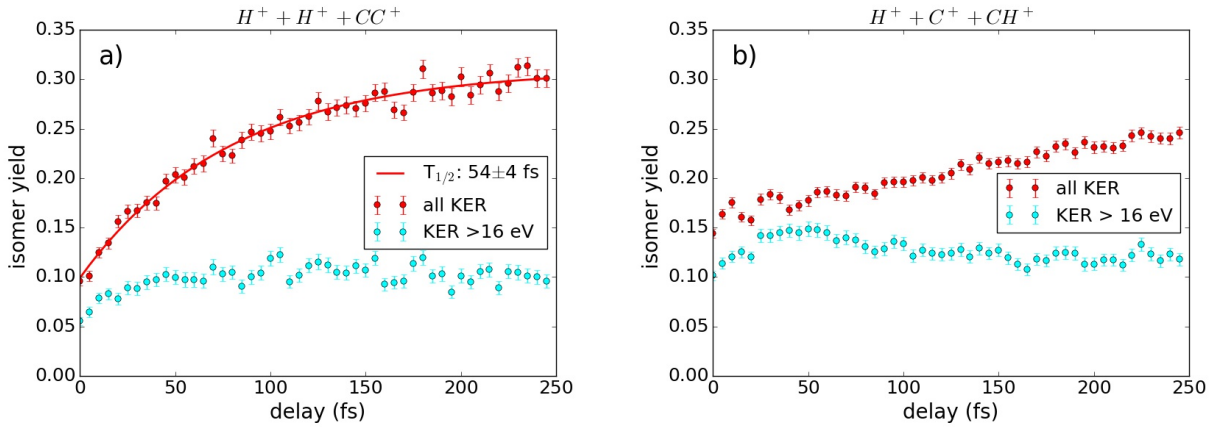

Figure 6.7: Isomer yield of a) $H^+ + H^+ + CC^+$ and b) $H^+ + C^+ + CH^+$ as a function of the pulse delay. The total isomer yield is presented in red, while the data in cyan correspond to events with an additional high-energy filter, KER > 16 eV. The error bars represent statistical errors of the measurement. In a) an exponential fit of the experimental data (red solid line) is used to extract the isomerization time. Please note that the isomer yield at zero pulse delay in (b) is overestimated due to the artifact discussed above.

final isomer yield of around 30-35 %. By applying an exponential fit to this data curve the isomerization time is extracted to be 54 ±4 fs, which is in good agreement with previously reported isomerization times from calculations and measurements [11, 38, 89, 93]. In channel $H^+ + C^+ + CH^+$, an almost linear trend for the measured pulse delays is observed, making it difficult to determine a definite isomerization time. The final isomer yield of 25 % after 250 fs is lower than for the $H^+ + H^+ + CC^+$ channel. As previously discussed, the dissociation along the CC-bond is, due to the larger masses, expected to be slower and hence the dynamics within the $H^+ + C^+ + CH^+$ channel will occur on longer timescales. Therefore, a saturation of the isomerization yield is expected to occur at longer pulse delays resulting also in much longer isomerization times within this channel.

Within the second scenario, using a high energy filter (KER > 16 eV), completely different dynamics are observed. In the $H^+ + C^+ + CH^+$ channel a peak appears at 40 fs reproducing previous measurements [38], which interpreted this as a maximum in isomerization yield followed by a proton migration from vinylidene back into the acetylene configuration [38]. However, as this dynamics cannot be seen in the second coincidence channel, an alternative explanation for this maximal isomerization yield at 40 fs is proposed in the following. While the molecule transfers from the t1' to the t2' state it surpasses the energetically higher lying state t-TS1' (see figure 6.6). This state has shorter CC-bonds resulting in higher KER when probed by Coulomb explosion. For the t2' state the CC-bond length increases again, emerging in a lower KER, where-after the molecule remains in the vinylidene configuration. In other words, by applying the high energy filter not only the isomerization but rather

the CC-bond length is probed. In contrast, in the $H^+ + H^+ + CC^+$ channel, which is less sensitive to the CC-bond length, exclusively the isomerization yield is probed fluctuating around 10 % throughout the complete delay range.

In summary, a clean isomerization signal is observed in the $H^+ + H^+ + CC^+$ channel allowing us to extract the isomerization time as 54 ±4 fs. Furthermore, the $H^+ + H^+ + CC^+$ channel provides additional information on the CC-bond length, indicating that the intermediate state t-TS1' is reached after 40 fs before undergoing the isomerization into the vinylidene configuration.

Newton diagram

To visualize the isomerization, Newton diagrams are depicted for different pulse delays in figure 6.8. To highlight the hydrogen migration without any constant contributions, only the events with a KER between 8 eV and 13 eV are used. Such a Newton diagram presents the 3D momenta of the 3 fragments in the following manner: The heaviest fragment is placed in the center and the first proton (lower TOF) is fixed to the right side of the horizontal axis. By fixing these two ion momenta the parallel and perpendicular component of the remaining proton momentum can be plotted as shown in figure 6.8. As guide to the eye the position of each ion is indicated within each diagram. The hydrogen migration is

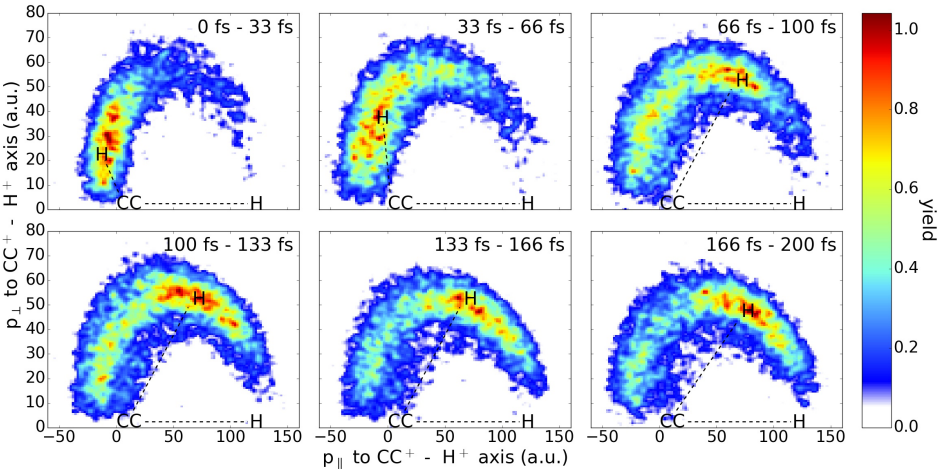

Figure 6.8: Newton diagrams of the isomerization process at various pulse delays (indicated in top right corner of each plot). As a guide to the eye the position of each atom is schematically indicated.

clearly visible within the first 100 fs where afterwards the molecular configuration remains constant.

6.4 Conclusion

In this chapter, a pump-probe scheme with unprecedented temporal resolution was used to gain insight into the evolution of an excited acetylene molecule. By investigating the time dependent fragmentation yield and kinetic energy release vibrational wave-packet motions are identified with periods of 11.5 fs ± 1.7 fs and 20.4 fs ± 1.5 fs resulting from the CH-bond and CC-bond vibration, respectively. Using the Coulomb-explosion technique allowed to reconstruct the molecular configuration at the time of dissociation. Probing at different delay times enabled us to track the isomerization in "real time" and gain further insight into the underlying processes. Assuming the $A^3\Pi_u$ state as intermediate state explains well the experimental results obtained for both triple coincidence channels. First, the molecule relaxes in the quasi-stable t1' state with a bent configuration, which is observed in the non-dissociative regions of the KER spectrum. Parts of the ensemble will pass over the t-TS1' state where the hydrogen migrates and hence the CH-bonds are stretched while the CC-bond is shortened. This state, from where the molecule finishes its isomerization and starts to dissociate is reached within 40 fs. The extracted mean isomerization time of 54 ± 4 fs is in agreement with previous experimental studies [89] [93] [11] and theoretical predictions [92].

7 Nuclear dynamics in acetylene

As the pump-probe studies in the previous chapter showed promising insights in the nuclear dynamics, they were extended with similar experiments on acetylene to investigate the vibrational motion in the intermediate state as well as the process of enhanced ionization (EI). In this chapter, we focus on the two scenarios for the pump-probe experiment that are displayed in figure 7.1.

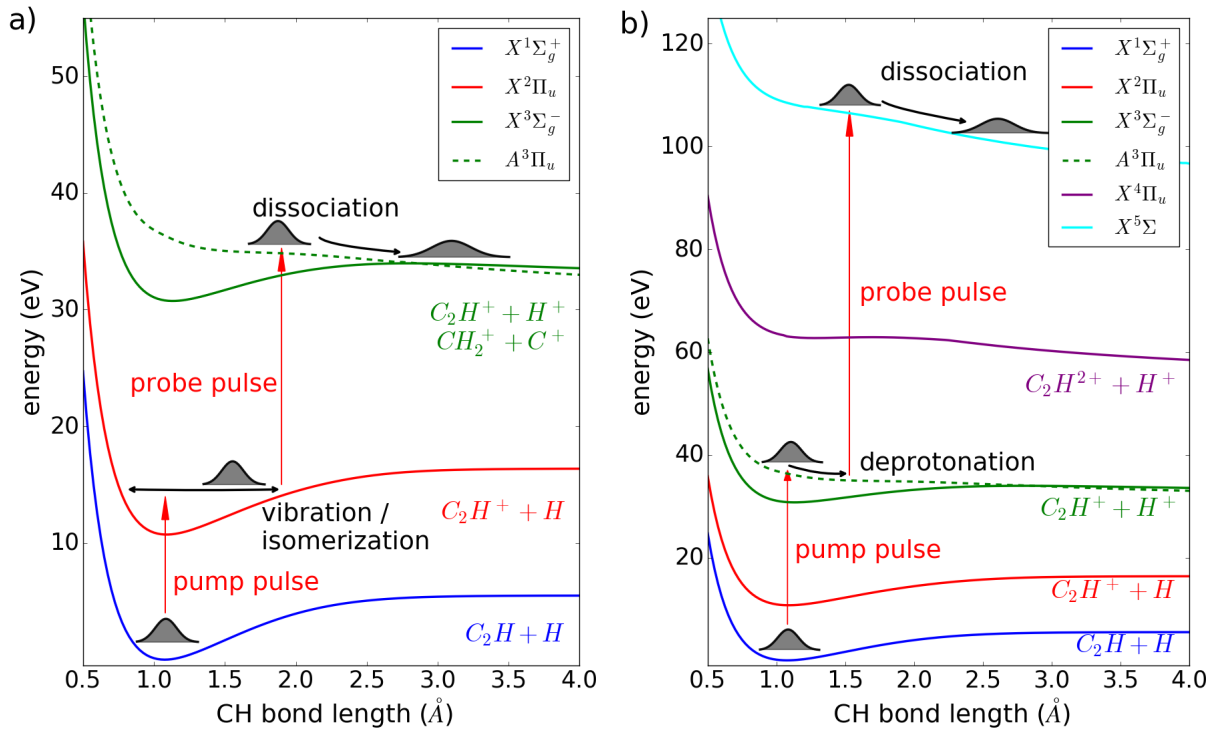

Figure 7.1: Potential energy curves for the neutral and various charged states of acetylene as a function of the CH-bond length. In scenario a), the pump pulse ionizes the molecule into a bound cation state and a subsequent probe pulse leads to the population of a dissociative dication state (here the first excited state of the dication). In scenario b), the pump pulse leads to a population of a dissociative dication state, while the subsequent probe pulse ionizes the molecule into a quadruple charged molecular state, which dissociates into four fragments.

In the first scenario, figure 7.1a), the pump pulse leads to a population of the bound ground state of the acetylene cation, such that the wave-packet starts to oscillate. The wave-packet dynamics is probed by dissociative ionization with the probe pulse. Here, the deprotonation ($C_2H_2^{2+} \rightarrow H^+ + C_2H^+$) and the isomerization ($C_2H_2^{2+} \rightarrow C^+ + CH_2^+$) are two product channels that are observed after dissociative double ionization.

In the second scenario, the pump pulse ionizes the molecule into a dissociative dication state, e.g. the first excited state as displayed in figure 7.1b). Previous work indicated that, at similar laser intensities, this process is facilitated by recollisional ionization after single ionization [6]. The probe pulse enables further ionization into the dissociative quadruple charged molecule, shown in figure 7.1b), which dissociate by Coulomb explosion. Additionally, also the three-fold coincidence channels $C_2H_2^{3+} \rightarrow H^+ + C^+ + CH^+$ and $C_2H_2^{3+} \rightarrow H^+ + H^+ + CC^+$ are investigated (not shown in the graphical representation).

In this chapter, the computational and experimental methods are shortly explained (section 7.1), followed by the investigation of nuclear motion in bound molecules via the two-fold coincidence channels in section 7.2. Subsequently, the effect of EI is introduced in more detail (section 7.3.1). In section 7.3, the experimental and theoretical evidences for enhanced ionization in dissociating acetylene molecules are presented. This chapter presents the results of a collaboration with the group of I. Litvinyuk and R. de Vivie-Riedle.

7.1 Methods

Computational methods

The following simulations were performed and visualized by Thomas Schnappinger. The time-dependent ionization processes were calculated using a combination of non-adiabatic on-the-fly simulations and ab-initio calculations of ionization rates. For these calculations the Complete Active Space Self-Consistent Field method (CASSCF) [94] was employed. The active space provided for the static electron correlation was adapted to the number of the valence electrons consisting of 10 molecular orbitals and the according electrons except for the 1s-core electrons of the carbon atoms, following [4, 95]. The calculations were performed using the program package MOLPRO 2012 [94, 96] with the 6-311++G** basis set [97–99]. To perform non-adiabatic on-the-fly simulations, a modified version of Newton-X [100–102] was used, which supports the usage of Molpro 2012.

Sets of respectively 100 trajectories were propagated in the ground state of the acetylene cation ($X^2\Pi_u$) and the first dissociative state of the dication ($A^3\Pi_u$) both starting from a Wigner distribution around the ground-state equilibrium geometry. The propagation time for the $A^3\Pi_u$ state was 100 fs and for the $X^2\Pi_u$ state 200 fs, both with a step size of 0.25 fs. For 20 typical trajectories the ionization probability (hereafter called rate) was

calculated with the ansatz described in references [103, 104]. In this ansatz, a quantum chemical calculation for a given molecular geometry with and without a static electric field is performed. Based on the obtained two electronic densities the tunneling rate can be extracted. For acetylene the highest three occupied orbitals are included to build up the electronic densities. In the current work, an angular dependence for the ionization was not included.

Experimental methods

In our time-resolved experiments, a femtosecond pump-probe setup was utilized, as described in [87]. In brief, a few-cycle laser pulse with a pulse duration below 5 fs was divided into two pulses in a Mach-Zehnder interferometer. The temporal delay between both pulses was adjusted by a linear nm-resolution translation stage in one arm of the interferometer. The delay was continuously swept between 0 fs and 120 fs, with one complete scan taking around 5 minutes, whereas the total scan duration was about 12 hours. By analyzing the individual short-term scans long-term drifts could be identified and compensated. The pulse duration of the individual arms were measured independently by a frequency-resolved optical-gating (FROG) technique behind the interferometer [45]. Additional laser parameters such as spectrum, power, and focal spot size were recorded before and after the scan to ensure similar conditions throughout the entire measurement. Both laser pulses were subsequently intersected with a jet of neutral acetylene molecules in a REMI, where the 3D momentum distributions of all charged particles resulting from the laser-molecule interaction were measured. In the here shown experiments, the detection of coincident fragment ions from the dissociation of the molecule induced by both pulses is used to distinguish the fragmentation channels. Both few-cycle pulses had an intensity of around $5 \cdot 10^{14}$ W/cm^2, permitting single or double ionization of acetylene by a single pulse.

7.2 Nuclear dynamics of bound molecules

In order to investigate the temporal evolution of the wave-packet in the bound cation, created by the pump pulse, the kinetic energy release (KER) of the ionic fragments, which are created by the probe pulse, are analyzed as a function of the delay between both laser pulses.

In figure 7.2, the ionization yield is depicted as a function of KER and delay for the deprotonation channel and the isomerization channel in figure 7.2a) and figure 7.2c), respectively. In figure 7.2b) and d), the KER-integrated signal as a function of delay is depicted. Since the probe step leads to a population of a dissociative dication state, see figure 7.1a), the KER is an indicator of the bond length in the cation. A short bond length

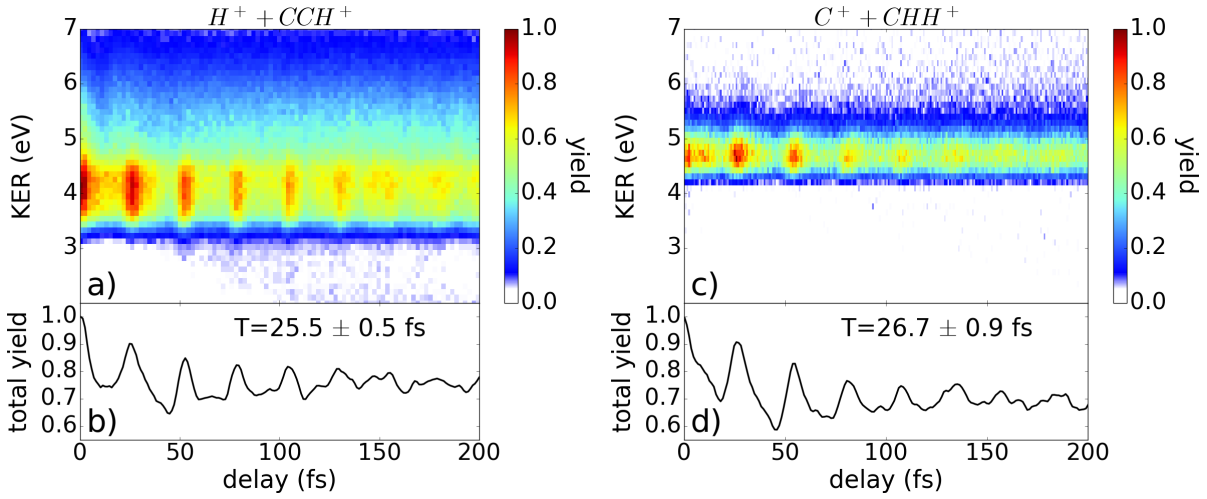

Figure 7.2: Ionization yield of a) the deprotonation and c) isomerization channel as a function of the kinetic energy release (KER) and the delay between pump and probe pulse. b) and d) represent the KER-integrated signal as a function of delay.

results in a higher KER and vice versa. As visible in figure 7.2a) and c), the KER remains rather constant over time, which is a strong indication of bound nuclear wave-packet motion in the cation.

The overall temporal evolution of the yield is similar within both investigated channels. This is of particular interest, as the mean isomerization time observed for the acetylene cation is around 50 fs [38, 89]. Therefore, a probe pulse after e.g. 15 fs should not reveal isomerized molecules in any state of the cation. This discrepancy can be explained as follows: The pump pulse excites molecules in a superposition of many states within the cation, which results in a mixture of molecules which only vibrate and some which additionally start to isomerize. The subsequent probe pulse excites the molecule into multiple dissociative states within the dication. From these excited states, the molecules can undergo deprotonation or isomerization reactions, which are triggered by their initial momentum from the populated electronic state in the dication.

Furthermore, a considerable modulation in ionization yield as a function of time is observed in both channels, compare figure 7.2b) and d), revealing vibrational motion in the cation. The vibrational periods are extracted as 25.5 ± 0.5 fs in the deprotonation channel and 26.7 ± 0.9 fs in the isomerization channel.

To explain the observed periods in the ionization yields, the nuclear dynamics in the ground state of the acetylene cation ($X^2\Pi_u$) were simulated. The theoretical results for the dynamics of the acetylene cation are summarized in figure 7.3.

All bonds in the acetylene cation show clear oscillation dynamics, see figure 7.3a) and b).

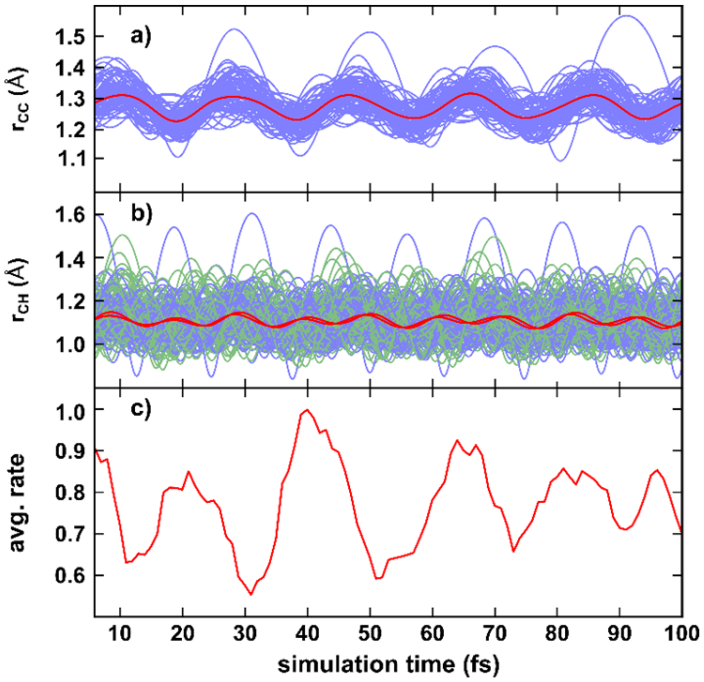

Figure 7.3: a) Simulated temporal dynamics of the carbon-carbon bond in the ground state of the acetylene cation shown in blue for all trajectories and in red for the averaged value. b) The temporal evolution of both carbon-hydrogen bonds in the ground state of the acetylene cation displayed in blue and green for all trajectories and in red for the averaged values. c) Calculated time-dependent averaged ionization rate of 20 exemplary trajectories propagating in the ground state of the acetylene cation.

The CC bond length varies between 1.1 Å and 1.5 Å (equilibrium distance around 1.2 Å) while the length of both CH bonds varies between 0.9 Å and 1.6 Å (equilibrium 1.06 Å). The averaged CC-bond has a vibrational period of about 20 fs while both CH-bonds oscillate with 15 fs. The averaged CH bonds are moving nearly in phase, observable by the almost perfect overlap of both red solid lines in figure 7.3b).

The average ionization rate was calculated for 20 exemplary trajectories, see figure 7.3c). A clear periodic modulation of the ionization rate was observed with a period around 22 fs. This timing agrees well with the experimentally observed temporal evolution of the ionization yield. The combined motion of the CC- and both CH-bonds induce the observed periodic change of the ionization rate. Comparing the averaged values of r_{CH} and r_{CC} around the peaks of the ionization rate, an antisymmetric behavior can be seen: Either the CH bonds or the CC bond elongates, while the other type of bond is shortened.

The simulations show that the vibrational motion in the bound ground state of the cation leads to periodic enhancement of ionization, which experimentally manifests in the periodic yield modulation. These results are in accordance with experiments performed on molecular hydrogen [6] and deuterium [105, 106].

7.3 Enhanced ionization of dissociating molecules

7.3.1 Introduction of enhanced ionization

The interaction of molecules with intense laser pulses typically results in ionization. Upon ionization of a molecule, its structure and its chemical properties can change drastically, and chemical reactions may be initiated [5]. EI is known to alter the ionization probability of molecules at an inter-nuclear distance of around twice the equilibrium bond length [107]. The process of double ionization via EI can be understood for the diatomic case as follows (see figure 1) [107]: First, a diatomic potential well, with an inter-nuclear distance of r being the equilibrium distance R_{eq}, is bent by a strong laser field such that an electron can tunnel through the outer barrier into the continuum, cf. figure 1a). Upon nuclear motion induced by the first ionization, the inter-nuclear distance increases while an inner barrier between both nuclei emerges. At a critical distance R_c, the (inner) barrier towards electron tunneling becomes smaller than the outer barrier, considerably enhancing the rate for double ionization (enhanced ionization), cf. figure 1b). When the inter-nuclear distance increases further, the inner barrier becomes larger and enhanced ionization ceases, cf. figure 1c). The simple picture for a diatomic molecule does not easily apply anymore to complex molecules where multiple bonds are involved. In the case of acetylene, both the CC-bond (depicted in figure 1) and the CH-bonds can elongate as a result of the first ionization step, providing a multi-dimensional landscape for enhanced ionization.

In 1995, Zuo *et al.* [108] theoretically predicted enhanced ionization in H_2^+ ions for

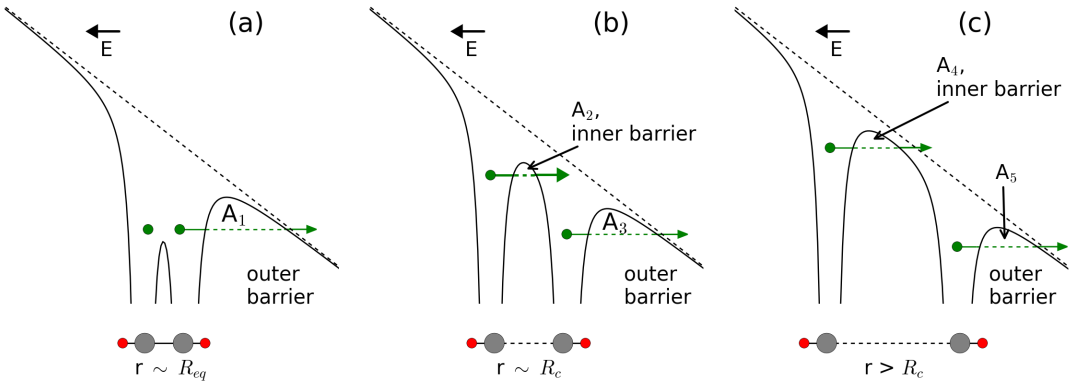

Figure 7.4: Schematic representation of enhanced ionization: molecular potentials (black solid lines), which are dressed by the laser field (E, black dashed lines), for different inter-atomic separations: a) at the equilibrium distance R_{eq}, b) at a critical distance R_c, and c) at even larger separations $R > R_c$. Electrons are depicted as green points with arrows indicating tunnel ionization through the barriers. The areas A_n can be seen as measure of the tunnel ionization probability: small areas result in large ionization probabilities and vice versa. Below each panel, as an example, enhanced ionization with respect to the CC-bond in acetylene is depicted with carbon (grey) and hydrogen (red) atoms.

a charged resonance between two strongly coupled states. As this process depends on the inter-nuclear distance, which is changing after the first laser-molecule interaction, its temporal evolution is of particular interest. Ergler *et al.* performed first time-resolved pump-probe measurements on hydrogen [109], followed by more extensive work on H_2 [110, 111] and on D_2 [63]. Another method of probing EI is to change the pulse duration and thereby investigate the role of EI on the ionization probability [112–114]. Wu *et al.* verified that in the process of EI the potentially high-lying nucleus is ionized using circularly polarized pulses [107]. Theoretical calculations were able to reproduce EI both in simple hydrogen [115] and in more complex acetylene [116, 117] showing the importance of two or more interacting states where charge-resonance enhanced ionization (CREI) can occur.

Experimental work on complex molecules is still scarce. Recent work on EI in acetylene showed that this process occurs at bond lengths which are about twice as large as the equilibrium value of the CH-bond [73]. Recently, Erattupuzha *et al.* found that CREI in acetylene originates not only from coupling of two states but rather due to an energy upshift and field coupling of multiple orbitals [118]. Following this argument, EI in complex molecules such as acetylene is not limited to a single critical inter-nuclear distance but can include a broader range of inter-nuclear distances, which are possibly assumed during a longer time intervals of molecular motion initiated by e.g. the ionization of the neutral molecule.

Here, we go beyond previous single pulse experiments [73, 118], investigating the enhanced ionization in acetylene by a time resolved study. The joined experimental and theoretical work provides insight into enhanced ionization in dissociating acetylene molecules.

7.3.2 Investigation of the four-fold coincidence

Enhanced ionization for dissociating molecules is observed in the second scenario of figure 7.1, where initially a dissociative dication state is populated by the pump pulse. The temporal evolution of this wave-packet is then observed by further ionization through the probe pulse. Here, the four-fold coincidence channel $C_2H_2^{4+} \rightarrow H^+ + C^+ + C^+ + H^+$ that results from interaction with both pulses is investigated.

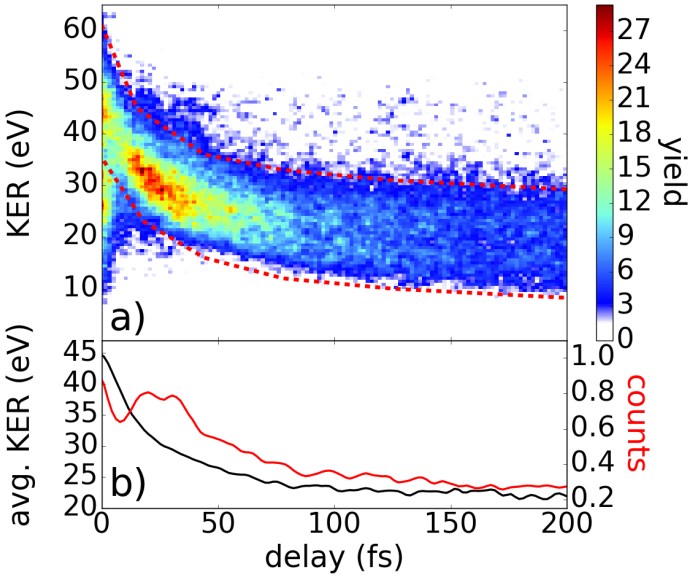

Figure 7.5: a) Ionization yield of the four-fold coincidence channel as a function of KER and delay. b) The one-dimensional representation of the normalized KER-integrated signal including all counts within the dissociative area (red line) and the average KER of the dissociative events as a function of the delay (black line). To select dissociative molecules, only events within the red dashed lines are considered.

In figure 7.5a), the ionization yield of the four-fold coincidences from this channel is shown as a function of KER and delay between pump and probe pulses. The area within the red dashed lines corresponds to the measured signal from dissociating molecules. The one-dimensional representation, depicted in figure 7.5b), represents the integrated signal (red) and the average KER (black) for dissociating molecules. In figure 7.5c), the results

of the theoretical calculations are depicted. The average KER (black) and total ionization rate (red) are shown as a function of the delay between the pump and probe pulse.

The average KER is decreasing with the delay time from about 45 eV to 22 eV. Compared to figure 7.2 almost no delay independent KER contribution was detected, which indicates that all molecules detected in this channel undergo dissociation in the intermediate state and furthermore that the pulse energies are sufficiently low to suppress background from a single pulse.

Regarding the temporal evolution, it can be concluded that the applied pulses are short enough to separate the maximum yields at the temporal overlap and the subsequent peak starting at 10 fs. Previous time-resolved measurements on EI suffered from interferences with a period of 2.7 fs created by pre- and post-pulses [63, 109–111]. Here, however, the experimental data are not influenced by any interference due to a very clean temporal profile. As the yield maximum at the temporal overlap does not occur due to an enhanced ionization effect but rather stems from the superposition of both pulses, this effect is not captured by the simulations.

Regarding the ionization yield in figure 7.5a), a clear indication of enhanced ionization in acetylene is observed. Compared to previous measurements performed on H_2 [109–111] and D_2 [63], the temporal evolution of acetylene shows a very similar behavior, i.e. a maximum occurs in the ionization yield within the signal of the dissociating molecules, indicating an enhanced ionization of dissociating molecules. Around the temporal overlap, a strong signal is detected which decreases with time. After a few fs, the ionization yield increases from about 10 fs to 40 fs. For longer delays above 40 fs, the ionization yield is decreasing again.

For a better understanding of the observed enhanced ionization process the nuclear dynamics in the first dissociative state of the acetylene dication ($A^3\Pi_u$) were simulated. The theoretical results are summarized in figure 7.6.

The temporal evolution of all bond length in the dication of acetylene is displayed in figure 7.6a) and b). All 100 trajectories show deprotonation on the timescale of a few femtoseconds (below 60 fs). On average, the leaving proton is around 2 Å away from the remaining C_2H^+ fragment after around 10 fs. In this fragment, an oscillation of the remaining bonds is observed. The CC bond has a period of around 20 fs and the CH bond of around 10 fs.

The averaged time-dependent KER and ionization rate of 20 exemplary trajectories are displayed in figure 7.6c). The average KER is decreasing from about 45 eV to 22 eV within the first 60 fs. The ionization rate increases beginning from about 10 fs to 30 fs. For simulation times longer than 30 fs, the ionization yield is decreasing again. An enhanced ionization rate along the CH bond occurs at the critical bond length of around 2.0 Å after 10 fs, which corresponds well to the experimentally observed starting position of the yield enhancement. Compared to the simulations, the experimentally observed peak in EI is

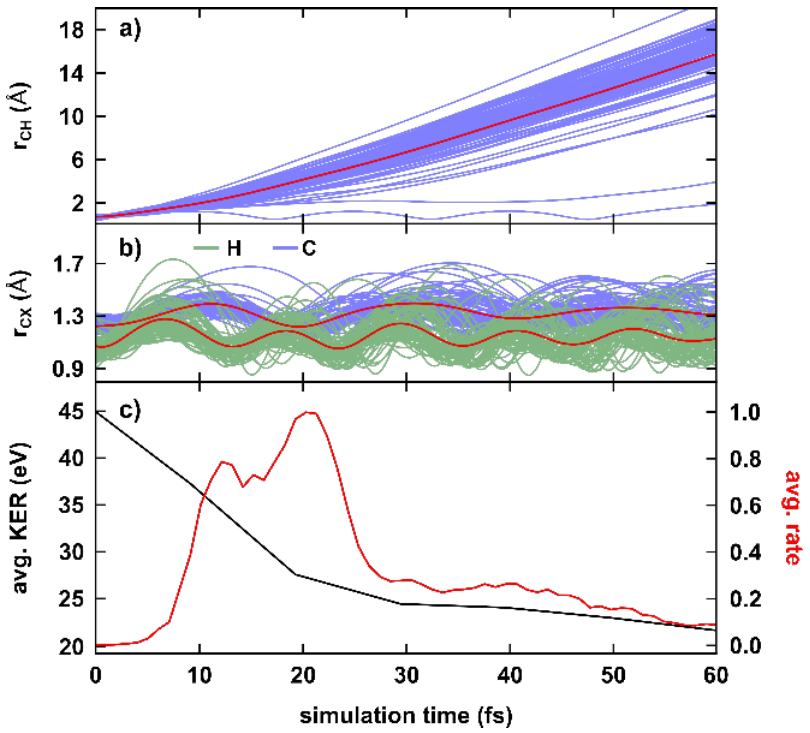

Figure 7.6: a) The temporal evolution of the breaking CH bond in the first dissociative state of the acetylene dication shown in blue for all trajectories and in red for the averaged value. b) The dynamics of the remaining CH bond (green) and the CC bond (blue) in the first dissociative state of the acetylene dication displayed for all trajectories and in red for the averaged values. c) Calculated time-dependent the KER and ionization rate of 20 exemplary trajectories propagating in first dissociative state of the acetylene dication.

slightly broader, which may be due the used CASSCF method, which overestimates the steepness of the potential energy curve in the dication state leading to a faster nuclear motion. Another reason may be, that the simulation includes only one single intermediate state, which is a simplification as likely not only one single dissociative state is populated but rather a multitude of states with different potential energy surfaces. As the time to reach the critical bond distance can vary for each state, the peak becomes broader.

7.3.3 Investigation of the three-fold coincidences

In order to get more insight into the EI process, also the three-fold coincidence channels $C_2H_2^{3+} \rightarrow H^+ + C^+ + CH^+$ and $C_2H_2^{3+} \rightarrow H^+ + H^+ + CC^+$ are investigated with respect to signs of enhanced ionization.

In figure 7.7a) and c), the ionization yield is depicted as a function of the delay for both three-fold coincidence channels. Similar to the four-fold coincidence channel, most of the

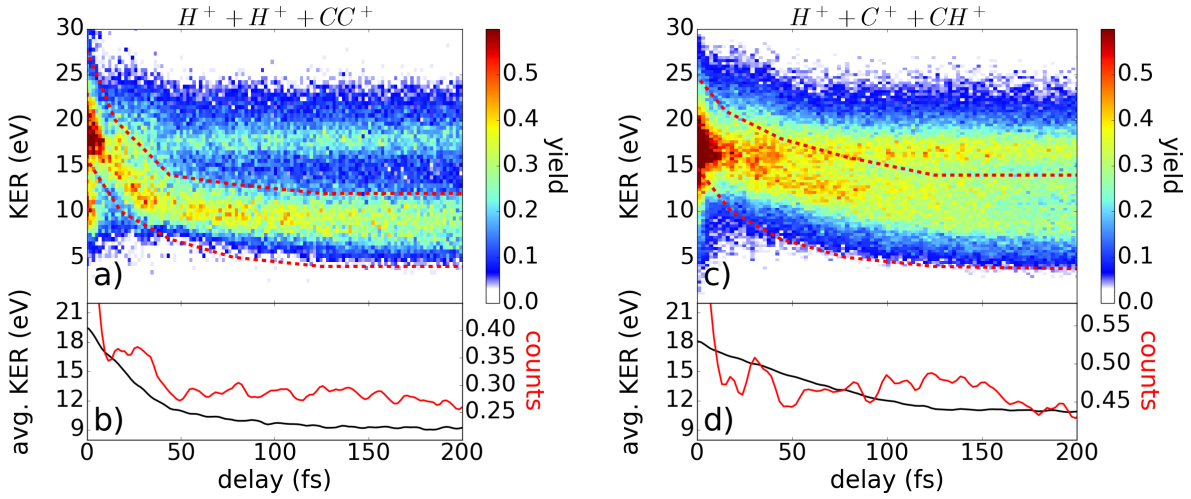

Figure 7.7: a) and c): Ionization yield as a function of KER and delay of the coincidence channels $C_2H_2^{3+} \rightarrow H^+ + H^+ + CC^+$ and $C_2H_2^{3+} \rightarrow H^+ + C^+ + CH^+$, respectively. b) and d): The one-dimensional plot represents the normalized KER-integrated signal including all counts within the dissociative area (red lines) and the average KER of the dissociative events (areas in between red dashed lines in a) and c)) as a function of the delay (black lines).

molecules dissociate. These dissociating molecules are selected by the red marked filter and further analyzed in b) and d) with respect to their relative counts and the average KER. In figure 7.7b), a peak/plateau in the ionization yield is observed in-between 10-40 fs. In comparison to the four-fold coincidence channel, here, the peak can be attributed to a pure CH-bond elongation.

In figure 7.7d), a small peak around 30 fs is observed, which fits well to the observations of enhanced ionization discussed above. Regarding the temporal evolution of average KER, it becomes obvious that the $C_2H_2^{3+} \rightarrow H^+ + H^+ + CC^+$ channel dissociates faster than the $C_2H_2^{3+} \rightarrow H^+ + C^+ + CH^+$ channel. Both observations can be explained by the fact that, in the $C_2H_2^{3+} \rightarrow H^+ + C^+ + CH^+$ channel, not only the CH-bond but also the CC-bond is elongated. Thus, the temporal evolution of the dissociation process and therefore also the enhanced ionization is washed out and hence not as clearly visible as in the $C_2H_2^{3+} \rightarrow H^+ + H^+ + CC^+$ channel.

7.4 Conclusion

In this chapter, the nuclear motion of acetylene was temporally resolved by a pump-probe experiment. Thereby, the pump pulse can either initiate a vibrational motion in the cation,

which is observed in two different two-fold coincidence channels or it excites the molecule such that it starts to dissociate.

In case of the bound cations, vibrational wave-packet motion could be observed via the increased ionization rate at the longest CC-bond distances. Wave-packet periods of 25.5 ± 0.5 fs for the deprotonation channel and 26.7 ± 0.9 fs for the isomerization channel were observed. This observation was confirmed by simulations of bound cationic acetylene molecules, highlighting the importance of the binding strength of the CC-bond. For the dissociating acetylene molecules, the process of enhanced ionization was measured experimentally via three- and four-fold coincidence channels to occur between 10 fs and 40 fs. The detailed information gained in the time-dependent studies show that reaction microscopy and non-adiabatic on-the-fly simulations are powerful tools to investigate the dynamics of enhanced ionization and related strong-field phenomena in complex molecules.

8 Multi-color synthesizer for coherent control and time-resolved studies

Many molecular processes happen at conical intersections of two energy surfaces. One example is the isomerization of acetylene in the cation, where the $A^3\Sigma_g^+$ state crosses the $X^2\Pi_u$ state [38]. Once a wave-packet reaches such an intersection, it has several possibilities to evolve resulting often in a superposition of states. It would be very advantageous to control the wave-packet motion at the conical intersection, as it would increase the amount of control as compared to the single pulse CEP control shown in chapter 4. In order to perform such an experiment, the molecule has to be excited into the relevant state and then the wave-packet motion has to be controlled at the conical intersection and the result of the control has to be probed. Hence, the experimental setup has to fulfill the following criteria:

1. The pump pulse has to efficiently excite the molecule into the reactive state. Any excitation into non reactive states results thereby in background signal, which is often impossible to disentangle from the real signal.

2. The second pulse has to control the wave-packet motion at the conical intersection. The timing of the control pulse is thereby of outermost importance as it will determine the amount of control over the wave-packet motion.

3. The result has to be probed; and depending on the investigated system different possibilities are feasible. In the case of isomerization in acetylene, it might be advantageous to ionize the molecule further to allow for Coulomb explosion imaging (see chapter 6).

In order to fulfill all these conditions, we built a new multi-color setup, where a first UV-pulse (264nm) efficiently excites the molecule and then a combination of fundamental and its second harmonic will act as control and pump pulse. As this experiment is very complex, the measurements are still under investigation – a detailed explanation will be given in section 8.4. However, the applicability and first experimental results of the synthesizer are presented in the following. In the beginning of this chapter, an introduction into the field of pulse synthesis and multi-color experiments is given (section 8.1). Subsequently,

the experimental setup for the multi-color synthesizer is explained (section 8.2) and first results on two-color experiments are presented (section 8.3). In the last part, the challenges of three-color experiments in combination with multiple coincidence measurements are discussed in detail. This chapter is mainly based on: C. Burger *et al.* [23]

8.1 Introduction into multi-color synthesis

Since more than twenty years, the interaction of matter with laser pulses of controlled waveform, such as few-cycle pulses with stable carrier-envelope phase or multi-cycle pulses composed of multiple colors, is studied. These waveform-controlled pulses permit a high degree of control of electron dynamics [19, 20, 119], and also over molecular processes [120–125].

Overlapping the fundamental and its second harmonic, in the following referred to as $\omega/2\omega$ fields, is a well-known method to control the ionization yield [126, 127] and to steer the emission direction of electrons and ions [104, 128]. Such $\omega/2\omega$ fields, which are based on pulses from Ti:sapphire lasers, were employed to study electron dynamics in atoms [129, 130] and electron-nuclear dynamics in molecules [104, 119, 130]. In recent years, these studies were extended to orthogonally polarized [131] or counter-rotating circularly polarized $\omega/2\omega$ fields [132]. Furthermore, $\omega/2\omega$ fields can be used for all-optical orientation of molecules [133, 134], efficient terahertz generation [135], creating isolated attosecond pulses [136], and increasing the yield of high-harmonic generation (HHG) [137, 138].

Previous theoretical and experimental investigations using a composition of fundamental and third harmonic fields, in the following referred to as $\omega/3\omega$ fields, focused mainly on the yield in HHG, and the control of the ionization yield of atoms and molecules [122, 139–143]. As an example, Watanabe *et al.* [139] demonstrated that the yield in HHG can be increased by an order of magnitude upon addition of a 5 times less intense 3ω pulse to the fundamental laser pulse. In a recent publication, Xu *et al.* presented the momentum distribution of protons after dissociation of H_2^+ ions, where again a yield modulation in dependence of the relative phase was detected [144].

Theoretical reports show that a combination of all three laser fields will allow to further increase the HHG yield and eventually even support isolated attosecond bursts [145]. Moreover it was shown theoretically that such $\omega/2\omega/3\omega$ synthesized fields can be used to significantly enhance the generation of terahertz radiation [146]. The possibility of combining more than just two wavelengths opened the new field of sub-cycle pulse synthesis [18]. Since Wirth *et al.* [53] demonstrated field synthesis of three independent channels obtained from dividing an 1.5-octaves white light generated in a hollow core fiber, the coherent addition of spectrally separated beams became an important tool in strong field physics [147, 148]. Such sub-cycle waveforms opened the possibility of generating optical

pulses with sub-femtosecond duration, which was successfully used for probing attosecond electron dynamics [149]. Another approach relies on the coherent combination of pulses from optical parametric amplifiers operating at different wavelengths [150]. This approach was demonstrated in the mid-infrared region with microjoule pulse energies [151]. Due to the relatively long optical beam paths, however, such a device requires active stabilization of the interferometer with attosecond precision. From the experimental point of view, both approaches represent a significant challenge, making simpler designs of field synthesis desirable. Utilizing three-color $\omega/2\omega/3\omega$ fields, generated from a Ti:sapphire laser, was demonstrated by Wei *et al.* [137], where selective enhancement of a single high harmonic in argon gas was achieved. Although the approach seems to be very simple and stable, it inherently did not permit an independent control of the delay between the three colors. Moreover, the polarizations of the beams were fixed (the polarization of the second harmonic beam was perpendicular to the other beams), thus significantly limiting its applicability. To overcome those limitations, here we introduce a device, which combines the advantage of both approaches: the simplicity of optical nonlinear harmonic conversion with the flexibility of field synthesis.

In the following, we demonstrate efficient generation of the second and third harmonic of a femtosecond laser pulse from a Ti:sapphire laser system, followed by a compact and versatile three-color synthesizer. The output of the synthesizer is used to investigate the interaction of neon with the combined $\omega/2\omega$ and $\omega/3\omega$ laser fields, by measuring the momentum distribution of Ne^+ ions from the strong-field ionization of neon. To interpret new experimental findings, we compare the measured data with semi-classical simulations based on the simple man's model [25].

8.2 Multi-color-pulse generation and synthesis

The setup for generating the second and third harmonic of the driving field and for three-color synthesis is schematically shown in figure 8.1. It is based on a Ti:sapphire laser system with pulse durations down to 25 fs and an energy of up to 720 µJ at a repetition rate of 10 kHz (Femtopower Compact Pro HR, Spectra Physics). We took special care to achieve a high third harmonic yield through sum-frequency generation (SFG) in a collinear configuration, following the idea proposed by Kardaś *et al.* [22], and the experimental implementation by Ibrahim *et al.* [38] In short, the laser passes through the following series of optical components: a 200 µm thick β-barium borate (BBO, type 1) crystal cut at 27.2° for second harmonic generation (SHG), a birefringent material to retard the fundamental beam (450 µm thick BBO, type 1, cut at 70°), a $\lambda/2$ quartz wave-plate to rotate the polarization of the fundamental beam with respect to its second harmonic, and a 100 µm thick BBO (type 1) cut at 44.3°, where sum frequency mixing allows for efficient SFG. In

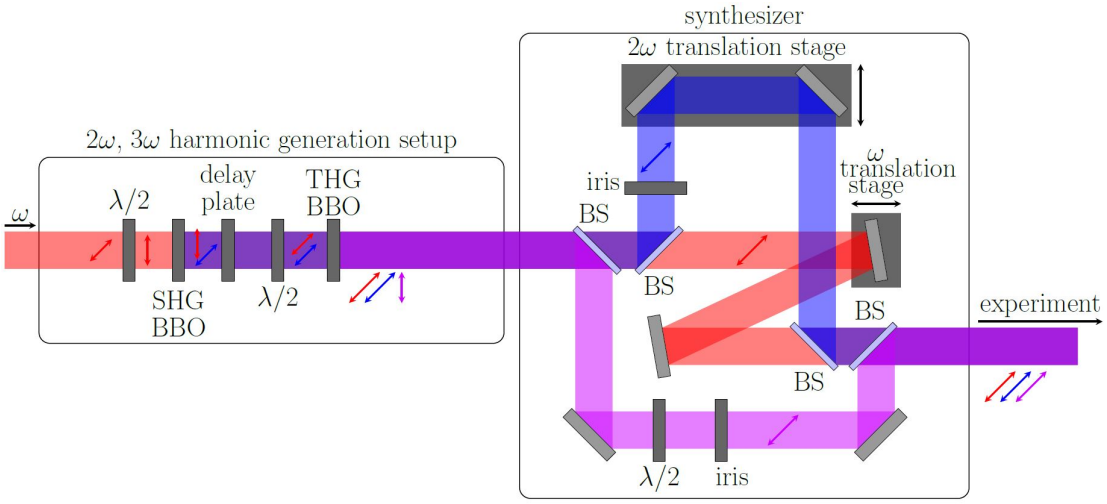

Figure 8.1: Experimental setup for the multi-color pulse generation and synthesis. SHG: second harmonic generation, SFG: sum frequency generation, BBO: β-barium-borate crystal, BS: beamsplitter, $\lambda/2$: half waveplate.

the second part of the setup, the second and third harmonic beams are separated from the fundamental beam using a combination of a custom-made triple band dichroic beamsplitters (BS) facilitating low group delay dispersion (below 50 fs^2), and supporting the full bandwidth of each harmonic. Each coating supports high reflectivity (above 99%) at 45° and high transmission (above 99%) for each corresponding harmonic. The beamsplitters were fabricated on 1 mm thick substrates made of fused silica to minimize additional pulse elongation. An anti-reflection coating, of similar thickness as the front coating, was applied on the back side of the BS for two reasons: First, to prevent a post pulse created from the Fresnel reflection on the back side of the optic. Secondly, to reduce stress induced by the single side coating of the thin substrate, which would result in avoidable wavefront distortions. Such separation of the harmonics into individual channels enables us to control each color independently with respect to energy, delay and its polarization. The colors corresponded to central wavelengths of 790 nm (ω), 395 nm (2ω), and 264 nm (3ω), see figure 8.3. The electric field composed of all three colors can be written as:

$$E(t, \phi_2, \phi_3) = E_\omega \cos(\omega t) + E_{2\omega} \cos(2\omega t + \phi_2) + E_{3\omega} \cos(3\omega t + \phi_3), \tag{8.1}$$

where $E_{\omega,2\omega,3\omega}$ represent the amplitudes of the electric field, ω is the fundamental frequency, and $\phi_{2,3}$ denote the relative phase between the fundamental and the second or third harmonic, respectively. This relative phase can be translated into the relative delay between the synthesizer arms, and is controlled by nanometer-precision delay stages. To achieve high passive stability of the synthesizer, optical mounts were carefully cho-

sen to avoid mechanical resonances, verified by recording the interference stability using a reference continuous wave (cw) laser. Additionally, the setup was housed to avoid air fluctuations. Thanks to the compact footprint of the synthesizer (each beam path length is around 30 cm), and isolation from environmental disturbances, passive sub-100-mrad stability over a 15-min timescale was achieved. In order to account for unavoidable long term drifts we continuously swept the delay stage between a relative phase of 0 and 4π (one complete sweep within 10 minutes). These short-term measurements were then analyzed individually. Any phase drifts between these short term measurements were shifted to the starting value within the post analysis enabling a combination of all measurements for the complete measuring time of 12 hours. Within these 12 hours a slow total phase drift of $\pi/2$ was observed, which had to be compensated by the post analysis.

An efficient frequency conversion of short pulses is a challenging task. It is often a compromise between conversion efficiency (requiring longer crystals and higher intensities) and pulse duration, which is elongated by the group velocity mismatch between interacting beams in the conversion crystals. Careful numerical simulation of the third harmonic generation using a nonlinear propagation software [22] provided optimal parameters for the intensities, and crystal thicknesses, which allowed obtaining high conversions efficiency, while only slightly elongating the pulses in time. With an input energy of 650 µJ in front of the frequency converter and an intensity of 160 GW/cm^2, we were able to generate the three colors with respective final energies of 350 µJ (ω), 90 µJ (2ω), and 80 µJ (3ω) at the output of the synthesizer. This corresponds to over 12 % conversion into the third harmonic, including losses in the synthesizer setup. According to the simulations, after the harmonic generation setup all beams have close to Gaussian beam profiles. This was experimentally verified by recording in the focal plane Gaussian distributions for each harmonic (see figure 8.2).

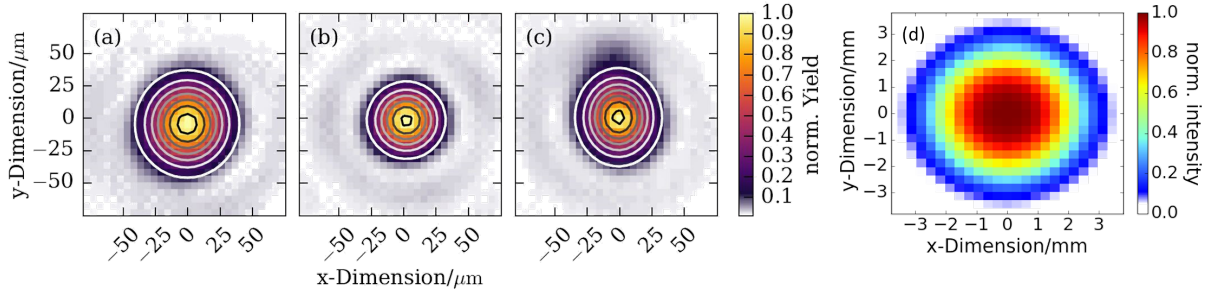

Figure 8.2: Recorded images of the foci of the fundamental (a), second harmonic (b) and third harmonic (c) beams. The contour plots are Gaussian fits to the intensity maps. (d) Spatial beam profile of the fundamental beam, calculated after harmonic conversion setup.

As seen in figure 8.2, Gaussian beam profiles for each harmonic were observed at the focus, and hence, we can assure that the beam does not experience any significant distor-

tion. The "well behaved" conversion also shows in the high intensities, which have been achieved in each individual beam (any distortion will decrease the achievable intensities).

In figure 8.3 (a), the calculated evolution of energies of all three harmonics during nonlinear propagation inside the second BBO crystal is shown. Discrepancies between calculated and measured pulse energies are due to an uncertainty in the crystals thickness (which is typically tens of micrometers for such thin crystals). Moreover, the simulation does not include optical losses on the optical interfaces in the harmonic generation setup as well as the waveform synthesizer. Measured spectra of the three beams after the field synthesizer are shown in figure 8.3 (b) as red lines and correspond well to the calculated ones, shown as black lines.

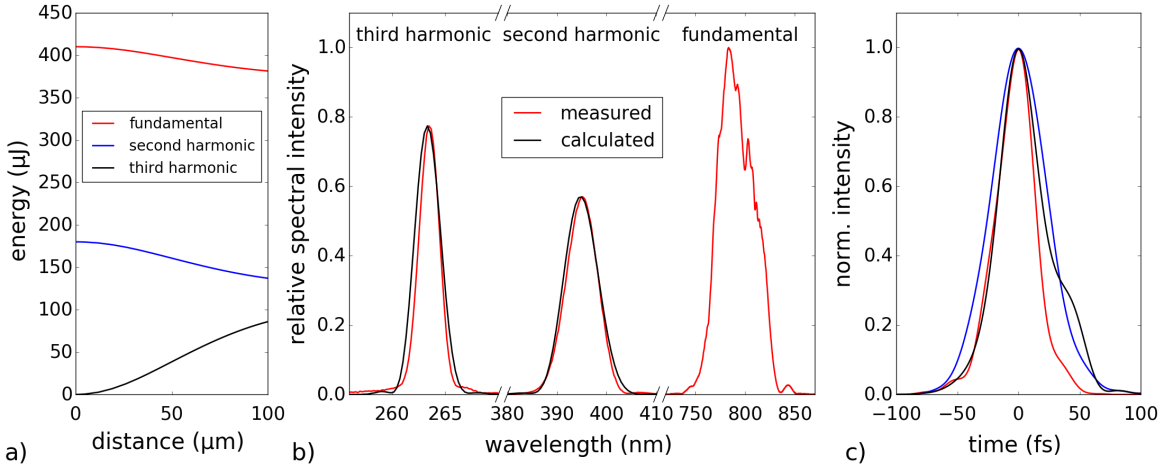

Figure 8.3: (a) Simulated evolution of pulse energies of all three harmonics of the sum-frequency mixing process within the second BBO-crystal. (b) Measured (red) and calculated (black) spectra of the fundamental, second harmonic and third harmonic. While the height of the fundamental beam is normalized, the spectral intensities of the second and third harmonic are calculated according to their relative pulse energies. (c) Calculated temporal profiles of the three beams after propagation through dispersive media.

Due to the propagation through dispersive material in the field synthesizer, additional 2 m of air, and the entrance window (1 mm SiO_2) into the experimental chamber, the pulses get stretched in time. The resulting calculated temporal profiles for the three beams in the interaction region are shown in figure 8.3 (c) with temporal full-width-at-half-maxima (FWHM) of 35 fs, 52 fs, and 42 fs for the fundamental, second and third harmonic, respectively. The pulse duration of the fundamental pulse was verified by TG-FROG measurements, while cross-correlation measurements were used for the second and third harmonic. The retrieved pulse durations are 35 fs (ω), 61 fs (2ω), and 59 fs (3ω), cf. tabel 8.2. The discrepancies could be the result of higher nonlinearities experienced by the second and third harmonic during propagation through the dispersive elements. To decrease the pulse

duration down to the Fourier limit one could introduce chirped mirrors in each arm of the synthesizer at the cost of a longer beam path making the synthesizer more complex, and reducing the throughput.

For the experiments on neon, the polarization of the 3ω beam is turned by 90 degrees to achieve parallel polarization of all three colors. Additionally, the size of the third harmonic beam was adjusted via an iris to match the focal spot size of the fundamental beam. Afterwards, the beams are recombined and sent directly into the experimental chamber. The experimental setup consists of a REMI, which allows retrieving the 3D momentum of each ionized particle on a single shot basis. The spectrum, the pulse energy and the focal spot size were determined before and after each measurement in front of the REMI. A summary of the laser parameters is shown in table 8.2. It is worth mentioning that only a small fraction of the pulse energies were needed for the presented experiments. The intensities were chosen such that the observable shifts in momentum distribution became as clear as possible while background signal from ionization by a single harmonic was minimized. We estimate that the numbers in table 8.2 for the intensities, pulse durations, and focus sizes have an uncertainty of about 20 %, which, however, is not crucial for the observed control.

Table 8.1: The laser parameters of the fundamental, second harmonic and third harmonic for the measurements using $\omega/2\omega$ and $\omega/3\omega$ configurations. The two applied energies of the fundamental beam for the two sets of measurements are shown along with the corresponding intensities.

	Wavelength (nm)	Pulse energy (μJ)	τ_{FWHM} (fs)	Focus size (μm)	Intensity (10^{13} W/cm^2)
ω (in $\omega/2\omega$ fields)	790	39	35	40	6.1
ω (in $\omega/3\omega$ fields)	790	76	35	40	12
2ω	395	27	61	31	4.1
3ω	263	10	59	35	1.3

8.3 Two color synthesis

To prove the applicability of the synthesizer we measured the momentum distribution of Ne^+ in $\omega/2\omega$ fields. In figure 8.4, the dependence of ionization yield of neon on the ion momentum and relative two-color phase ϕ_2 is shown. The observed horizontal stripes correspond to peaks from above-threshold ionization (ATI) and are in good agreement with peak positions calculated from the photon energy of the fundamental light (shown in grey in the left panel). In agreement with earlier work, we observe that the final momentum exhibits characteristic oscillations as a function of the relative phase [129, 130].

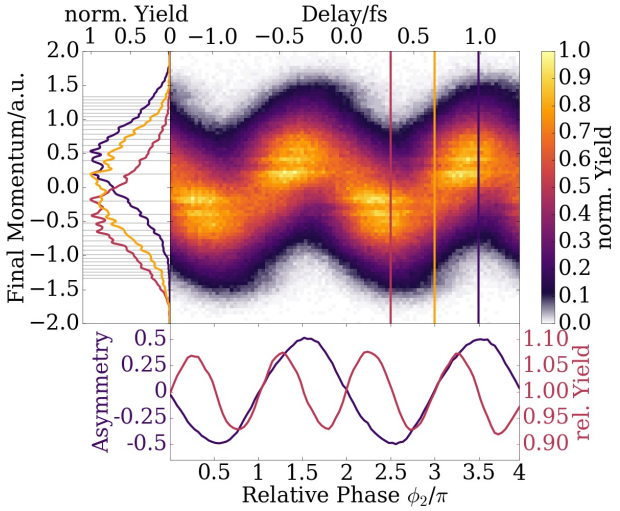

Figure 8.4: Control over neon ionization in $\omega/2\omega$ fields. The ionization yield is plotted as a function of momentum along the polarization direction and relative phase of the two-color ($\omega/2\omega$) field. The lower panel presents the relative total yield, abbreviated as "rel. yield" (red), and the asymmetry of ion emission direction (purple). In the left panel the momentum distributions at the three indicated relative phases are plotted.

In order to quantify the phase-dependent momentum shifts, we define an asymmetry parameter A(ϕ) as:

$$A(\phi) = \frac{L(\phi) - R(\phi)}{L(\phi) + R(\phi)}, \tag{8.2}$$

where L(ϕ) and R(ϕ) denote the yield of ions emitted with positive and negative momentum along the laser polarization direction, respectively. The resulting asymmetry A(ϕ) is plotted in the lower panel together with the relative total ion yield, where unity corresponds to the phase averaged yield. The π-periodicity of the total yield results from occurrences of field crests resulting in higher ionization twice per fundamental laser period. The asymmetry oscillates with a periodicity of 2π and its amplitude (50 %) demonstrates very high control over the ion emission direction. This experiment clearly shows that strong control over the direction of electron emission can be achieved with such synthesized waveforms, being in agreement with previous studies [104, 128]. This will allow e.g. to steer various molecular processes, compare references [125, 152, 153].

In the following, we present experimental and theoretical results on the control of the ionization of neon in $\omega/3\omega$ fields. In figure 8.5, we show the ionization yield as a function of the momentum and the relative phase between the ω and 3ω fields for experimental (a) and theoretical (b) results. The relative phase was varied from 0 to 6π to confirm the periodicity of the observed pattern. Similar to the $\omega/2\omega$ case, we again observe ATI peaks originating from the fundamental wavelength. More dominant, however, is the broadening

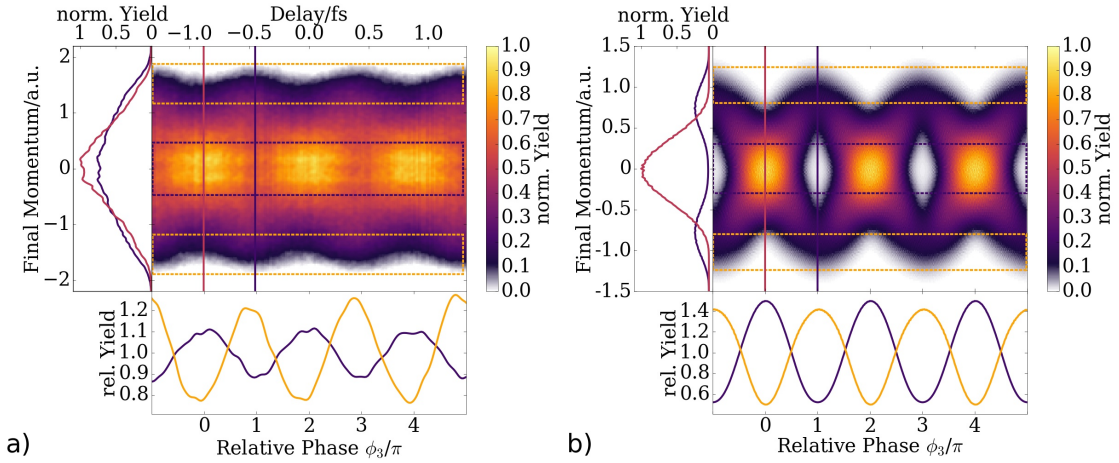

Figure 8.5: Control of neon ionization in $\omega/3\omega$ fields. The ionization yield is presented as a function of the Ne^+ momentum along the polarization direction and the relative phase between the laser fields for (a) experimental and (b) calculated results. In the lower panels the integrated ionization yield is shown for the areas marked by correspondingly colored dashed lines while the left panel presents the momentum distribution along the line cuts in the 2D plot.

of the momentum distribution for phases that are odd multiples of π. This broadening is highlighted by two selected momentum spectra (8.5 (a)) for positions depicted by the two vertical lines in the experimental results.

In order to understand the underlying physics behind the observed control of Ne^+ momenta in $\omega/3\omega$ fields, we have used semi-classical simulations based on the simple man's model [25], in which the ionization rate is calculated by the modified Ammosov, Delone, and Krainov (ADK) rate using the formula of Ref. [35] for ionization in a quasi-static field. This modification allows covering the tunnel ionization regime as well as the barrier suppression regime [35]. After ionization, the electron is propagated classically along the polarization direction neglecting all interactions with the parent ion. The two-color field is described as:

$$E = E_\omega \cos(\omega t) + E_{3\omega} \cos(3\omega t + \phi_3), \tag{8.3}$$

where ϕ_3 denotes the relative phase between the fundamental and the third harmonic. In the simulations, the intensity averaging over the focal volume is taken into account assuming a Gaussian intensity profile and neglecting intensity variation along the beam propagation axis. The latter assumption is reasonable since the Rayleigh-lengths for all colors were larger than 4 mm, exceeding the dimension of the gas jet (several 100 µm) in the REMI. We find best agreement with the momentum shifts observed in the experiments when the intensities used in the simulation are 3 times higher than the experimentally retrieved intensities. The fact that electron momenta are systematically underestimated

in a semi-classical approach is known (see for instance [75, 154]). We note that the simple model cannot capture all details of the process, however, we would like to emphasize that a higher-level of theory was not essential here, since the results rather serve to demonstrate the capabilities of the waveform synthesizer.

When we compare our experimental results to the simulations, we find qualitative agreement with respect to the observed phase control of the ionization yield and the shift in the oscillatory patterns at low and high Ne^+ momenta. To investigate the yield modulations in more detail, we separate two momentum regions: high momenta, marked by yellow rectangles, and low momenta, depicted in purple. The corresponding integrated signals are shown in the lower graph. The phase dependent modulation of the yield for low momenta amounts to 10 %, while the modulation depth increases to 20 % for high momenta. A phase-independent signal at low momenta is seen in the experimental data, which likely contributes to the smaller modulation at low momenta. Intensity fluctuations are unlikely to cause this background, since simulations show that the momentum shifts should still be observed for intensities varied by one order of magnitude. We believe that the constant background can rather be attributed to an imperfect overlap of the two fields in the focus, i.e. where an atom only experiences one of the two laser fields. Moreover, a phase shift of π is observed between the low and high momentum regions, which is also retrieved in the simulations.

In order to better understand the atom-laser interaction in the case of $\omega/3\omega$ fields, we present in figure 8.6 the calculated electric field (solid purple line), the corresponding final momentum (dashed green line), the ionization rate calculated by the ADK rate (grey area), and the final momentum distribution (green area on the right) for two different relative phases ϕ_3.

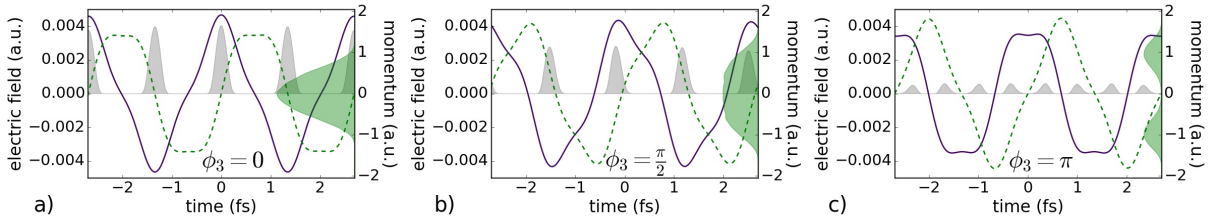

Figure 8.6: Control of Ne ionization yield and Ne^+ momenta in $\omega/3\omega$ fields. Depicted are the electrical field (solid purple line), the ionization rate (grey area) and the final momentum (dashed green line) and its distribution (green area) for relative phases of $\phi_3 = 0$ in a), $\phi_3 = \pi/2$ in b), and $\phi_3 = \pi$ in c), respectively.

For a relative phase of zero, we see that the final momentum distribution peaks around zero as it would be expected from ionization in just a single-color field. Increasing the relative phase to π, we observe two phenomena: First, the overall ionization rate becomes

lower, which was previously seen in several calculations and measurements [140, 141]. This decreased ionization yield results from lower absolute fields and hence lower ionization rates. Secondly, a splitting of the final momentum distribution becomes clearly visible. This splitting can be related to the vector potential. For a relative phase of π, the ionization rate is highest for times when the final momentum is non-zero. Depending on the cycle of the ionization, the final momentum is either negative or positive. Furthermore, the range of the final momenta increased by 50 % compared to a relative phase of zero. It is also important to notice that the ionization yield for a relative phase of π is 8 times lower than for a relative phase of zero. Therefore, in an experiment, which is only sensitive to the overall ionization yield, a 2π-periodic modulation would be observed, with lowest yield corresponding to a phase of π [139, 141, 142].

8.4 Three-color experiments

As discussed in the beginning, a three-color experiment is needed to excite the molecule by the 3ω pulse and to control and probe it by the combined $\omega/2\omega$ fields. However, to obtain a decent signal strength in such an experiment becomes difficult, due to the severe noise resulting from the UV photons. In the following, this problem is discussed in detail with the first experimental results.

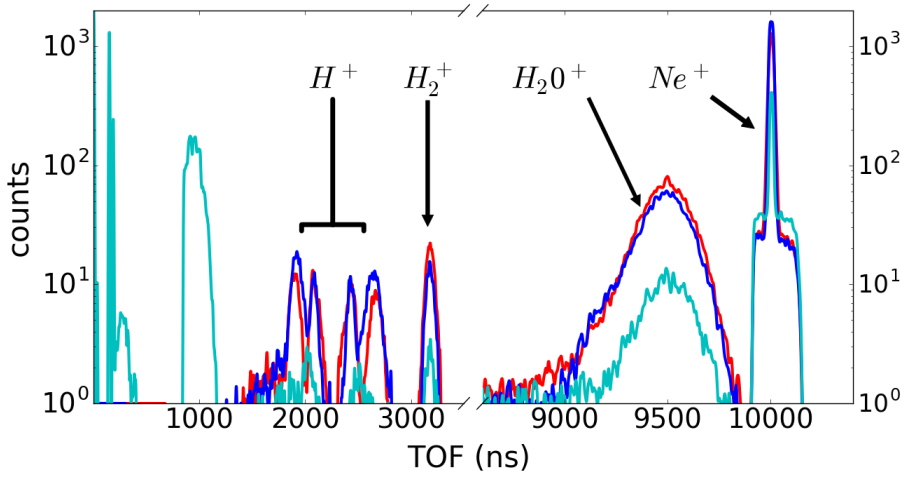

Figure 8.7: Time of flight spectrum of neon gas ionized by the fundamental (red), the second harmonic (blue), and the third harmonic (cyan). All spectra contain the same total number of counts. A time window condition (9.8-10.2 µs) is applied such that a TOF spectrum is only recorded once an ion is detected within this time window (compare section 3.4.1). The ionized species are labeled within the graph. Any signal before 1500 ns does not result from ionic fragments but can be seen as noise.

In figure 8.4, the TOF spectra are shown using only the individual colors for ionization, i.e. the fundamental alone (red), the second harmonic (blue), and the third harmonic (cyan). For all three colors, different ionic fragments are visible. The target gas neon is clearly visible as a defined peak at 10 µs. Around that peak a clear cut in the background signal is visible, which is due to the applied time window. This window allows to reduce signal from unwanted ionic species (see section 3.4.1). All seen counts outside of this time window result from "false" coincidences: signal acquired within the same laser shot as the counts in the time window. As neon required high intensities, a strong background signal from water in the experimental chamber is usually observed.

In contrast to the fundamental and second harmonic, the third harmonic has 40 % of its total yield at very low TOFs (below the TOF of hydrogen). These counts are likely due to scattered light hitting the DLD, releasing thereby an electron, which is then recorded as signal. This acquisition of false signals becomes only possible if the photon energy exceeds the work function of the detector material. As the DLD consist of copper, having a work-function of 4.5 eV [155], only the UV light with 4.75 eV photon energy creates these false signals.

One problem of this "flood" of photons/electrons is the decreased sensitivity of the detector, resulting in much worse signal-to-noise ratio. For single ionization experiments, the signal strength was still good enough to perform measurements, as it was shown in the previous section. For coincidence measurements, however, the applied time window includes everything but the signal of the single ionization, which results in much more noise – as seen in figure 8.4.

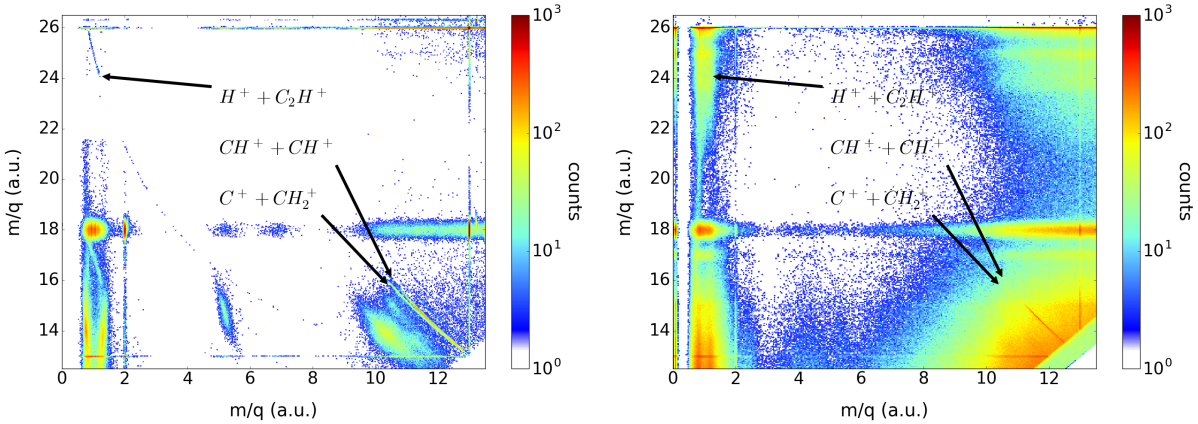

Figure 8.8: Photoion-Photoion Coincidence plot of acetylene ionized by two- and three-color fields. m/q represent the mass over charge ratio, with which the individual elements can be identified.

In figure 8.4, the recorded coincidences of acetylene are shown for ionization by $\omega/2\omega$ fields and $\omega/2\omega/3\omega$ fields, in a) and b), respectively. The ionization by the two-color field,

consisting of the fundamental and second harmonic, results in clearly visible coincidence lines of acetylene. Only the usual "false" coincidences, e.g. water with hydrogen and carbon ions (broad horizontal line at m/q of 18), are observed. The ionization of the combined three-color field, however, has many of those false coincidences, which do not result from one parent molecule. This massive background makes a reasonable investigation impossible. In order to improve the situation, different changes can be applied to the experimental setup:

1. Using different excitation wavelength, which do not release electrons in a single photon process. In the current setup, however, this is not possible as the wavelength of the third harmonic is dependent on the fundamental wavelength.

2. Eliminating the scattering points within the chamber such that no photons will reach the detector. The only possible scattering objects are: the entrance and exit window, the background and target gas, and the focusing mirror. The entrance and exit window are UV grade fused silica plates of 1 mm thickness. One can use an anti-reflex coating or place them at the Brewster angle. Both options, however, will reduce the amount of flexibility of the experimental setup. The background gas can be reduced by better vacuum conditions, but currently we already operate at $1.2 \cdot 10^{-10}$ mbar, so no big improvements can be expected. The target gas will logically be always in the chamber. The mirror is a spherical UV-enhanced aluminum mirror, which provides the best reflectivity within the UV range while still maintaining reasonable reflectivity in the visible spectrum. As the scattering cross section scales with λ^{-4} (considering only Rayleigh-scattering), using a small wavelength results in a lot of scattered light. Additional contributions from the Mie-scattering occur, due to the surface roughness, which can be close to the range of the UV-wavelengths. So in order to reduce the scattering, one has to improve the surface quality and the coating of the focusing mirror.

3. By gating the detector, one could make it sensitive only for the needed TOF and discard all other times. Gating in this context means that the detector is at a constant voltage of e.g. 2300 V and only for a special time gate it is set to 2600 V. However, due to technical reasons in the decoupling electronics, this possibility might lead to destruction of the decoupling elements such that this option was not pursued further.

As seen from the different points above, there is no easy solution to this problem. Groups working with photon energies higher than the work function of the detector usually tend to pursue point 2. In order to reduce the scattering points, a forward focusing geometry is used obsoleting the mirror within the chamber. Furthermore, the entrance and exit windows are placed far away from the interaction region, often even separated by an additional iris.

To finally enable the mentioned experiment, and for future experiments with even lower wavelength, this experimental approach is planned.

8.5 Conclusion

In this chapter, a device for the efficient generation of the second and third harmonic of a femtosecond laser field in a collinear geometry is presented. A subsequent multi-harmonic synthesizer permits to superimpose all three colors and control their relative phase as well as their intensities and polarizations. The device was tested and successfully used to investigate the interaction of $\omega/2\omega$ and $\omega/3\omega$ fields with neon atoms. For $\omega/3\omega$ fields, we observed a modulation of the ionization yield and ion momenta as a function of the relative phase between both colors. A shift of π is observed between the phase-dependent oscillations of low and high ion momenta. These trends were reproduced by semi-classical simulations based on the simple man's model. The three-color device offers sufficient flexibility for a variety of future studies on the coherent control of strong-field processes and for time-resolving ultrafast molecular dynamics.

Furthermore, the possibility of a control experiment at a conical intersection is discussed. While the measurement on the control on acetylene are still challenging, many other interesting measurements become feasible by this new setup. The here introduced three-color device permits to tailor the fields with all three colors and thereby to extend recent studies, which use orthogonally polarized [131] or counter-rotating circularly polarized $\omega/2\omega$ fields [132, 156], to more complex fields. Another application of the three-color setup are pump-probe experiments, where e.g. the ultraviolet pulse is used for exciting the target and single or multiple color laser fields are used to control and probe the unfolding dynamics. This is particularly interesting in studies on the strong-field control of molecular reactions.

9 Conclusion and Outlook

For more than a decade it has been known that electronic motion in atoms and molecules can be controlled by the carrier-envelope phase of an ultrashort laser pulse [20]. More recently, a study demonstrated that also the nuclear motion can be influenced by the CEP [6]. This control, however, was mainly limited to the directional dissociation of CH-bonds [7].

In this thesis, the CEP-control was extended to the more complex molecular reaction of isomerization – a structural rearrangement of the molecule via hydrogen migration. It was shown that an ultrashort laser pulse can steer the directionality of the isomerization in small hydrocarbons, i.e. acetylene and allene. The intensity- and the CEP-dependence of both molecules was probed, revealing that the ionization process predetermines the strength of the CEP-control. For low intensities, the non-sequential double-ionization introduces a CEP-dependence of the molecular reaction, while for higher intensities the sequential double-ionization suppresses CEP-control.

With the gained knowledge on how to control the molecular reactions, studies on the temporal evolution of the molecular structure were performed by few-cycle pump-probe experiments in acetylene. A very high temporal resolution of 5 fs could be achieved such that the vibrational motion of the CC- and CH-bonds in acetylene became directly observable. The experimentally retrieved vibrational periods of ∼11 fs and ∼20 fs coincide well with the theoretical predictions of the CH- and CC-bond of the dication state. In additional measurements, a vibrational motion with a period of ∼25 fs was detected, which survived several hundreds of femtoseconds, indicating a strong CC-bond vibration in the cation. By the investigation of the temporal evolution of the CCH-angles, the isomerization process was visualized in "real" time, revealing an isomerization time of ∼54 fs, which agrees well with previous experimental studies [11, 89, 93] and theoretical predictions [92]. In particular, the dissociation channel $C_2H_2^{3+} \rightarrow H^+ + H^+ + CC^+$ provided complementary information about the isomerization process compared to the previously investigated channel $C_2H_2^{3+} \rightarrow H^+ + C^+ + CH^+$. Exploring the kinetic energies of all particles involved in the process revealed the importance of the intermediate transition states t-TS1' and t-TS1" for the temporal evolution of the molecule.

Within the same study, an enhanced ionization was measured in few-cycle pump-probe measurements in several dissociation channels of acetylene. The pump pulse excited the molecule into the dication state, where a dissociation was initiated. Once the inter-nuclear

bond length reached the critical distance (around twice the equilibrium bond length), the ionization was enhanced due to easier tunneling through the inner barrier, see 7.3.1. The EI signal in the four-fold Coulomb explosion channel $C_2H_2^{4+} \rightarrow H^+ + H^+ + C^+ + C^+$ is in good agreement with previous measurements performed in diatomic systems [63, 109–111]. This implies that also in a polyatomic molecule like acetylene mainly a single bond is dissociated, which leads to enhanced ionization, while all other bonds stay intact. By the comparison to the three-fold coincidence channels, it could be concluded that mainly the CH-bond is stretched, which leads to the enhanced ionization signal in acetylene.

In the last part of this thesis, a setup to shape multi-color laser-fields was developed, consisting of a part to efficiently generate the second and third harmonic with a subsequent field synthesizer. In first experiments, the technical possibilities were explored, showing its applicability for the investigation of molecular processes. Especially the resonant molecular excitation in the UV can be employed to efficiently ionize molecules as the conversion efficiency into the UV reaches more than 10 %.

In the future, the interpretation of experimental data could be facilitated if the molecules would be excited into specific charged states. For this purpose, the shown multi-color synthesizer could be employed to selectively create one harmonic within a high-harmonic scheme (see [137]). Using such selective wavelengths would solve the ambiguity in strong-field excitations, which usually results in an undesired superposition of excited states. Another exciting possibility is the control over molecular reactions at conical intersections of the potential energy surfaces. For this purpose, the molecule has first to be excited by a pump pulse, e.g. by the third harmonic. After propagation on the potential energy surface, the wave-packet reaches the conical intersection, where a second pulse, e.g. a combination of the fundamental and the second harmonic, allows to control the directionality of the wave-packet. Thereby, the control over molecular reactions, such as isomerization, can be increased.

With the developed techniques, studies on molecular reactions could also be performed on larger molecules which are more relevant for medical/pharmaceutical applications. Hereby, the possibility to interact with selective bonds is of special interest as the classical chemistry applies often only to the weakest bonds if no further catalysts are used. In particular the light-induced control over chirality is a very interesting field as it opens new possibilities of creating isomers with different chemical and medical properties. The here-shown field synthesizer could serve as an appropriate tool for the control of such reactions.

Bibliography

[1] M. Shapiro and P. Brumer, *Quantum Control of Molecular Processes, Second Edition* (Wiley-VCH, 2012).

[2] A. Rudenko, B. Feuerstein, K. Zrost, V. L. B. de Jesus, T. Ergler, C. Dimopoulou, C. D. Schroter, R. Moshammer, and J. Ullrich, "Fragmentation dynamics of molecular hydrogen in strong ultrashort laser pulses", J. Phys. B-Atomic Mol. Opt. Phys. **38**, 487–501 (2005).

[3] J. Heicklen, J. Desai, A. Bahta, C. Harper, and R. Simonaitis, "The temperature and wavelength dependence of the photo-oxidation of propionaldehyde", J. Photochem. **34**, 117–135 (1986).

[4] M. Kübel, C. Burger, R. Siemering, N. G. Kling, B. Bergues, A. S. Alnaser, I. Ben-Itzhak, R. Moshammer, R. de Vivie-Riedle, and M. F. Kling, "Phase- and intensity-dependence of ultrafast dynamics in hydrocarbon molecules in few-cycle laser fields", Mol. Phys. **115**, 1835–1845 (2017).

[5] M. Kübel, R. Siemering, C. Burger, N. G. Kling, H. Li, A. S. Alnaser, B. Bergues, S. Zherebtsov, A. M. Azzeer, I. Ben-Itzhak, R. Moshammer, R. de Vivie-Riedle, and M. F. Kling, "Steering Proton Migration in Hydrocarbons Using Intense Few-Cycle Laser Fields", Phys. Rev. Lett. **116**, 193001 (2016).

[6] A. S. Alnaser, M. Kübel, R. Siemering, B. Bergues, N. G. Kling, K. J. Betsch, Y. Deng, J. Schmidt, Z. A. Alahmed, A. M. Azzeer, J. Ullrich, I. Ben-Itzhak, R. Moshammer, U. Kleineberg, F. Krausz, R. de Vivie-Riedle, and M. F. Kling, "Subfemtosecond steering of hydrocarbon deprotonation through superposition of vibrational modes", Nat. Commun. **5**, 3800 (2014).

[7] H. Li, N. G. Kling, B. Förg, J. Stierle, A. Kessel, S. A. Trushin, M. F. Kling, and S. Kaziannis, "Carrier-envelope phase dependence of the directional fragmentation and hydrogen migration in toluene in few-cycle laser fields", Struct. Dyn. **3**, 043206 (2016).

[8] G. Van der Rest, P. Mourgues, J. Tortajada, and H. Audier, "Gas phase catalyzed keto-enol isomerization of cations by proton transport", Int. J. Mass Spectrom. **179-180**, 293–300 (1998).

[9] G. Van Der Rest, H. Nedev, J. Chamot-Rooke, P. Mourgues, T. B. McMahon, and H. E. Audier, "'Proton-transport' catalysis in the gas phase. Keto-enol isomerization of ionized acetaldehyde", Int. J. Mass Spectrom. **202**, 161–174 (2000).

[10] J. Chamot-Rooke, G. Van Der Rest, P. Mourgues, and H. E. Audier, "Two different pathways for unimolecular and for catalyzed keto-enol isomerization of ionized acetophenone", Int. J. Mass Spectrom. **195-196**, 385–392 (2000).

[11] T. Osipov, C. L. Cocke, M. H. Prior, A. Landers, T. Weber, O. Jagutzki, L. Schmidt, H. Schmidt-Böcking, and R. Dörner, "Photoelectron-Photoion Momentum Spectroscopy as a Clock for Chemical Rearrangements: Isomerization of the Di-Cation of Acetylene to the Vinylidene Configuration", Phys. Rev. Lett. **90**, 233002 (2003).

[12] H. Xu, T. Okino, and K. Yamanouchi, "Ultrafast hydrogen migration in allene in intense laser fields: Evidence of two-body Coulomb explosion", Chem. Phys. Lett. **469**, 255–260 (2009).

[13] T. Okino, A. Watanabe, H. Xu, and K. Yamanouchi, "Double Proton Migration and Proton/Deuteron Exchange in Methylacetylene in Intense Laser Fields", in "Multiphot. Process. Attosecond Phys.", (Springer, Berlin, Heidelberg, 2012), pp. 335–340.

[14] T. Okino, A. Watanabe, H. Xu, and K. Yamanouchi, "Ultrafast hydrogen scrambling in methylacetylene and methyl-d3-acetylene ions induced by intense laser fields", Phys. Chem. Chem. Phys. **14**, 10640 (2012).

[15] B. R. Heazlewood, A. T. Maccarone, D. U. Andrews, D. L. Osborn, L. B. Harding, S. J. Klippenstein, M. J. T. Jordan, and S. H. Kable, "Near-threshold H/D exchange in CD_3CHO photodissociation", Nat. Chem. **3**, 443–448 (2011).

[16] O. Ghafur, W. Siu, P. Johnsson, M. F. Kling, M. Drescher, and M. J. J. Vrakking, "A velocity map imaging detector with an integrated gas injection system", Rev. Sci. Instrum. **80**, 033110 (2009).

[17] J. Ullrich, R. Moshammer, A. Dorn, R. Dörner, L. P. H. Schmidt, and H. Schmidt-Böcking, "Recoil-ion and electron momentum spectroscopy: reaction-microscopes", Reports Prog. Phys. **66**, 1463–1545 (2003).

[18] F. Krausz and M. Ivanov, "Attosecond physics", Rev. Mod. Phys. **81**, 163–234 (2009).

[19] A. Baltuška, T. Udem, M. Uiberacker, M. Hentschel, E. Goulielmakis, C. Gohle, R. Holzwarth, V. S. Yakovlev, A. Scrinzi, T. W. Hänsch, and F. Krausz, "Attosecond control of electronic processes by intense light fields", Nature **421**, 611–615 (2003).

[20] M. F. Kling, C. Siedschlag, A. J. Verhoef, J. I. Khan, M. Schultze, T. Uphues, Y. Ni, M. Uiberacker, M. Drescher, F. Krausz, and M. J. J. Vrakking, "Control of Electron Localization in Molecular Dissociation", Science **312**, 246–248 (2006).

[21] I. H. Malitson, "Interspecimen Comparison of the Refractive Index of Fused Silica", J. Opt. Soc. Am. **55**, 1205–1209 (1965).

[22] T. M. Kardaś, M. Nejbauer, P. Wnuk, B. Resan, C. Radzewicz, and P. Wasylczyk, "Full 3D modelling of pulse propagation enables efficient nonlinear frequency conversion with low energy laser pulses in a single-element tripler", Sci. Rep. **7**, 42889 (2017).

[23] C. Burger, W. F. Frisch, T. M. Kardaś, M. Trubetskov, V. Pervak, R. Moshammer, B. Bergues, M. F. Kling, and P. Wnuk, "Compact and flexible harmonic generator and three-color synthesizer for femtosecond coherent control and time-resolved studies", Opt. Express **25**, 31130–31139 (2017).

[24] L. V. Keldysh, "Ionization in the field of a strong electromagnetic wave", Sov. Phys. JETP **20**, 1307–1314 (1965).

[25] P. B. Corkum, "Plasma perspective on strong field multiphoton ionization", Phys. Rev. Lett. **71**, 1994–1997 (1993).

[26] K. C. Kulander, K. J. Schafer, and J. L. Krause, *Dynamics of Short-Pulse Excitation, Ionization and Harmonic Conversion* (Springer US, Boston, MA, 1993), pp. 95–110.

[27] T. Brabec and F. Krausz, "Intense few-cycle laser fields: Frontiers of nonlinear optics", Rev. Mod. Phys. **72**, 545–591 (2000).

[28] M. Hentschel, R. Kienberger, C. Spielmann, G. A. Reider, N. Milosevic, T. Brabec, P. Corkum, U. Heinzmann, M. Drescher, and F. Krausz, "Attosecond metrology", Nature **414**, 509–513 (2001).

[29] G. G. Paulus, W. Nicklich, H. Xu, P. Lambropoulos, and H. Walther, "Plateau in Above Threshold Spectra", Phys. Rev. Lett. **72**, 2851–2854 (1994).

[30] M. Busuladžić, A. Gazibegović-Busuladžić, and D. B. Milošević, "High-order above-threshold ionization in a laser field: Influence of the ionization potential on the high-energy cutoff", Laser Phys. **16**, 289–293 (2006).

[31] Y. Huismans, A. Rouzée, A. Gijsbertsen, J. H. Jungmann, a. S. Smolkowska, P. S. W. M. Logman, F. Lépine, C. Cauchy, S. Zamith, T. Marchenko, J. M. Bakker, G. Berden, B. Redlich, a. F. G. van der Meer, H. G. Muller, W. Vermin, K. J. Schafer, M. Spanner, M. Y. Ivanov, O. Smirnova, D. Bauer, S. V. Popruzhenko, and M. J. J. Vrakking, "Time-Resolved Holography", Science **331**, 61–64 (2011).

[32] B. Walker, B. Sheehy, L. F. DiMauro, P. A. Agostini, K. J. Schafer, and K. C. Kulander, "Precision Measurement of Strong Field Double Ionization of Helium", (1994).

[33] P. B. Corkum, N. H. Burnett, and F. Brunel, "Above-Threshold Ionization in the Long-Wavelength Limit", Phys. Rev. Lett. **62**, 1259–1262 (1989).

[34] W. F. Frisch, "Multi Colour Control of Strong Field Ionisation", thesis, Ludwig-Maximilians-Universität München (2017).

[35] X. M. Tong and C. D. Lin, "Empirical formula for static field ionization rates of atoms and molecules by lasers in the barrier-suppression regime", J. Phys. B At. Mol. Opt. Phys. **38**, 2593–2600 (2005).

[36] M. V. Ammosov, N. B. Delone, and V. P. Krainov, "Tunnel ionization of complex atoms and of atomic ions in an alternating electromagnetic field", Sov. Phys. JETP **64**, 1191–1194 (1986).

[37] M. Kowalewski, K. Bennett, K. E. Dorfman, and S. Mukamel, "Catching Conical Intersections in the Act: Monitoring Transient Electronic Coherences by Attosecond Stimulated X-Ray Raman Signals", Phys. Rev. Lett. **115**, 193003 (2015).

[38] H. Ibrahim, B. Wales, S. Beaulieu, B. E. Schmidt, N. Thiré, E. P. Fowe, É. Bisson, C. T. Hebeisen, V. Wanie, M. Giguére, J.-C. Kieffer, M. Spanner, A. D. Bandrauk, J. Sanderson, M. S. Schuurman, and F. Légaré, "Tabletop imaging of structural evolutions in chemical reactions demonstrated for the acetylene cation", Nat. Commun. **5**, 4422 (2014).

[39] S. Koke, C. Grebing, H. Frei, A. Anderson, A. Assion, and G. Steinmeyer, "Direct frequency comb synthesis with arbitrary offset and shot-noise-limited phase noise", Nat. Photonics **4**, 462–465 (2010).

[40] F. Lücking, V. Crozatier, N. Forget, A. Assion, and F. Krausz, "Approaching the limits of carrier-envelope phase stability in a millijoule-class amplifier", Opt. Lett. **39**, 3884–7 (2014).

[41] F. Lücking, A. Assion, A. Apolonski, F. Krausz, and G. Steinmeyer, "Long-term carrier-envelope-phase-stable few-cycle pulses by use of the feed-forward method", Opt. Lett. **37**, 2076–2078 (2012).

[42] H. Telle, G. Steinmeyer, A. Dunlop, J. Stenger, D. Sutter, and U. Keller, "Carrier-envelope offset phase control: A novel concept for absolute optical frequency measurement and ultrashort pulse generation", Appl. Phys. B **69**, 327–332 (1999).

[43] V. Pervak, I. Ahmad, S. a. Trushin, Z. Major, A. Apolonski, S. Karsch, and F. Krausz, "Chirped-pulse amplification of laser pulses with dispersive mirrors", Opt. Express **17**, 19204–12 (2009).

[44] D. J. Kane and R. Trebino, "Characterization of Arbitrary Femtosecond Pulses Using Frequency-Resolved Optical Gating", IEEE J. Quantum Electron. **29**, 571–579 (1993).

[45] M. Schultze, A. Wirth, I. Grguras, M. Uiberacker, T. Uphues, A. Verhoef, J. Gagnon, M. Hofstetter, U. Kleineberg, E. Goulielmakis, and F. Krausz, "State-of-the-art attosecond metrology", J. Electron Spectros. Relat. Phenomena **184**, 68–77 (2011).

[46] T. Wittmann, B. Horvath, W. Helml, M. G. Schätzel, X. Gu, a. L. Cavalieri, G. G. Paulus, and R. Kienberger, "Single-shot carrier-envelope phase measurement of few-cycle laser pulses", Nat. Phys. **5**, 357–362 (2009).

[47] A. M. Sayler, T. Rathje, W. Müller, K. Rühle, R. Kienberger, and G. G. Paulus, "Precise, real-time, every-single-shot, carrier-envelope phase measurement of ultrashort laser pulses", Opt. Lett. **36**, 16–18 (2011).

[48] G. G. Paulus, F. Grasbon, H. Walther, P. Villoresi, M. Nisoli, S. Stagira, E. Priori, and S. De Silvestri, "Absolute-phase phenomena in photoionization with few-cycle laser pulses", Nature **414**, 2000–2002 (2001).

[49] G. G. Paulus, F. Lindner, H. Walther, A. Baltuška, E. Goulielmakis, M. Lezius, and F. Krausz, "Measurement of the Phase of Few-Cycle Laser Pulses", Phys. Rev. Lett. **91**, 253004 (2003).

[50] T. Rathje, N. G. Johnson, M. Möller, F. Süßmann, D. Adolph, M. Kübel, R. Kienberger, M. F. Kling, G. G. Paulus, and a. M. Sayler, "Review of attosecond resolved measurement and control via carrierenvelope phase tagging with above-threshold ionization", J. Phys. B At. Mol. Opt. Phys. **45**, 074003 (2012).

[51] M. Kübel, K. J. Betsch, N. G. Johnson, U. Kleineberg, R. Moshammer, J. Ullrich, G. G. Paulus, M. F. Kling, and B. Bergues, "Carrier-envelope-phase tagging in measurements with long acquisition times", New J. Phys. **14**, 093027 (2012).

[52] M. Takeda, H. Ina, and S. Kobayashi, "Fourier-transform method of fringe-pattern analysis for computer-based topography and interferometry", J. Opt. Soc. Am. **72**, 156 (1982).

[53] A. Wirth, M. T. Hassan, I. Grguras, J. Gagnon, A. Moulet, T. T. Luu, S. Pabst, R. Santra, Z. a. Alahmed, a. M. Azzeer, V. S. Yakovlev, V. Pervak, F. Krausz, and E. Goulielmakis, "Synthesized Light Transients", Science **334**, 195–200 (2011).

[54] M. T. Hassan, A. Wirth, I. Grguraš, A. Moulet, T. T. Luu, J. Gagnon, and V. Pervak, "Invited Article: Attosecond photonics: Synthesis and control of light transients", Rev. Sci. Instrum. **83**, 111301 (2012).

[55] T. Fuji, T. Horio, and T. Suzuki, "Generation of 12 fs deep-ultraviolet pulses by four-wave mixing through filamentation in neon gas", Opt. Lett. **32**, 2481–2483 (2007).

[56] O. Jagutzki, L. Spielberger, R. Dörner, S. Nüttgens, V. Mergel, H. Schmidt-Böcking, J. Ullrich, R. E. Olson, and U. Buck, "Recoil-ion momentum distribution for He(e,2e)He^+ - and He(e,3e)He^{++}-reactions", Zeitschrift für Phys. D **36**, 5–10 (1996).

[57] V. Mergel, R. Dörner, J. Ullrich, O. Jagutzki, S. Lencinas, S. Nüttgens, L. Spielberger, M. Unverzagt, C. L. Cocke, R. E. Olson, M. Schulz, U. Buck, E. Zanger, W. Theisinger, M. Isser, S. Geis, and H. Schmidt-Böcking, "State Selective Scattering Angle Dependent Capture Cross Sections Measured by Cold Target Recoil Ion Momentum Spectroscopy", Phys. Rev. Lett. **74**, 2200–2203 (1995).

[58] R. Moshammer, Y. H. Jiang, L. Foucar, A. Rudenko, T. Ergler, C. D. Schröter, S. Lüdemann, K. Zrost, D. Fischer, J. Titze, T. Jahnke, M. Schöffler, T. Weber, R. Dörner, T. J. M. Zouros, A. Dorn, T. Ferger, K. U. Kühnel, S. Düsterer, R. Treusch, P. Radcliffe, E. Plönjes, and J. Ullrich, "Few-Photon Multiple Ionization of Ne and Ar by Strong Free-Electron-Laser Pulses", Phys. Rev. Lett. **98**, 203001 (2007).

[59] O. Jagutzki, A. Cerezo, A. Czasch, R. Dörner, M. Hattaß, M. Huang, V. Mergel, U. Spillmann, K. Ullmann-pfleger, T. Weber, H. Schmidt-Böcking, and G. D. W. Smith, "Multiple Hit Readout of a Microchannel Plate Detector With a Three-Layer Delay-Line Anode", IEEE Trans. Nucl. Sci. **49**, 2477–2483 (2002).

[60] O. Jagutzki, V. Mergel, K. Ullmann-Pfleger, L. Spielberger, U. Spillmann, R. Dörner, and H. Schmidt-Böcking, "A broad-application microchannel-plate detector system for advanced particle or photon detection tasks: large area imaging, precise multi-hit timing information and high detection rate", Nucl. Instruments Methods Phys. Res. A **477**, 244–249 (2002).

[61] R. S. Slepnev, A. A. Bezbakh, M. S. Golovkov, A. V. Gorshkov, V. A. Gorshkov, A. V. Daniel, G. Kaminski, S. A. Krupko, A. S. Martianov, S. I. Sidorchuk, V. Chudoba, and A. S. Fomichev, "VME-based data acquisition system for multiparameter measurements", Instruments Exp. Tech. **55**, 645–650 (2012).

[62] J. Adamczewski, M. Al-Turany, D. Bertini, H. G. Essel, M. Hemberger, N. Kurz, and M. Richter, "Go4 multitasking class library with ROOT", IEEE Trans. Nucl. Sci. **49**, 521–524 (2002).

[63] A. S. Alnaser, I. Litvinyuk, T. Osipov, B. Ulrich, A. Landers, E. Wells, C. M. Maharjan, P. Ranitovic, I. Bochareva, D. Ray, and C. L. Cocke, "Momentum-imaging investigations of the dissociation of D_2^+ and the isomerization of acetylene to vinylidene by intense short laser pulses", J. Phys. B At. Mol. Opt. Phys. **39**, 485–492 (2006).

[64] C. Uiberacker and J. Werner, "Molecular isomerization induced by ultrashort infrared pulses. II. Pump-dump isomerization using pairs of time-delayed half-cycle pulses", J. Chem. Phys. **120**, 11540–11548 (2004).

[65] M. E. A. Madjet, O. Vendrell, and R. Santra, "Ultrafast dynamics of photoionized acetylene", Phys. Rev. Lett. **107**, 263002 (2011).

[66] M. E. A. Madjet, Z. Li, and O. Vendrell, "Ultrafast hydrogen migration in acetylene cation driven by non-adiabatic effects", J. Chem. Phys. **138** (2013).

[67] X. Xie, S. Roither, M. Schöffler, E. Lötstedt, D. Kartashov, L. Zhang, G. G. Paulus, A. Iwasaki, A. Baltuška, K. Yamanouchi, and M. Kitzler, "Electronic predetermination of ethylene fragmentation dynamics", Phys. Rev. X **4**, 1–10 (2014).

[68] X. Xie, K. Doblhoff-Dier, S. Roither, M. S. Schöffler, D. Kartashov, H. Xu, T. Rathje, G. G. Paulus, A. Baltuška, S. Gräfe, and M. Kitzler, "Attosecond-recollision-controlled selective fragmentation of polyatomic molecules", Phys. Rev. Lett. **109**, 243001 (2012).

[69] S. Kaziannis, N. Kotsina, and C. Kosmidis, "Interaction of toluene with two-color asymmetric laser fields: Controlling the directional emission of molecular hydrogen fragments", J. Chem. Phys. **141** (2014).

[70] N. Kotsina, S. Kaziannis, and C. Kosmidis, "Hydrogen migration in methanol studied under asymmetric fs laser irradiation", Chem. Phys. Lett. **604**, 27–32 (2014).

[71] R. A. Siemering, "Light-matter interactions: From ionization to the control of nuclear and electron dynamics", Ph.D. thesis, Ludwig-Maximilians-Universität München (2017).

[72] M. F. Kling, P. von den Hoff, I. Znakovskaya, and R. de Vivie-Riedle, "(Sub-) femtosecond control of molecular reactions via tailoring the electric field of light", Phys. Chem. Chem. Phys. **15**, 9448–67 (2013).

[73] X. Gong, Q. Song, Q. Ji, H. Pan, J. Ding, J. Wu, and H. Zeng, "Strong-field dissociative double ionization of acetylene", Phys. Rev. Lett. **112**, 1–5 (2014).

[74] M. Kübel, N. G. Kling, K. J. Betsch, N. Camus, A. Kaldun, U. Kleineberg, I. Ben-Itzhak, R. R. Jones, G. G. Paulus, T. Pfeifer, J. Ullrich, R. Moshammer, M. F. Kling, and B. Bergues, "Nonsequential double ionization of N_2 in a near-single-cycle laser pulse", Phys. Rev. A **88**, 023418 (2013).

[75] M. Kübel, C. Burger, N. G. Kling, T. Pischke, L. Beaufore, I. Ben-Itzhak, G. G. Paulus, J. Ullrich, T. Pfeifer, R. Moshammer, M. F. Kling, and B. Bergues, "Complete characterization of single-cycle double ionization of argon from the nonsequential to the sequential ionization regime", Phys. Rev. A **93**, 053422 (2016).

[76] M. Kübel, "Single-Cycle Non-Sequential Double Ionization", Ph.D. thesis, Ludwig-Maximilians-Universität München (2014).

[77] V. Roudnev and B. D. Esry, "General Theory of Carrier-Envelope Phase Effects", Phys. Rev. Lett. **99**, 220406 (2007).

[78] S. Skruszewicz, J. Tiggesbäumker, K. H. Meiwes-Broer, M. Arbeiter, T. Fennel, and D. Bauer, "Two-Color Strong-Field Photoelectron Spectroscopy and the Phase of the Phase", Phys. Rev. Lett. **115**, 043001 (2015).

[79] K. Doblhoff-Dier, M. Kitzler, and S. Gräfe, "Theoretical investigation of alignment-dependent intense-field fragmentation of acetylene", Phys. Rev. A **94**, 013405 (2016).

[80] J. Collin and F. P. Lossing, "Ionization and Dissociation of Aliene, Propyne, 1-Butyne, and 1,2- and 1,3-Butadienes by Electron Impact; the $C_3H_3^+$ Ion", J. Am. Chem. Soc. **79**, 5848–5853 (1957).

[81] F. Hopfgarten and R. Manne, "Molecular orbital interpretation of X-ray emission and photoelectron spectra", J. Chem. Phys. **52**, 5733–5739 (1970).

[82] J. Levin, H. Feldman, A. Baer, D. Ben-Hamu, O. Heber, D. Zajfman, and Z. Vager, "Study of Unimolecular Reactions by Coulomb Explosion Imaging: The Nondecaying Vinylidene", Phys. Rev. Lett. **81**, 3347–3350 (1998).

[83] H. Stapelfeldt, E. Constant, H. Sakai, and P. Corkum, "Time-resolved Coulomb explosion imaging: A method to measure structure and dynamics of molecular nuclear wave packets", Phys. Rev. A **58**, 426–433 (1998).

[84] A. Hishikawa, A. Matsuda, M. Fushitani, and E. J. Takahashi, "Visualizing recurrently migrating hydrogen in acetylene dication by intense ultrashort laser pulses", Phys. Rev. Lett. **99**, 258302 (2007).

[85] A. Hishikawa, A. Matsuda, E. J. Takahashi, and M. Fushitani, "Acetylene-vinylidene isomerization in ultrashort intense laser fields studied by triple ion-coincidence momentum imaging", J. Chem. Phys. **128**, 084302 (2008).

[86] A. Matsuda, M. Fushitani, E. J. Takahashi, and A. Hishikawa, "Visualizing correlated dynamics of hydrogen atoms in acetylene dication by time-resolved four-body coulomb explosion imaging", Springer Proc. Phys. **125**, 317–322 (2012).

[87] C. Burger, N. G. Kling, R. Siemering, A. S. Alnaser, B. Bergues, A. M. Azzeer, R. Moshammer, R. de Vivie-Riedle, M. Kübel, and M. Kling, "Visualization of bond rearrangements in acetylene using near single-cycle laser pulses", Faraday Discuss. **194**, 495–508 (2016).

[88] H. Werner, P. J. Knowles, G. Knizia, F. R. Manby, M. Schütz, P. Celani, W. Györffy, D. Kats, T. Korona, R. Lindh, A. Mitrushenkov, G. Rauhut, K. R. Shamasundar, T. B. Adler, R. D. Amos, A. Bernhardsson, A. Berning, D. L. Cooper, M. J. O. Deegan, A. J. Dobbyn, F. Eckert, E. Goll, C. Hampel, A. Hesselmann, G. Hetzer, T. Hrenar, G. Jansen, C. Köppl, Y. Liu, A. W. Lloyd, R. A. Mata, A. J. May, S. J. McNicholas, W. Meyer, M. E. Mura, A. Nicklass, D. P. O'Neill, P. Palmieri, D. Peng, K. Pflüger, R. Pitzer, M. Reiher, T. Shiozaki, H. Stoll, A. J. Stone, R. Tarroni, T. Thorsteinsson, and M. Wang, "MOLPRO, version 2006.1, a package of ab initio programs", (2006).

[89] Y. H. Jiang, A. Rudenko, O. Herrwerth, L. Foucar, M. Kurka, K. U. Kühnel, M. Lezius, M. F. Kling, J. Van Tilborg, A. Belkacem, K. Ueda, S. Düsterer, R. Treusch, C. D. Schröter, R. Moshammer, and J. Ullrich, "Ultrafast extreme ultraviolet induced isomerization of acetylene cations", Phys. Rev. Lett. **105**, 263002 (2010).

[90] C. E. Liekhus-Schmaltz, I. Tenney, T. Osipov, A. Sanchez-Gonzalez, N. Berrah, R. Boll, C. Bomme, C. Bostedt, J. D. Bozek, S. Carron, R. Coffee, J. Devin, B. Erk, K. R. Ferguson, R. W. Field, L. Foucar, L. J. Frasinski, J. M. Glownia, M. Gühr, A. Kamalov, J. Krzywinski, H. Li, J. P. Marangos, T. J. Martinez, B. K. McFarland, S. Miyabe, B. Murphy, A. Natan, D. Rolles, A. Rudenko, M. Siano, E. R. Simpson, L. Spector, M. Swiggers, D. Walke, S. Wang, T. Weber, P. H. Bucksbaum, and V. S. Petrovic, "Ultrafast isomerization initiated by X-ray core ionization", Nat. Commun. **6**, 1–7 (2015).

[91] Y. H. Jiang, A. Senftleben, M. Kurka, A. Rudenko, L. Foucar, O. Herrwerth, M. F. Kling, M. Lezius, J. V. Tilborg, A. Belkacem, K. Ueda, D. Rolles, R. Treusch, Y. Z. Zhang, Y. F. Liu, C. D. Schröter, J. Ullrich, and R. Moshammer, "Ultrafast dynamics in acetylene clocked in a femtosecond XUV stopwatch", J. Phys. B At. Mol. Opt. Phys. **46**, 164027 (2013).

[92] T. S. Zyubina, Y. A. Dyakov, S. H. Lin, A. D. Bandrauk, and A. M. Mebel, "Theoretical study of isomerization and dissociation of acetylene dication in the ground and excited electronic states", J. Chem. Phys. **123**, 134320 (2005).

[93] Y. H. Jiang, A. Senftleben, A. Rudenko, M. E. Madjet, O. Vendrell, M. Kurka, K. Schnorr, L. Foucar, M. Kübel, O. Herrwerth, M. Lezius, M. F. Kling, J. Van Tilborg, A. Belkacem, K. Ueda, S. Düsterer, R. Treusch, C. D. Schröter, R. Santra, J. Ullrich, and R. Moshammer, "Watching the acetylene-vinylidene intramolecular reaction in real time", arxiv pp. 1–21 (2010).

[94] H.-J. Werner, P. J. Knowles, G. Knizia, F. R. Manby, and M. Schütz, "Molpro: a general-purpose quantum chemistry program package", Wiley Interdiscip. Rev. Comput. Mol. Sci. **2**, 242–253 (2012).

[95] H. Li, N. G. Kling, T. Gaumnitz, C. Burger, R. Siemering, J. Schötz, Q. Liu, L. Ban, Y. Pertot, J. Wu, A. M. Azzeer, R. de Vivie-Riedle, H. Wörner, and M. F. Kling, "Sub-cycle steering of the deprotonation of acetylene by intense few-cycle mid-infrared laser fields", Opt. Express **25**, 14192–14203 (2017).

[96] B. Roos, P. R. Taylor, and P. E. M. Siegbahn, "A complete active space SCF method (CASSCF) using a density matrix formuulated super-CI approach", Chem. Phys. **48**, 157–173 (1980).

[97] W. J. Hehre, R. Ditchfield, and J. A. Pople, "Self-Consistent Molecular Orbital Methods. XII. Further Extensions of Gaussian-Type Basis Sets for Use in Molecular Orbital Studies of Organic Molecules", J. Chem. Phys. **56**, 2257–2261 (1972).

[98] P. C. Hariharan and J. A. Pople, "The Influence of Polarization Functions on Molecular Orbital Hydrogenation Energies", Theor. Chim. Acta **28**, 213–222 (1973).

[99] M. M. Francl, W. J. Pietro, W. J. Hehre, S. J. Binkley, M. S. Gordon, D. J. DeFrees, and J. A. Pople, "Self-consistent molecular orbital methods. XXIII. A polarization-type basis set for second-row elements", J. Chem. Phys. **77**, 3654–3665 (1982).

[100] M. Barbatti, G. Granucci, M. Ruckenbauer, F. Plasser, R. Crespo-Otero, J. Pittner, M. Persico, and H. Lischka, "NEWTON-X: a package for Newtonian dynamics close to the crossing seam", (2014).

[101] M. Barbatti, M. Ruckenbauer, F. Plasser, J. Pittner, G. Granucci, M. Persico, and H. Lischka, "Newton-X: A surface-hopping program for nonadiabatic molecular dynamics", Wiley Interdiscip. Rev. Comput. Mol. Sci. **4**, 26–33 (2014).

[102] B. P. Fingerhut, S. Oesterling, K. Haiser, K. Heil, A. Glas, W. J. Schreier, W. Zinth, T. Carell, and R. de Vivie-Riedle, "ONIOM approach for non-adiabatic on-the-fly molecular dynamics demonstrated for the backbone controlled Dewar valence isomerization", J. Chem. Phys. **136**, 204307 (2012).

[103] P. von den Hoff, I. Znakovskaya, S. Zherebtsov, M. F. Kling, and R. de Vivie-Riedle, "Effects of multi orbital contributions in the angular-dependent ionization of molecules in intense few-cycle laser pulses", Appl. Phys. B Lasers Opt. **98**, 659–666 (2010).

[104] D. Ray, F. He, W. Cao, H. Mashiko, P. Ranitovic, K. P. Singh, I. Znakovskaya, U. Thumm, G. G. Paulus, M. F. Kling, I. V. Litvinyuk, and C. L. Cocke, "Ion-Energy Dependence of Asymmetric Dissociation of D_2 by a Two-Color Laser Field", Phys. Rev. Lett. **103**, 223201 (2009).

[105] T. Ergler, A. Rudenko, B. Feuerstein, K. Zrost, C. D. Schröter, R. Moshammer, and J. Ullrich, "Spatiotemporal Imaging of Ultrafast Molecular Motion: Collapse and Revival of the D_2^+ Nuclear Wave Packet", Phys. Rev. Lett. **97**, 193001 (2006).

[106] H. Niikura, D. M. Villeneuve, and P. B. Corkum, "Controlling vibrational wave packets with intense, few-cycle laser pulses", Phys. Rev. A - At. Mol. Opt. Phys. **73**, 21402 (2006).

[107] J. Wu, M. Meckel, L. Schmidt, M. Kunitski, S. Voss, H. Sann, H. Kim, T. Jahnke, A. Czasch, and R. Dörner, "Probing the tunnelling site of electrons in strong field enhanced ionization of molecules", Nat. Commun. **3**, 1113 (2012).

[108] T. Zuo and A. D. Bandrauk, "Charge-resonance-enhanced ionization of diatomic molecular ions by intense lasers", Phys. Rev. A **52**, 2511–2514 (1995).

[109] T. Ergler, A. Rudenko, B. Feuerstein, K. Zrost, C. D. Schröter, R. Moshammer, and J. Ullrich, "Time-Resolved Imaging and Manipulation of H_2 Fragmentation in Intense Laser Fields", Phys. Rev. Lett. **95**, 93001 (2005).

[110] I. Ben-Itzhak, P. Q. Wang, A. M. Sayler, K. D. Carnes, M. Leonard, B. D. Esry, A. S. Alnaser, B. Ulrich, X. M. Tong, I. V. Litvinyuk, C. M. Maharjan, P. Ranitovic, T. Osipov, S. Ghimire, Z. Chang, and C. L. Cocke, "Elusive enhanced ionization structure for H_2^+ in intense ultrashort laser pulses", Phys. Rev. A **78**, 063419 (2008).

[111] H. Xu, F. He, D. Kielpinski, R. Sang, and I. Litvinyuk, "Experimental observation of the elusive double-peak structure in R-dependent strong-field ionization rate of H_2^+", Sci. Rep. **5**, 13527 (2015).

[112] I. A. Bocharova, A. S. Alnaser, U. Thumm, T. Niederhausen, D. Ray, C. L. Cocke, and I. V. Litvinyuk, "Time-resolved Coulomb-explosion imaging of nuclear wave-packet dynamics induced in diatomic molecules by intense few-cycle laser pulses", Phys. Rev. A - At. Mol. Opt. Phys. **83**, 1–17 (2011).

[113] I. Bocharova, R. Karimi, E. F. Penka, J. P. Brichta, P. Lassonde, X. Fu, J. C. Kieffer, A. D. Bandrauk, I. Litvinyuk, J. Sanderson, and F. Légaré, "Charge resonance enhanced ionization of CO_2 probed by laser coulomb explosion imaging", Phys. Rev. Lett. **107**, 1–5 (2011).

[114] X. Xie, S. Roither, M. Schöffler, H. Xu, S. Bubin, E. Lötstedt, S. Erattuphuza, A. Iwasaki, D. Kartashov, K. Varga, G. G. Paulus, A. Baltuška, K. Yamanouchi, and M. Kitzler, "Role of proton dynamics in efficient photoionization of hydrocarbon molecules", Phys. Rev. A - At. Mol. Opt. Phys. **89**, 1–9 (2014).

[115] N. Takemoto and A. Becker, "Time-resolved view on charge-resonance-enhanced ionization", Phys. Rev. A - At. Mol. Opt. Phys. **84** (2011).

[116] E. Lötstedt, T. Kato, and K. Yamanouchi, "Enhanced ionization of acetylene in intense laser fields", Phys. Rev. A **85**, 041402 (2012).

[117] E. Lötstedt, T. Kato, and K. Yamanouchi, "Intramolecular electron dynamics in the ionization of acetylene by an intense laser pulse", J. Chem. Phys. **138**, 104304 (2013).

[118] S. Erattupuzha, C. L. Covington, A. Russakoff, E. Lötstedt, S. Larimian, V. Hanus, S. Bubin, M. Koch, S. Gräfe, A. Baltuška, X. Xie, K. Yamanouchi, K. Varga, and M. Kitzler, "Enhanced ionisation of polyatomic molecules in intense laser pulses is due to energy upshift and field coupling of multiple orbitals", J. Phys. B At. Mol. Opt. Phys. **50**, 125601 (2017).

[119] M. R. Thompson, M. K. Thomas, P. F. Taday, J. H. Posthumus, A. J. Langley, L. J. Frasinski, and K. Codling, "One and two-colour studies of the dissociative ionization and Coulomb explosion of H_2 with intense Ti:sapphire laser pulses", J. Phys. B At. Mol. Opt. Phys. **30**, 5755–5772 (1997).

[120] J. Wu, A. Vredenborg, L. P. H. Schmidt, T. Jahnke, A. Czasch, and R. Dörner, "Comparison of dissociative ionization of H_2, N_2, Ar_2, and CO by elliptically polarized two-color pulses", Phys. Rev. A **87**, 023406 (2013).

[121] L. Zhang, X. Xie, S. Roither, Y. Zhou, P. Lu, D. Kartashov, M. Schöffler, D. Shafir, P. B. Corkum, A. Baltuška, A. Staudte, and M. Kitzler, "Subcycle Control of Electron-Electron Correlation in Double Ionization", Phys. Rev. Lett. **112**, 193002 (2014).

[122] M. Shapiro, J. W. Hepburn, and P. Brumer, "Simplified laser control of unimolecular reactions: Simultaneous (ω1, ω3) excitation", Chem. Phys. Lett. **149**, 451–454 (1988).

[123] H. Li, X. Gong, K. Lin, R. de Vivie-Riedle, X. M. Tong, J. Wu, and M. F. Kling, "Subcycle directional control of the dissociative ionization of H_2 in tailored femtosecond laser fields", J. Phys. B At. Mol. Opt. Phys. **50**, 172001 (2017).

[124] Q. Song, X. Gong, Q. Ji, K. Lin, H. Pan, J. Ding, H. Zeng, and J. Wu, "Directional deprotonation ionization of acetylene in asymmetric two-color laser fields", J. Phys. B At. Mol. Opt. Phys. **48**, 094007 (2015).

[125] T. Endo, H. Fujise, Y. Kawachi, A. Ishihara, A. Matsuda, M. Fushitani, H. Kono, and A. Hishikawa, "Selective bond breaking of CO_2 in phase-locked two-color intense laser fields: laser field intensity dependence", Phys. Chem. Chem. Phys **19**, 3550–3556 (2017).

[126] D. W. Schumacher, F. Weihe, H. G. Muller, and P. H. Bucksbaum, "Phase Dependence of Intense Field Ionization: A Study Using Two Colors", Phys. Rev. Lett. **73**, 1344–1347 (1994).

[127] H. G. Muller, P. H. Bucksbaum, D. W. Schumacher, and A. Zavriyev, "Above-threshold ionisation with a two-colour laser field", J. Phys. B At. Mol. Opt. Phys. **23**, 2761–2769 (1990).

[128] B. Sheehy, B. Walker, and L. F. DiMauro, "Phase Control in the Two-Color Photodissociation of HD^+", Phys. Rev. Lett. **74**, 4799–4802 (1995).

[129] X. Xie, S. Roither, D. Kartashov, E. Persson, D. G. Arbó, L. Zhang, S. Gräfe, M. S. Schöffler, J. Burgdörfer, A. Baltuška, M. Kitzler, S. Gräfe, M. S. Schöffler, J. Burgörfer, A. Baltuška, and M. Kitzler, "Attosecond Probe of Valence-Electron Wave Packets by Subcycle Sculpted Laser Fields", Phys. Rev. Lett. **108**, 193004 (2012).

[130] Y. Mi, N. Camus, M. Laux, L. Fechner, R. Moshammer, and T. Pfeifer, "Ionization of atoms and molecules in a strong two-color field", J. Phys. Conf. Ser. **635**, 092093 (2015).

[131] Q. Song, P. Lu, X. Gong, Q. Ji, K. Lin, W. Zhang, J. Ma, H. Zeng, and J. Wu, "Dissociative double ionization of CO in orthogonal two-color laser fields", Phys. Rev. A **95**, 013406 (2017).

[132] S. Eckart, M. Richter, M. Kunitski, A. Hartung, J. Rist, K. Henrichs, N. Schlott, H. Kang, T. Bauer, H. Sann, L. P. H. Schmidt, M. Schöffler, T. Jahnke, and R. Dörner, "Nonsequential Double Ionization by Counterrotating Circularly Polarized Two-Color Laser Fields", Phys. Rev. Lett. **117**, 133202 (2016).

[133] S. De, I. Znakovskaya, D. Ray, F. Anis, N. G. Johnson, I. a. Bocharova, M. Magrakvelidze, B. D. Esry, C. L. Cocke, I. V. Litvinyuk, and M. F. Kling, "Field-Free Orientation of CO Molecules by Femtosecond Two-Color Laser Fields", Phys. Rev. Lett. **103**, 153002 (2009).

[134] K. Oda, M. Hita, S. Minemoto, and H. Sakai, "All-optical molecular orientation", Phys. Rev. Lett. **104**, 213901 (2010).

[135] D. J. Cook and R. M. Hochstrasser, "Intense terahertz pulses by four-wave rectification in air", Opt. Lett. **25**, 1210 (2000).

[136] E. J. Takahashi, P. Lan, O. D. Mücke, Y. Nabekawa, and K. Midorikawa, "Infrared Two-Color Multicycle Laser Field Synthesis for Generating an Intense Attosecond Pulse", Phys. Rev. Lett. **104**, 233901 (2010).

[137] P. Wei, J. Miao, Z. Zeng, C. Li, X. Ge, R. Li, and Z. Xu, "Selective Enhancement of a Single Harmonic Emission in a Driving Laser Field with Subcycle Waveform Control", Phys. Rev. Lett. **110**, 233903 (2013).

[138] S. Haessler, T. Balčiūnas, G. Fan, L. E. Chipperfield, and A. Baltuška, "Enhanced multi-colour gating for the generation of high-power isolated attosecond pulses", Sci. Rep. **5**, 10084 (2015).

[139] S. Watanabe, K. Kondo, Y. Nabekawa, A. Sagisaka, and Y. Kobayashi, "Two-Color Phase Control in Tunneling Ionization and Harmonic Generation by a Strong Laser Field and Its Third Harmonic", Phys. Rev. Lett. **73**, 2692–2896 (1994).

[140] K. Kondo, Y. Kobayashi, A. Sagisaka, Y. Nabekawa, and S. Watanabe, "Tunneling ionization and harmonic generation in two-color fields", J. Opt. Soc. Am. B **13**, 424–429 (1996).

[141] D. Xenakis, N. E. Karapanagioti, O. Faucher, E. Hertz, and D. Charalambidis, "Observation of field phase dependent autoionization", J. Phys. B At. Mol. Opt. Phys. **32**, 341–348 (1999).

[142] C. Chen and D. S. Elliott, "Measurements of Optical Phase Variations Using Interfering Multiphoton Ionization Processes", Phys. Rev. Lett. **65**, 1737–1740 (1990).

[143] M. Shapiro and P. Brumer, "Coherent control of molecular dynamics", Reports Prog. Phys. **66**, 859–942 (2003).

[144] H. Xu, H. Hu, X.-M. Tong, P. Liu, R. Li, R. T. Sang, and I. V. Litvinyuk, "Coherent control of the dissociation probability of H_2 in ω-3ω two-color fields", Phys. Rev. A **93**, 063416 (2016).

[145] C. Jin, G. Wang, H. Wei, A.-T. Le, and C. D. Lin, "Waveforms for optimal sub-keV high-order harmonics with synthesized two- or three-colour laser fields", Nat. Commun. **5**, 4003 (2014).

[146] L. Zhang, G.-L. Wang, and X.-X. Zhou, "Optimized two- and three-colour laser pulses for the intense terahertz wave generation", J. Mod. Opt. **63**, 2159–2165 (2016).

[147] T. T. Luu, M. Garg, S. Y. Kruchinin, A. Moulet, M. T. Hassan, and E. Goulielmakis, "Extreme ultraviolet high-harmonic spectroscopy of solids", Nature **521**, 498–502 (2015).

[148] M. Garg, M. Zhan, T. T. Luu, H. Lakhotia, T. Klostermann, A. Guggenmos, and E. Goulielmakis, "Multi-petahertz electronic metrology", Nature **538**, 359–363 (2016).

[149] M. T. Hassan, T. T. Luu, A. Moulet, O. Raskazovskaya, P. Zhokhov, M. Garg, N. Karpowicz, a. M. Zheltikov, V. Pervak, F. Krausz, and E. Goulielmakis, "Optical attosecond pulses and tracking the nonlinear response of bound electrons", Nature **530**, 66–70 (2016).

[150] H. Fattahi, H. G. Barros, M. Gorjan, S. Prinz, M. Haefner, M. Ueffing, A. Alismail, L. Vámos, A. Schwarz, O. Pronin, J. Brons, X. T. Geng, G. Arisholm, M. Ciappina, V. S. Yakovlev, D.-E. Kim, A. M. Azzeer, N. Karpowicz, D. Sutter, Z. Major, T. Metzger, and F. Krausz, "Third-generation femtosecond technology", Optica **1**, 45 (2014).

[151] S.-W. Huang, G. Cirmi, J. Moses, K.-H. Hong, S. Bhardwaj, J. R. Birge, L.-J. Chen, E. Li, B. J. Eggleton, G. Cerullo, and F. X. Kärtner, "High-energy pulse synthesis with sub-cycle waveform control for strong-field physics", Nat. Photonics **5**, 475–479 (2011).

[152] T. Endo, H. Fujise, A. Matsuda, M. Fushitani, H. Kono, and A. Hishikawa, "Coincidence momentum imaging of asymmetric Coulomb explosion of CO_2 in phase-locked

two-color intense laser fields", J. Electron Spectros. Relat. Phenomena **207**, 50–54 (2016).

[153] V. Wanie, H. Ibrahim, S. Beaulieu, N. Thiré, B. E. Schmidt, Y. Deng, A. S. Alnaser, I. V. Litvinyuk, X.-M. Tong, and F. Légaré, "Coherent control of D_2 /H_2 dissociative ionization by a mid-infrared two-color laser field", J. Phys. B At. Mol. Opt. Phys. **49**, 025601 (2016).

[154] M. G. Pullen, W. C. Wallace, D. E. Laban, A. J. Palmer, G. F. Hanne, A. N. Grum-Grzhimailo, K. Bartschat, I. Ivanov, A. Kheifets, D. Wells, H. M. Quiney, X. M. Tong, I. V. Litvinyuk, R. T. Sang, and D. Kielpinski, "Measurement of laser intensities approaching 10^{15} W/cm^2 with an accuracy of 1%", Phys. Rev. A **87**, 053411 (2013).

[155] P. A. Anderson, "The Work Function of Copper", Phys. Rev. **76**, 388–390 (1949).

[156] C. A. Mancuso, K. M. Dorney, D. D. Hickstein, J. L. Chaloupka, X.-M. Tong, J. L. Ellis, H. C. Kapteyn, and M. M. Murnane, "Observation of ionization enhancement in two-color circularly polarized laser fields", Phys. Rev. A **96**, 023402 (2017).

Danksagung

An dieser Stelle möchte ich allen Personen danken, die mich während meiner Doktorarbeit unterstützt haben. Für die schöne Zeit in den letzten 4.5 Jahren an zwei verschiedenen Instituten und in zahlreichen Kooperationen mit internationalen Forschungsgruppen bin ich sehr dankbar. Hier möchte ich gerne die wichtigsten Personen aufführen, die mir diese Zeit so angenehm und kurzweilig gemacht haben:

- Zuallererst möchte ich Matthias Kling für die Möglichkeit danken, die Doktorarbeit in seiner Gruppe anzufertigen. Insbesondere die außergewöhnlich gute Infrastruktur und die wissenschaftliche Expertise, mit der er meine Arbeit unterstützt hat, aber auch die außerberuflichen Aktivitäten wie das Skifahren oder die Weihnachtsfeier haben es mir ermöglicht, die Zeit als Doktorand so zu genießen.

- Matthias Kübel und Boris Bergues und Wilhelm Frisch danke ich für die angenehme Zusammenarbeit, die vielen guten Ratschläge und die Unterstützung in guten und entspannten, wie auch in anstrengenden und stressigen Zeiten.

- I would like to thank all the members of the Kling group for the nice atmosphere and the many fun excursions: Matthias and Matthias, Philipp and Philipp, Johannes and Johannes, Max and Max and Max, Wilhelm, Nora, Boris, Sergey, Hiro, Shubadeep, Benni, Harald, Marcel, Sambit, Tom, and Hui. Through you I experienced all the positive effects of a teamwork.

- Desweiteren danke ich Regina de Vivie-Riedle, Robert Siemering, und Thomas Schnappinger für die vielen aufschlussreichen Diskussionen und Berechnungen, welche es ermöglicht haben, die experimentellen Daten auch theoretisch zu erklären.

- I would like to thank the IMPRS-APS team for the great atmosphere, which I could enjoy at many nice events and locations with so many nice and open-minded people. Special thanks goes to Matthias, Nick, Hannieh and of course the one and only Mrs. Wild.

- I'm grateful to the LMU lunch-team: Tobi, Maxi, Stephan, Dominik, Kathrin, Elena, Matt, Nora, Kellie, and all the others joining in from time to time. It was always a really great time with so many mind-opening discussions.

- Furthermore, I would like to thank all people I worked with in the fruitful cooperations: Robert Moshammer and his team with special thanks to Kirsten Schnorr, Sven Augustin, and Georg Schmid; Don Eon Kim with his team and especially Tsendsuren Khurelbaatar and Jiuding Kim; Hans-Jakob Wörner and his team with special thanks to Thomas Gaumnitz, Inga Jordan, and Martin Huppert; Artem Rudenko, Alina Khodko, Atia Tul-Noor, Han Xu, and Igor Litvinyuk.

- Ganz herzlich möchte ich mich noch bei meiner Familie bedanken, welche immer hinter mir steht und mich in allen Lebenslagen unterstützt.

- Mein größter Dank geht an meine Frau Karin, welche mich in allen Lebenslagen unterstützt und motiviert. In schwierigen Zeiten gibst du mir den nötigen Rückhalt und hilfst mir mit zusätzlicher Motivation und die guten Zeiten verschönerst du mir mit deiner unvergleichlichen Lebensfreude. Danke!